SOVIET ATOMIC ENERGY

АТОМНАЯ ЭНЕРГИЯ

(ATOMNAYA ÉNERGIYA)

TRANSLATED FROM RUSSIAN

SOVIET ATOMIC ENERGY

Soviet Atomic Energy is a translation of *Atomnaya Énergiya*, a publication of the Academy of Sciences of the USSR.

An agreement with the Copyright Agency of the USSR (VAAP) makes available both advance copies of the Russian journal and original glossy photographs and artwork. This serves to decrease the necessary time lag between publication of the original and publication of the translation and helps to improve the quality of the latter. The translation began with the first issue of the Russian journal.

Consultants Bureau journals appear about six months after the publication of the original Russian issue. For bibliographic accuracy, the English issue published by Consultants Bureau carries the same number and date as the original Russian from which it was translated. For example, a Russian issue published in December will appear in a Consultants Bureau English translation about the following June, but the translation issue will carry the December date. When ordering any volume or particular issue of a Consultants Bureau journal, please specify the date and, where applicable, the volume and issue numbers of the original Russian. The material you will receive will be a translation of that Russian volume or issue.

CONSULTANTS BUREAU, NEW YORK AND LONDON

233 Spring Street
New York, New York 10013

SOVIET ATOMIC ENERGY

A translation of *Atomnaya Énergiya*

August, 1984

Volume 56, Number 2

February, 1984

CONTENTS

CONTENTS

(continued)

Engl./Russ.

The Russian press date (podpisano k pechati) of this issue was 1/26/1984.
Publication therefore did not occur prior to this date, but must be assumed
to have taken place reasonably soon thereafter.

CONTROL OF THE ENERGY DISTRIBUTION AND SAFETY OF A VVÉR-1000

REACTOR WHEN OPERATING IN THE VARIABLE MODE

E. V. Filipchuk, V. A. Voznesenskii,
V. G. Dunaev, I. A. Luk'yanets, V. I. Mitin,
P. T. Potapenko, and E. S. Timokhin

UDC 621.039.512:621.039.515

Increases in the dimensions and power of reactors demand a qualitatively new approach to the nuclear reactor as a subject for control with distributed parameters [1]. The present article investigates one approach to the control of energy distribution as applied to the type VVÉR-1000 reactor [2], based on present-day control theory. Model results indicate that the proposed control algorithm is effective for base-load operations and for conditions of variable load. The need to vary the power of a nuclear power station can arise from faults in various systems or plant (fault conditions) or through operation of the station under variable load conditions (variable mode). The power of a reactor can be varied by altering the setting of the control rods and by operating a boron regulating system.

The control strategy for varying the power under steady-state conditions is based on the maintenance of a given form of energy distribution within permissible limits, enabling the minimum-possible safety factor in thermal loading to be employed. The algorithm for controlling the energy distribution is calculated by computer. This has to take account of the occurrence of xenon oscillations in the neutron field, variations in the reactivity factor in the process of burnup, and the proximity of the principal engineering parameters of the reactor to their maxima.

It is desirable for the operator to apply the best possible sequence of control parameters when controlling the energy distribution, by acting upon the control rods and boron regulating system.

Control System. The computerized control system of the VVÉR-1000 is a data measurement and processing complex with a system for monitoring conditions within the reactor, an operator, means for affecting the reactivity (the control rods and boron regulating system) and the reactor itself. This latter represents a control object with distributed parameters.

The system for monitoring conditions inside the reactor as a primary source of information has water-temperature detectors at the outlet of the coolant system. Each probe has several rhodium β-emission detectors equispaced in height. A proportion of such probes are uniformly distributed throughout the core, the remainder being sited in the coolant system, conforming to various degrees of symmetry. The sensitive part of these β detectors is made of rhodium. The reactor monitoring system includes apparatus for selecting, preprocessing and transmitting the detector signals to the computer centre, together with the specialized mathematical software needed for processing the detector signals and presenting the necessary data to the operator's VDU.

The purpose of system monitoring is to provide the operator with full and accurate data on the neutron and thermohydraulic processes taking place in the core. Specifically, this concerns the energy distribution throughout the volume of the core, the margin in relation to heat-exchange crisis and other parameters registering the position of the regulator.

The density of neutron flux at the points at which the β-emission detectors are cited is determined by multiplying the detector currents by the appropriate coefficients. The matrix of coefficients is stored in the memories at the computer centre. These coefficients are then amended as necessary during burnup. The energy distribution is determined as a linear combination of a known set of reference functions. The amplitudes (coefficients of linear combination) are calculated from the measured densities of neutron flux. By using six reference functions, we are able to reduce the mean-square methodical error in calculating the energy distribution to <1%.

When a computer and a system of reactor-core monitoring are used together, the operator is able to monitor the reactor under normal conditions of operation and prevent the onset of disturbances connected with nuclear-safety situations.

Investigations carried out on the VVER-1000 have shown that the means for affecting the reactivity (the control rods and boron regulation system) are adequate for effective control of energy distribution [3]. When running on load, practically the whole of the control rods, with the exception of those concerned with automatic regulation of power, is entirely devoted to preventing distorsions in energy distribution. The boron regulating system of the reactor compensates not only for the burnup of the fuel, but also for the poisoning of the fuel elements.

A mathematical model [4] has been used in the development and study of various approaches and algorithms concerned with the problem of control. This contains two-group diffusion equations for calculating the distribution of neutron-flux density and equations for mass and energy balance in the primary coolant circuit. The model takes account of the main feedback loops in the core of the reactor and the burnup of fuel, enabling the axial and radial-azimuthal distributions of energy to be found, together with the concentrations of xenon and iodine in the core. Various approximations and recurrence formulas are used to reduce the time involved in the calculation. The necessary coefficients are predetermined and recalculated as need be during the burnup, on the basis of core measurements.

Instabilities in the axial distribution of power can arise in the core of a VVER-1000 under certain conditions, namely xenon oscillations with a period of 21-24 h. Oscillations of the axial distribution of power can be accompanied by damping of the radial-azimuthal oscillations. The greatest distortion in the energy distribution arises under transient conditions of operation with moderate reductions in load (up to 40-50%) and is followed (after some hours) by the recovery of rated values.

The effectiveness of using a computer in raising the operational safety of reactor plant rests upon the introduction into the program of a model of the reactor. The presence of such a model in the package of programs enables a series of important variable states of the reactor that have not been measured to be calculated, and varations of state to be forecast for all disturbances of the rated conditions of the unit during the control of the reactor.

Control Algorithm. The aim of control is to maintain the energy distribution in the core under steady-state and non-steady-state conditions with minimum-possible error. The distribution should be maintained close to the specified value, taking engineering limitations into consideration.

The main contributions to deviations in the neutron field are the fundamental and first harmonic. The fundamental is determined by the specific optimum distribution and is monitored by the automatic power regulation. The first harmonic introduces power unbalances between the upper and lower halves of the core. By taking these into account, we are able to formulate a control target which can achieve an effective suppression of the fundamental and first harmonic. The advisability of such an approach is based on the use of two means of acting on the reactor: the regulator and the boron regulating system. The amplitudes of the harmonics being regulated are measured with the aid of the computer center. The mathematical formula for the control problem consists as follows. A vector of state S is formed, consisting of the deviation in the neutron flux density distribution and the deviations in the concentrations of xenon and iodine from standard at specific moments in time. Control of the final state consists in finding the sequence of control actions that will convert the dynamic state of the system from the initial state S(0) into zero state S(N) in a definite (minimum) number N of operations, while complying with the following engineering limitations.

The specified linear power of the fuel elements.

The maximum rate of change of the axial first harmonic, set by requirements related to the engineering reliability of the core.

The limiting magnitude and speed of the control action, connected with the limited reactivity introduced by the control rods and with the final speed of introduction of boric acid and its dilution in the coolant.

The need to maintain a given total reactor power.
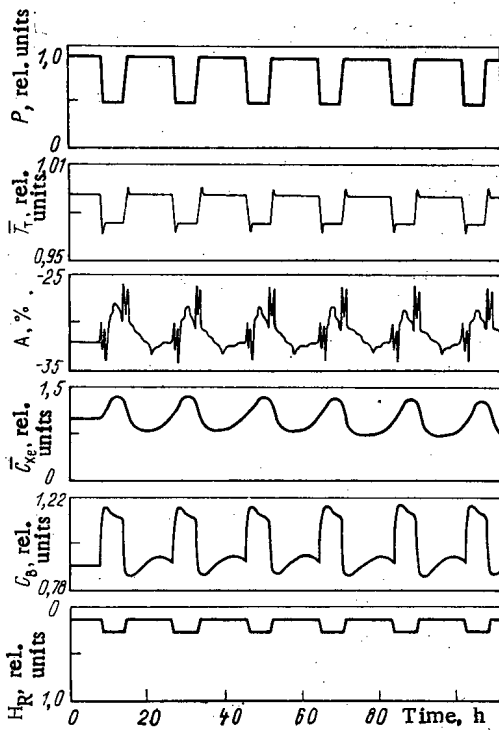
Fig. 1   Fig. 2

Fig. 1. Control of power and axial distributions of energy during power variations at a rate of 1% per minute.
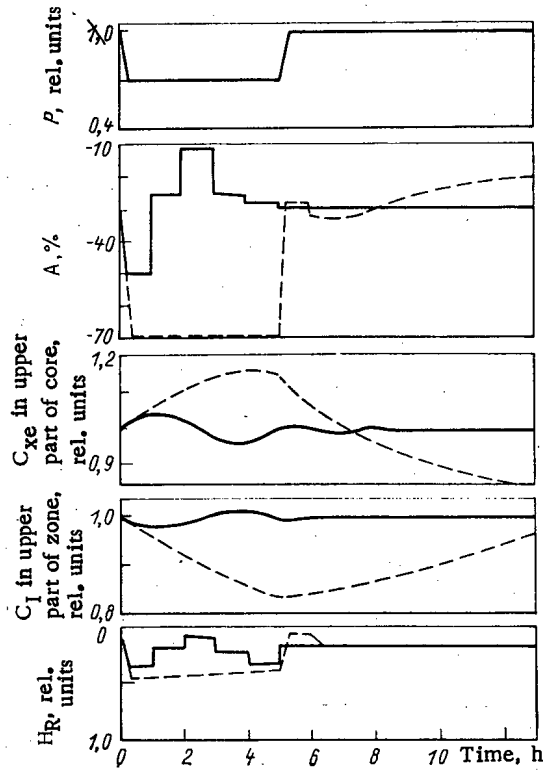
Fig. 2. Transients in control of axial distribution of energy (---) and the results achieved by control (——).

When selecting a criterion of quality in the form of the quadratic target function $J = S^T(N)S(N)$, the initial problem reduces to one of quadratic programming, the numerical solution to which has been well developed [5].

We shall give the most characteristic examples of the solutions to these problems.

1. Varying the Power at a Rate of 1% per Minute with Large Margins in Reactivity Compensated by the Boron Regulation System. This condition is characteristic of the start of burnup.

In this case, we can use the boron regulating system to maintain a given rate of change of power. Under these circumstances, the automatic power regulator corrects the vertical energy distribution. Stabilization of the first axial harmonic practically excludes any possibility of xenon oscillations arising.

Figure 1 gives the results obtained by modeling a control algorithm for power P and axial distribution of energy with cyclic variations in load. During regulation, the power developed by the reactor is brought down from 100 to 50% at a rate of 1% per minute by means of the boron regulating system. The automatic power regulator is used to control the axial energy distribution. The deviation in first axial harmonic amplitude A is maintained within the limits ±5% of rated.

2. The Variable-Load Mode at a Speed Exceeding the Dynamic Capability of the Boron Regulating System (up to 5% per minute). In this case, it is necessary to use both the control rods and boron regulating system. Reference [6] proposes ensuring minimum distortion of the vertical distribution of energy by combining the control rods into lighter (in reactivity) groups, fully inserted (or extracted, as the case may be) during changes in power. However, such a strategy would lead to considerable distortions in the radial-azimuthal energy distribution in the case of the VVER-1000, with its relatively "heavy" control rods.

67
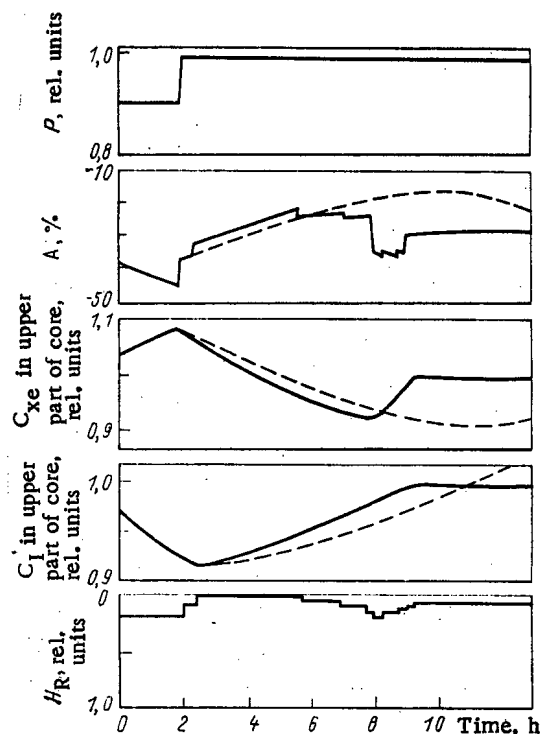
Fig. 3. Free (---) and controlled (——) xenon os-
cillations in energy distribution.
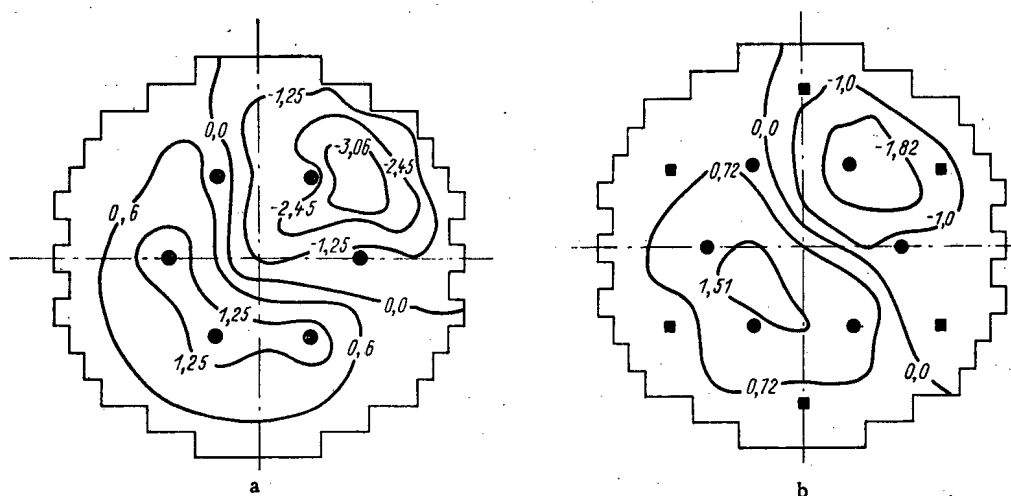
Fig. 4. Excited radial energy distribution prior to (a) and after (b)
control: ●) automatic power regulator; 0.0,—0.1, 1.25, etc. are the dev-
iations of energy distribution from rated in %; ■) control rods used
for controlling radial energy distribution.

The proposed algorithm permits a distortion of the vertical distribution at reduced
power, due to a considerable displacement of the automatic power regulator groups and, if
necessary, additional groups of control rods. The control strategy for reducing power is
aimed at excluding xenon oscillations after the departure from rated power.

The results of modeling the daily load cycle at a rate of power change of 5% per min-
ute are shown in Fig. 2. During the simulation, the reactive power was reduced to 70% of rated
over a period of 6 min and after a hold of 5 h the load was returned to rated power level
at the same speed. The boron regulating system and the group of control rods linked to the
automatic power regulator were used to control the reactor. The results show that the re-
quired state was achieved immediately after the return to full power, due to the predeter-
mined actions of the control system.

68

3. Unplanned Rapid Losses of Power, due Either to Changes in Power-System Demand or as a Result of the Operation of Fault Protection. In this case, the random nature of the disturbances necessitates taking purposeful action on energy distribution from the instant rated power is lost. It is natural that xenon oscillations can arise in such a situation, and these have to be effectively suppressed.

Figure 3 illustrates the results obtained by simulating the suppression of axial xenon oscillations arising from a rapid reduction in power by 10% of rated and its increase again to rated after a hold of 4 h. Immediately after the rise in power, a program is initiated for calculating the best strategy, as far as speed is concerned, for suppressing the xenon oscillations. Figure 3 represents the control law obtained and also the transients for the main variable states of the reactor and the processes within the reactor in the absence of control.

The stabilization of vertical energy distribution is important, but it is not the only problem facing the operator in controlling the distribution of energy in a VVER-1000. Although the regulations have to exclude radial-azimuthal distortions in energy distribution, these are always incipient, due to various irregular situations, such as the loss of rated conditions in one or more circulating loops.

The high stability of the radial-azimuthal distribution of water-cooled reactors, the low levels of disturbance of this distribution during operation, and the rapidly-attenuating nature of the radial-azimuthal xenon oscillation enables the control of this distribution to be formulated as a steady-state problem of finding the closest approximation of the energy distribution to a specified profile, taking the necessary limitations into account. The engineering limitations must take into consideration the standard limitations on the range of control actions, the maintenance of a preset total reactor power, and the continuous limitation of the neutron flux densities in all the fuel elements.

Besides these limitations, we have to ensure that the power levels in the halves of the reactor core are the same, to prevent exciting a first azimuthal harmonic, which is more unstable than the radial-azimuthal xenon oscillations. Satisfaction of this condition ensures identical temperatures when operating the various circulation loops of the reactor.

The control rods and boron regulating system can also be used for controlling the radial-azimuthal energy distribution in a VVER-1000. However, the displacement of the control rods that takes place during the control of the radial field distorts the vertical distribution. To avoid this distortion when controlling the radial distribution, we also have to take account of the need to maintain the amplitude of the first axial harmonic within preset limits. This reduces to the canonical problem of quadratic programming, which can be solved by the same computer procedures as were used to solve the control of vertical energy distribution.

The results of simulating the control algorithm for radial energy distribution in a VVER-1000 is indicated in Fig. 4. A change of 10% of rated in the flow of coolant through one of the circulation loops of the primary coolant circuit is taken as the initial disturbance. The variation in radiant energy distribution due to this disturbance is plotted in Fig. 4a. The lines on the diagram connect the fuel rods with the same power deviations from standard. The circles signify the positions of the control rods belonging to the automatic power regulator group. The radial power field obtained by compensating for the disturbance in the coolant flow is given in Fig. 4b. The boron regulating system and the control rods of a specially chosen group act as control devices.

Conclusions. The main operations in the proposed algorithm for controlling the distribution of energy under variable-load conditions are carried out at a reduced power level. When the power falls, all the control rods are found in the rated position. We show that the main problems in controlling the energy distribution can be solved within the framework of a single computer procedure based on the quadratic programming method. When the proposed algorithm is set up in the computer, together with a realization of the optimum control actions, found from a digital model, we can expect to achieve an increase in efficiency in the work of the operating staff, and as a result, an increased level of safety in the operation of nuclear power stations.

LITERATURE CITED

1. E. V. Filipchuk, P. T. Potapenko, and V. V. Postnikov, Controlling the Neutron Field of a Nuclear Reactor [in Russian], Énergoizdat, Moscow (1981).

2. Yu. V. Vikhorev et al., At. Energ., 50, No. 2, 87 (1981).
3. V. A. Sidorenko, Problems of Safe Operation of Type VVÉR Reactors [in Russian], Atomiz-dat, Moscow (1977).
4. E. S. Timokhin, in: Control of Nuclear Power Plant [in Russian], No. 5, Énergoizdat, Moscow (1981), p. 52.
5. G. Dantzig and R. Cottle, in: Nonlinear Programming, North-Holland, Amsterdam (1968), p. 57.
6. P. T. Potapenko, V. G. Dunaev, and E. S. Timokhin, At. Tekh. Rubezhom, No. 5, 3 (1979).

MULTICHANNEL CORRELATION SYSTEM FOR MEASUREMENT OF THE

COOLANT FLOW RATE FOR HIGH-POWERED WATER-COOLED

CHANNEL REACTORS (RBMK)

V. M. Selivanov, B. V. Lysikov,
N. P. Karlov, B. A. Kuznetsov,
A. D. Martynov, V. V. Prostyakov,*
D. Pallagi, Sh. Khorani, T. Khargitai,
and Sh. Tezhert†

Investigations of the physical nature of the thermal noise of a coolant and study of the application of the correlation method to measurement of the flow velocity of a liquid [1] have shown the possibility of creating a system for measurement of the flow rate in the fuel channels (FC) of an RBMK reactor in which correlation of the random signals of thermo-electric transducers (TET) is used. The basic requirements for such a system have been formulated in bench and reactor tests of models of a thermometric correlation flow meter [2, 3].

Taking account of the structural characteristics of RBMK, the channel-by-channel accumulation of statistical data with subsequent analysis of it by a single microprocessor seems the most advisable. This approach reduces the cost of the equipment and makes it possible to divide the analog I and digital II parts of the system (Fig. 1) into two separate units, which facilitates maintenance and makes the system more flexible.

The TET signals, which are amplified and filtered by the amplifier 1 with a transmission band of 0.5-8 Hz, enter the input of the system. It has been established in measuring the intensity of the thermal noise of the coolant in different FC of a reactor that the minimum mean square value of the input signal is ∿0.1 μV. The low level of the signal places high requirements both on the noise protection circuit and on the degree of intrinsic noise of the amplifiers, which has made it necessary to create a specialized amplifier with intrinsic noise ∿0.05 μV.

Structurally, the amplifier 1 consists of a preamplifier, the amplifier itself, and an active filter. The preamplifier is built around Type KT 3102, KT 3107, and KT 325 low-noise high-frequency transistors. Four Type K284UD1A and K553UD1A microcircuits are used in the amplifier itself and the active filter. The gain coefficient can be varied within the limits of $(0.5-16) \times 10^6$ and is set so that the standard deviation of the output signal of the amplifier 1, which is monitored by the comparison circuit 2, was no less than ∿1 V.

A comparator 3, which along with the amplifier and the comparison circuit comprises the information channel, is used to convert the analog signal to a digital one. The analog unit of the multichannel system consists of 16 measuring channels. The output signals of

_____
*USSR.
†Hungarian People's Republic.
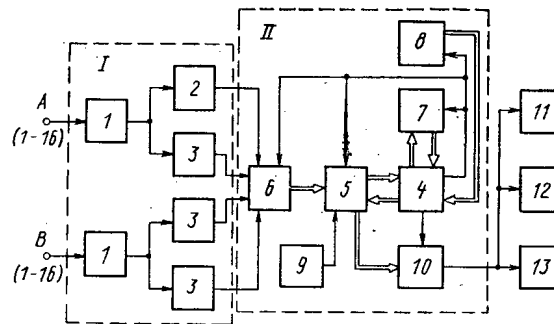
Fig. 1. Structural diagram of the correlation system.

the analog unit enter the commutator 6 and then the programmable input—output circuit 5. The digital unit and the computation unit are controlled by a Z-80 microprocessor — position 4. The results obtained and the constants are stored in an operatoral memory 7 with a capacity of seven kilobytes. The calculated values of the velocity and flow rate through the interface system 10 are presented on the display 11 and the teletype 12.

Information which permits performing diagnostics of the system operation can be presented on the plotter 13 and the display or teletype. The necessary information is provided upon request of the operator by means of a keyboard 9, with whose help one can also start or stop the measurement and calculation process and introduce or change the constants. The programming for the system is written in the constant memory 8 with a capacity of eight kilobytes. It contains the following programs: the monitor program, a program for the measurements and data collection, a program for calculation of the velocity and flow rate of the coolant, and a program for presentation of the results [4].

One can write the standard algorithm for calculation of the cross-correlation function (CCF) by the digital method in the form

$$R_{AB}(i\Delta\tau) = \frac{1}{N} \sum_{n=0}^{N-1} a(n\Delta\tau - i\Delta\tau)\, b(n\Delta\tau) \tag{1}$$

for $N \gg i$,

where $\Delta\tau$ is the quantization step, i is the step number, and N is the sampling duration.

The application of this algorithm in multichannel information processing is complicated even in the case of one-bit quantization due to insufficient response speed of the microprocessors. Therefore a special method is used in the correlation measurement system in which the signal interrogation period b(t) is the same as in the standard algorithm but the signal a(t) is interrogated more rarely; the ratio of the periods S is a whole number [5]. For one-bit quantization and the special interrogation method Eq. (1) will take the form

$$R_{AB}(i\Delta\tau) = \sum_{n=0}^{S(N-1)} \left\{ \frac{1}{2}\, \mathrm{sgn}\,[a(n\Delta\tau - i\Delta\tau)]\, \mathrm{sgn}\,[b(n\Delta\tau)] + \frac{1}{2} \right\} \text{ for } N \gg I_+, \tag{2}$$

where $-I_- \leqslant i \leqslant I_+$ ($I_-\Delta\tau$ is the maximum negative time shift, and $I_+\Delta\tau$ is the maximum positive time shift), N is the duration of sampling of the signal a(t), n = kS, and k = 0, 1, 2, ..., N — 1. In accordance with the Kotel'nikov theorem, the inequality

$$S\,\Delta\tau < 1/2f_{max},$$

where f_{max} is the maximum frequency of the signal, should be observed when selecting S. The maximum value of the function calculated according to Eq. (2) is equal to N (correlation coefficient of unity), and the minimum value is equal to zero (correlation coefficient of —1).

The delay time is determined from the position of the maximum of the CCF. In order to reduce the statistical error in the determination of the transport time, it is more advisable to use not the coordinate of the maximum but the abscissa of the center of gravity of the

71
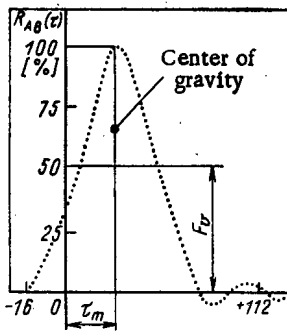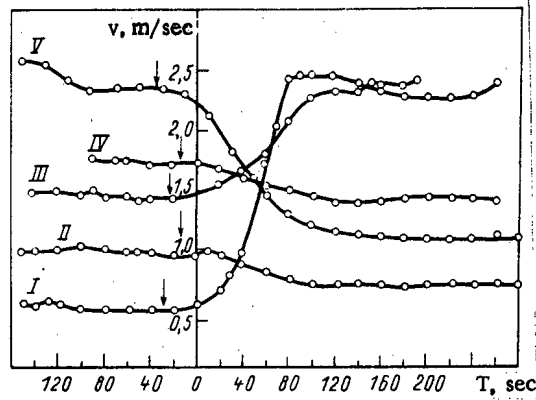
Fig. 2

Fig. 3

Fig. 2. Appearance of the correlation function.

Fig. 3. Reaction of the system to a change in the flow rate (I–V — channels of the correlation system).

figure bounded by the CCF and some arbitrary straight line parallel to the abscissa axis, which is called the baseline level F_v (Fig. 2).

With the structural characteristics of the thermometric correlation flow meter for RBMK taken into account, the values of the velocity v and the flow rate Q of coolant in the FC are calculated from the following formulas:

$$v = \frac{K_{1v}}{\tau_m \pm K_2}; \quad Q = \frac{K_{1Q}}{\tau_m \pm K_2},$$

where K_{1v} is the distance between the TET, τ_m is the transport time, K_2 is a coefficient which corrects for the difference between the time constants of the TET and the measuring channels, and K_{1Q} is the calibration coefficient of the flow meter.

The operation of the correlation measurement system begins with an inquiry of the constants necessary for functioning of the program: the quantization step $\Delta\tau$, the correlation level ρ, the baseline level F_v, the periodicity of output to the teletype T, the coefficients K_{1v}, K_{1Q}, and K_2, and the placings of v1–v16 or Q1–Q16.

The choice of the quantization step depends on the flow velocity of the coolant and can be specified in the 5-20 msec range. Since $I_+ = 112$, the minimum velocity which it is possible to measure when $\Delta\tau = 5.0$ msec and $K_{1v} = 0.2$ m is ∿0.4 m/sec. When the quantization step is increased, the resolving power of the system decreases, and consequently the statistical error of velocity measurement increases. In addition averaging of no more than eight values of successively calculated positions of maxima of the CCF (B ≤ 8) is carried out to smooth the measurement results. The averaged velocity (flow rate) of the coolant:

$$\bar{v} = \frac{1}{A} \sum_{i=1}^{A} v_i,$$

where v_i is the i-th value of the velocity (flow rate) and A is the number of calculated positions of maxima of the CCF selected from B for calculation of the average velocity according to the algorithm (A = B − 2 if B > 2 and A = B if B = 2). The maximum and minimum values are discarded in the calculation of the velocity (flow rate) in order to reduce the effect of overshoots on the final result.

The correlation system constantly controls the level of correlation between the signals being analyzed and the velocity (flow rate) of the coolant. If their values are less than the specified constants (ρ, v1–v16), the system signals to the operator.

After introduction of the constants the program monitors the input signals and the functionining of the equipment. Conclusion of the test program and a transfer to the measurement and data collection subprogram occurs in response to an interrupt from the cycle

72
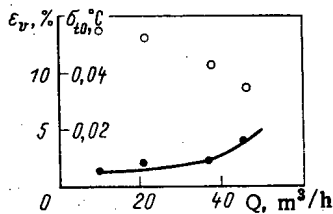
Fig. 4. Dependence of the
measurement error (●) and
the intensity of the tem-
perature fluctuations (o)
on the flow velocity of
the coolant.

generator. The duration of the sampling from which the CCF is calculated is determined by the
size of the operational memory $n = 8 \times 256$. The velocity or flow rate of the coolant is de-
termined from the values obtained for the function with the help of the described algorithm.
Then the program transfers to the test subprogram and the cycle is repeated. It should be
noted that erasing of only one-half of the data occurs to increase the rate at which infor-
mation is obtained upon transfer to the new cycle. Thus the time required for obtaining the
CCF is $T = (8 \times 256)/2 \, \Delta\tau$, where $\Delta\tau$ is the quantization step.

In order to estimate the parameters of the correlation system for measurement of coolant
flow rate, which are important design characteristics, bench tests were run. TET with an
uninsulated working junction 1.5 mm in diameter were used as the primary transducers; the
distance between TET was 200 mm. The measurements were made at a coolant temperature of
200-270 C, a pressure of 8-9 MPa, and a flow rate of 10-70 m³/h, which corresponds to a
velocity of 0.4-2.8 m/sec ($K_{1V} = 0.2$ m, and $K_{1Q} = 5$ m³·sec/h). The constants necessary
for operation of the system were not changed: $\Delta\tau = 5$ msec, $A = 6$, $B = 8$, and $F_V = 95\%$.

Upon a change in the coolant flow rate the readings of the system varied in accordance
with the established values of the flow rate (Fig. 3), which were monitored by a regular
differential manometric flow meter. Since it is impossible to change instantaneously the
flow rate in a channel, the end of flow rate regulation (the start is shown by an arrow)
is taken as the origin of coordinates. The lag of the system for the minimum quantization
step and maximum sample obtained from the experimental data is ∿70 sec. With the minimum
sample ($B = 2$) the time to ascertain the readings is reduced by a factor of four. In addi-
tion the system permits monitoring the flow rate in one selected channel with an information
renewal interval of 10 sec.

The procedure for estimating the system error consisted of multiple recording of the
instrument readings with a constant coolant velocity. The test conditions were such that
the degree of fluctuation of the temperature in the measuring section varied with the change
in the flow rate (Fig. 4). The correlation coefficient between the TET signals remained con-
stant (∿0.6), and the frequency spectrum of the signal was 0.5-3 Hz.

The fluctuations measured by this procedure are the sum of the oscillations of the flow
rate in the channel and the statistical scatter of the system. Due to the dependence
of these components, the measurement error of the system $\varepsilon_S = \sqrt{\varepsilon_\Sigma^2 - \varepsilon_f^2}$, where ε_Σ is the mea-
sured deviation and ε_f is the mean square oscillation of the flow rate in the channel. One
can take $\varepsilon_f \approx 0$ in order that there not be a significant effect on the final result; then the
measured mean square value can be interpreted as the measurement error of the system (see
Fig. 4). The increase in the error for $Q > 50$ m³/h is explained by a number of factors as-
sociated with the construction of the primary transducer.

Thus, the described system permits measuring the flow rate with an error of approximately
<5% in the 10-45 m³/h range at a level of fluctuation of the coolant temperature in the mea-
surement section of ∿0.003°C.

LITERATURE CITED

1. V. M. Selivanov et al., "Utilization of thermocouple random signal correlation method
for coolant flow rate measuring in nuclear power plants," Measurement for Progress in
Science and Technology, IMEKO-VIII, May 21-27, 1979, Preprint Section IV, S. 26, Moscow
(1979), p. 5.

73

2. V. M. Selivanov et al., "The development and investigation of a thermometric correlation system for measurement of the coolant flow rate for a reactor of the RBMK type," Preprint KFKI-1980-70, Budapest (1980).
3. D. Pallagi et al., "The development and investigation of a 16-channel thermometric correlation system for measurement of flow rate," Preprint KFKI-1982-49, Budapest (1982).
4. D. Pallagi et al., "New transit time flowmeter system for coolant flow measurement," in: Proc. Int. Symp. on Nuclear Power Plant Control and Instrumentation, Preprint IAEA-SM-265, Munich (1982).
5. R. Fell and T. Hargital, "Fluid flow measurement using a microprocessor-based correlator," in: Proc. of Mini- and Microcomputers and Their Applications, Budapest (1980), p. 250.

STABILITY OF NATURAL CIRCULATION IN A LOOP WITH
BOILING OF THE COOLANT

V. I. Budnikov and E. F. Sabaev   UDC 621.039.56

Loops with natural circulation of a boiling coolant are widely used in power engineering. Strong underheating of the coolant at the entrance and a low mass flow steam content are characteristic of loops with low pressure. It has been shown in [1] for such conditions that instability of the circulation can arise in the loop for specified parameters of a steady regime. In loops with moderate pressure in which heat removal is accomplished with the help of a Field steam-generating tube the input underheating of the coolant is usually small and the mass flow steam content is high. It has been established in experimental investigations of the evaporator of a nuclear power plant steam generator with a BN-350 [2] that the steady regime of a Field steam-generating tube is stable. At the same time it has been discovered in the experiments that for sufficiently large heat fluxes to the coolant there exists a region of unstable operation of the evaporator.

The stability of natural circulation in a loop is investigated theoretically in this paper within the framework of a unique mathematical model for two cases which are of independent interest: 1) underheating of the coolant at the entrance is so small that boiling of the coolant starts at the entrance to the section being heated; and 2) underheating of the coolant at the entrance is so great that boiling of the coolant occurs only at the exit from the heating zone.

Mathematical Model. Let us consider a circulation loop consisting of a drop tube and a lift section. The latter includes a zone with heat supply, an unheated traction section, and a heat exchanger. A Field tube [2], of which a simplified example is illustrated in Fig. 1, can serve as an example of such a loop. The underheating of water to saturation temperature in the drop tube is usually close to zero in a Field tube. In this connection one can assume in the construction of a mathematical model of a circulation loop that saturated water is located in the drop tube and the enthalpy of the coolant at the entrance to the lift section is equal to the saturation enthalpy. Bearing in mind that the pressure in a Field tube varies slowly, we shall assume the pressure in the circulation loop to be constant. It follows from this that one can assume the enthalpy of the water at the entrance to the lift section to be constant. Next we note that the heat flux from the coolant in the lift section to the water in the drop tube is significantly less than the heat supply from the external source to the steam-water mixture in the lift section.

It is sufficient for investigation of the circulation stability to know the variation in time of the coolant velocity at some point of the loop, for example, at the entrance to the lift section. We shall take into account in the determination of this velocity that the total pressure drop in a closed loop is equal to zero. In other words, we shall take account of the fact that the pressure head of natural circulation, defined as the differ-
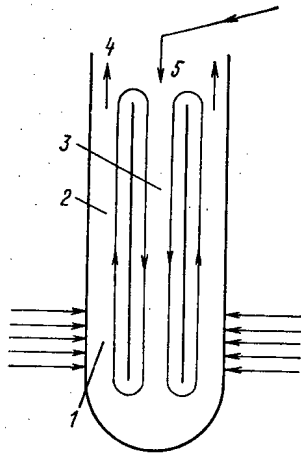
Fig. 1. Simplified scheme of the circulation in a Field tube: 1) heated zone; 2) underheated traction section 3) drop tube; 4) steam exit; and 5) input of supply water.

ence in weight of the columns of water in the drop tube and the steam-water mixture in the lift section, is equal to the total pressure losses in the loop. In the general case the latter are comprised of the pressure losses to acceleration (ΔP_{acc}) and expansion (ΔP_{exp}) of the coolant and also the pressure losses by various kinds of hydraulic drag. However, one can neglect the values ΔP_{acc} and ΔP_{exp} for the low velocity characteristic of natural circulation of the coolant. In this connection the pressure losses in the drop tube can be treated as pressure losses on an equivalent disk located at the entrance to the lift section. Thus the investigation of the stability of natural circulation in a closed loop of the Field tube-type reduces to an analysis of the time-dependent equations which describe the lift section. These equations can be written in the following form on the assumption of quasihomogeneity of the two-phase flow:

$$\frac{\partial i}{\partial t} + u\frac{\partial i}{\partial z} = qv; \tag{1}$$

$$\frac{\partial u}{\partial z} = q\frac{\partial v}{\partial i}; \tag{2}$$

$$H_{n.c.} = \Delta P_{tot}; \tag{3}$$

$$v = \begin{cases} v' & i < i'; \\ v' + \frac{v'' - v'}{r}(i - i') & i' \leqslant i \leqslant i''. \end{cases} \tag{4}$$

Here i, u, and v are the enthalpy, velocity, and specific volume of the coolant, q is the heat flux to the coolant, v' and v" are the specific volume of water and steam on the saturation line, r is the latent heat of vaporization, i' and i" are the enthalpy of water and steam on the saturation line, $H_{n.c.}$ is the pressure head of the natural circulation, ΔP_{tot} is the total pressure losses in the circulation loop, z is the longitudinal coordinate, and t is the time.

We shall investigate the stability on the assumption of smallness of the deviations from a steady regime. With this aim we shall find a solution of the linearized Eqs. (1)–(4), respectively, for a zone with coolant and the traction section, using the Laplace transformation. Then we obtain from these solutions transfer functions on the basis of which we shall derive the characteristic equation. We shall assess the stability of the steady regime from the arrangement of the roots of the characteristic equation.

<u>Derivation of the Characteristic Equation and Analysis of the Stability. First Case.</u> Proceeding as indicated above, we obtain the transfer function $W_1(p)$ relating the variation of the enthalpy of the coolant at the exit from the evaporator zone to the variation of the coolant velocity at its entrance:

$$W_1(p) = \frac{\Delta i (h_{ev})}{\Delta u_{ent}} = -\frac{(v/u)^*}{(\partial v/\partial i)}\left[\frac{1 - \exp(-\lambda \ln m)}{\lambda}\right], \tag{5}$$

where

$$\lambda = \left(p - q\,\frac{\partial v}{\partial i}\right)\Big/ q\,\frac{\partial v}{\partial i};\quad m \cdot v^*\,(h_{ev})/v';$$

u_{ent} is the coolant velocity at the entrance to the evaporator zone, h_{ev} is the height of the evaporator zone, p is the parameter of the Laplace transformation, Δ is the deviation of a variable from its steady value, and "*" is the symbol for a variable in the steady regime.

For simplicity's sake we shall assume that the pressure head of natural circulation developed in the vaporator zone is negligibly small in comparison with the pressure head of the traction section. Then substituting the solution of Eq. (1) for the traction section into the equation for determination of the pressure head of natural circulation, we obtain the transfer function

$$W_2(p) = \frac{\Delta H_{n.c.}}{\Delta i\,(h_{ev})} = \frac{H_{n.c.}^*(M-1)}{m\,(m-1)\,r}\left[\frac{1-\exp(-p\tau_{t.s.})}{p\tau_{t.s.}}\right], \tag{6}$$

where $M = v''/v'$ and $\tau_{t.s.}$ is the time for the coolant to pass through the traction section in the steady regime. Bearing in mind the relationship $(m-1) = x(M-1)$, one can conclude on the basis of the expression (6) that for a sufficiently large mass flow steam content (x) the pressure head of natural circulation is practically independent of a variation in the entrance velocity or enthalpy in the evaporator zone. It is evident that in this case analysis of the stability of natural circulation of the coolant can be reduced to an investigation of the stability of forced circulation with a constant pressure differential on the lift section of the circulation loop. After linearization and neglect of the pressure differential on the evaporator zone one can write Eq. (3) in the form

$$\Delta H_{n.c.} = 2\Delta P_{ent}^*\frac{\Delta u_{ent}}{u_{ent}^*} + \int_0^{h_{t.s.}} \xi_{t.s.}\frac{u_{t.s.}^{*2}}{v_{t.s.}^*}\left(2\,\frac{\Delta u_{t.s.}}{u_{t.s.}^*} - \frac{\Delta v_{t.s.}}{v_{t.s.}^*}\right)dz + 2\Delta P_{ex}^*\,\frac{\Delta u_{ex}}{u_{ex}^*} - \Delta P_{ex}^*\,\frac{\Delta v_{ex}}{v_{ex}^*}, \tag{7}$$

where ΔP_{ent} is the total pressure differential at the drop tube and the entrance to the lift section, $\Delta P_{t.s.}$ and ΔP_{ex} are the pressure differentials on the traction section and at its exit, $u_{t.s.}$ and $v_{t.s.}$ are the velocity and specific volume of the coolant on the traction section, $\xi_{t.sec}$ is the hydrualic drag coefficient of the traction section, u_{ex} and v_{ex} are the velocity and specific volume of the coolant at the exit from the traction section, and $h_{t.s.}$ is the height of the traction section.

With formula (5) and the solution of Eq. (1) for the traction section taken into account, one can write the expression for Δv_{ex} as follows:

$$\Delta v_{ex} = v'\,\frac{M-1}{r}\,W_1(p)\exp(-p\tau_{t.s})\,\Delta u_{ent}. \tag{8}$$

We shall bear in mind that in the steady regime the velocity and specific volume of the coolant in the traction section do not depend on the spatial coordinate. Then using the solution of the linearized Eq. (2), we find on the basis of Eq. (7) with the expression (8) taken into account the transfer function to be

$$W_3(p) = \Delta u_{ent}/\Delta H_{n.c.} = u_{ent}^*\Big/\left\{2\left(\Delta P_{ent}^* + \frac{\Delta P_{t.s.}^* + \Delta P_{ex}^*}{m}\right) - \right.$$

$$\left. \frac{u_{ent}^*(M-1)}{mr}\,W_1(p)\left[\Delta P_{t.s.}^*\,\frac{1-\exp(-p\tau_{t.s.})}{p\tau_{t.s.}} + \Delta P_{ex}^*\,\exp(-p\tau_{t.s.})\right]\right\}. \tag{9}$$

By multiplying the transfer functions (5), (6), and (9), we obtain the characteristic equation ($W_1 W_2 W_3 = 1$), the arrangement of whose roots determines the stability of the steady regime:

$$\eta = -K(p), \tag{10}$$

where

$$\eta = 2\left(\Delta P_{ent}^* + \frac{\Delta P_{t.s.}^* + \Delta P_{ex}^*}{m}\right);$$

76

$$K(p) = \frac{(v/u)^*}{(\partial v/\partial t)} \left[\frac{1-\exp(-\lambda \ln m)}{\lambda} \right] \left[\frac{u_{\text{ent}}^{*}(M-1)}{mr} \right] \left\{ \left(\frac{\Delta P_{\text{ent}}^{*} + \Delta P_{\text{t.s.}}^{*} + \Delta P_{\text{ex}}^{*}}{m-1} + \right. \right.$$

$$\left. \left. + \Delta P_{\text{t.s.}}^{*} \right) \left[\frac{1-\exp(-p\tau_{\text{t.s.}})}{p\tau_{\text{t.s.}}} \right] + \Delta P_{\text{ex}}^{*} \exp(-p\tau_{\text{t.s.}}) \right\}.$$

One can write a sufficient stability condition for Eq. (10) as:

$$\Pi > (m-2)/(2m-1), \tag{11}$$

where

$$\Pi = \Delta P_{\text{ent}}^{*} / (\Delta P_{\text{t.s.}}^{*} + \Delta P_{\text{ex}}^{*}).$$

It is not difficult to show that in the case in which water with the saturation enthalpy enters the entrance to the lift section the static hydraulic characteristic of the loop does not have a decreasing section. Consequently, aperiodic instability of the coolant flow rate is eliminated in the loop. We note that for sufficiently large values of m the inequality (11) coincides with the stability condition of a boiling channel with forced circulation for the case of a steam—water mixture at the channel exit and a constant heat flux to the coolant [3].

The characteristic equation (10) was obtained by neglecting the pressure differential in the evaporator zone (ΔP_{ev}). However, the value of ΔP_{ev} in a Field tube can be comparable to the pressure difference in the drop section. In this connection we shall derive a characteristic equation with ΔP_{ev} taken into account. Equation (10) contains both noninertial terms caused by variation of the input velocity of the coolant and inertial ones caused by the time lag in the variation of the specific volume of the coolant upon a change in its input velocity. The noninertial terms are combined in the expression (10) in the coefficient η, and the inertial ones are combined in the transfer function K(p). We shall estimate the contribution of the pressure differential in the evaporator zone to η and K(p), respectively. With this aim we write the expression for ΔP_{ev} in the form

$$\Delta P_{\text{ev}} = \int_0^1 \xi_{\text{ev}} \frac{u_{\text{ev}}^2}{v_{\text{ev}}} \, dl, \tag{12}$$

where $l = z/h_{\text{ev}}$, ξ_{ev} is the hydraulic drag coefficient of the evaporator section, and u_{ev} and v_{ev} are the velocity and specific volume of the coolant in the evaporator zone.

Next we taken into account that

$$u_{\text{ev}} = u_{\text{ent}}(t) + u_{\text{ent}}^{*}(m-1) \, l; \tag{13}$$
$$v_{\text{ev}}^{*} = v' \, [1 + (m-1) \, l].$$

Then linearizing Eq. (12) with the expressions (13) and (4) taken into account, we determine the contribution to the increase in the pressure differential in the evaporator zone, respectively, from a change in the coolant velocity

$$2\Delta P_{\text{ev}}^{*} \left(\frac{2}{m+1} \right) \frac{\Delta u_{\text{ent}}}{u_{\text{ent}}^{*}} \tag{14}$$

and from a change in the specific volume of the coolant

$$\Delta P_{\text{ev}}^{*} \left(\frac{m-1}{m+1} \right) \frac{\Delta u_{\text{ent}}}{u_{\text{ent}}^{*}}. \tag{15}$$

We note that the expression (15) is obtained in the quasistatic approximation of the processes in the evaporator zone, i.e., the relationship

$$\Delta v_{\text{ev}} = -v' \, (m-1) \, l \, \frac{\Delta u_{\text{ent}}}{u_{\text{ent}}^{*}}$$

was used. With the expression (14) taken into account, the coefficient η in Eq. (10) will take the form

77

$$\eta_1 = 2 \left(\Delta P^*_\text{ent} + \frac{\Delta P^*_\text{t.s.} + \Delta P^*_\text{ex}}{m} + \frac{2}{m+1} \Delta P^*_\text{ev} \right). \tag{16}$$

By making use of the expression (15), the transfer function K(p) in Eq. (10) can, with the pressure differential in the evaporator zone taken into account, be written in the form

$$K_1(p) = \Delta P^*_\text{ev} \left(\frac{m-1}{m+1} \right) L(p) + K(p), \tag{17}$$

where L(p) is some quasipolynomial for which the bound $|L(p)| \leqslant 1$ for Re $p \geqslant 0$ is valid.

By using the expressions (16) and (17), we obtain the characteristic equation in final form

$$\eta_1 = - K_1(p). \tag{18}$$

One can write the sufficient condition of stability for Eq. (18) as follows:

$$\Delta P^*_\text{ent} > \left(\frac{m-2}{2m-1} \right) (\Delta P^*_\text{t.s.} + \Delta P^*_\text{ex}) + \left(\frac{m-5}{m+1} \right) \left(\frac{m}{2m-1} \right) \Delta P^*_\text{ev}. \tag{19}$$

Substituting the parameters of the steady regime of the Field steam-generating tube of an installation with a BN-350, we find that the sufficient condition of stability is satisfied with a reserve. The latter is in agreement with the results of experiments cited in [2]. We note that the stability reserve obtained on the assumption of an absence of input underheating of the coolant indicates the possibility of providing for stability of natural circulation in a Field tube with moderate input underheatings of the coolant. However, one should bear in mind that as the input underheating increases a decreasing section may appear on the static hydraulic characteristic of the circulation loop.

Second Case. Since boiling of the coolant occurs only at the entrance end of a zone with heat supply, we shall neglect the length of the evaporator zone. In this approximation the characteristic Eq. (10) takes the form

$$\eta = - K_2(p), \tag{20}$$

where

$$K_2(p) = \frac{\Delta I^*_\text{t.h.}(M-1)}{mr} \left[\frac{1 - \exp(-p\tau_\text{ed})}{p\tau_\text{ec}} \right] \left\{ \left(\frac{\Delta P^*_\text{ent} + \Delta P^*_\text{t.s.} + \Delta P^*_\text{ex}}{m-1} + \Delta P^*_\text{t.s.} \right) \left[\frac{1 - \exp(-p\tau_\text{t.s.})}{p\tau_\text{t.s.}} \right] + \Delta P^*_\text{ex} \exp(-p\tau_\text{t.s.}) \right\}.$$

Here $\Delta I^*_\text{t.h.}$ denotes the total heating of the coolant in the heated section of the loop, ΔP^*_ent denotes the total pressure differential in the drop section, at the entrance to the lift section, and in the zone with heat supply, and τ_ec denotes the time for the coolant to pass through the economizer section in the steady regime.

Next we taken into account that the main pressure losses in a loop of natural circulation with strong input underheating of the coolant usually occur in sections of the loop occupied by water. In other words, $\Delta P^* \gg (\Delta P^*_\text{t.s} + \Delta P^*_\text{ex})$. For this case one can write on the basis of Eq. (20) the sufficient condition of stability in the form

$$2r [1 + (M-1) x] x > \Delta I^*_\text{t.h.}. \tag{21}$$

Substituting the parameters given in [1] for an experimental loop of natural circulation of the coolant into the expression (21), we verify that the inequality (21) is not satisfied when x = 1.3%, but the steady regime is stable when x = 2%.

The authors are grateful to A. L. Prigorovskii for a discussion of the article.

LITERATURE CITED

1. F. M. Mitenkov et al., At. Engerg., 52, No. 4, 227 (1982).
2. P. L. Kirillov et al., Teploenergetika, No. 1, 7 (1982).
3. E. F. Sabaev, Comparison Systems for Nonlinear Differential Equations and Their Application in Reactor Dynamics [in Russian], Atomizdat, Moscow (1980).

METHODS OF CALCULATION OF THE STRESS—STRAIN STATE OF MICROFUEL ELEMENTS
OF HIGH-TEMPERATURE HELIUM-COOLED REACTORS AND THE CHOICE OF THEIR DESIGN

N. N. Ponomarev-Stepnoi, T. A. Sazykina,   UDC 621.039.548
and N. I. Tikhonov

The use of microfuel elements with pyrocarbon and carbide cladding in high-temperature helium-cooled reactors (HTHR) determined, as is known, the advantage of these reactors with respect to temperature, energy release, and safety as compared to reactors using conventional metal-clad rod fuel elements. Microfuel elements are usually in the form of a spherical fuel core with a diameter of 0.1-0.8 mm, onto which a cladding of several layers is deposited (Fig. 1). In order to determine the efficiency of microfuel elements, taking account of the hermeticity requirements on the cladding as well as the characteristic features of the radiation behavior of the pyrocarbon and carbides, we must carry out special investigations, including computational, of the stress-strain state of the claddings of microfuel elements during operation.

Methods of calculation of clad microfuel elements, which have been developed fairly intensively recently [1-5], make it possible to determine the stress—strain state of microfuel elements with a different number of coatings when a number of different assumptions and simplifications are made. The most complete method of calculation is described in a paper by Walther [5]. Calculations by this method, however, are very laborious and require a large expenditure of computer time since numerical methods of computations are used. Except for the one considered in [5], these models do not describe the stress—strain state of microfuel elements with mutlilayer deformable coatings. In this paper we present a number of programs for the calculation of microfuel elements with different coatings, using analytic methods of calculation, without the considerable simplifications characteristic of [1-4]; moreover, the computer programs are less laborious than the method proposed in [5].

The mathematical model of the computation is based on the following assumptions: the core is in the shape of a sphere and is surrounded by spherically symmetrical coatings; the inner coating of porous pyrocarbon does not bear a mechanical load and transfers all stresses normal to its surface directly to the force coating of dense pyrocarbon; the elastic constants of the coating materials are isotropic and do not change during irradiation; bombardment with fast neutrons causes anisotropic changes in the size of the pyrocarbon coating.

The stress—strain state of microfuel elements is calculated using the classical methods of the theory of elasticity which are based on equilibrium and compatibility equations and the equations for the principal laws of deformation. The solution is carried out in a spherical system of coordinates. The principal laws of deformation are in the form

$$\varepsilon_r^{(i)} = \varepsilon_r^{(i)e} + \eta_r^{(i)} + \int_0^\gamma \dot{\varepsilon}_{cr}\, d\gamma'; \qquad \varepsilon_\theta^{(i)} = \varepsilon_\theta^{(i)e} + \eta_\theta^{(i)} + \int_0^\gamma \dot{\varepsilon}_{c\theta}\, d\gamma',$$

where i is the number of the layer; $\varepsilon_r^{(i)}$ and $\varepsilon_\theta^{(i)}$, deformation of the i-th layer in the radial and tangential directions; γ, neutron fluence; and $\varepsilon_r^{(i)e}$ and $\varepsilon_\theta^{(i)e}$, elastic components of the deformation according to Hooke's law:

$$\varepsilon_r^{(i)e} = -\frac{2\nu_i}{E_i}\, \sigma_0^{(i)}(r,\, \gamma) + \frac{1}{E_i}\, \sigma_r^{(i)}(r,\, \gamma);$$

$$\varepsilon_\theta^{(i)e} = \frac{1-\nu_i}{E_i}\, \sigma_0^{(i)}(r,\, \gamma) - \frac{\nu_i}{E_i}\, \sigma_r^{(i)}(r,\, \gamma);$$

here ν_i is the Poisson ratio of the i-th layer; E_i, modulus of elasticity of the i-th layer; $\eta_r^{(i)}$ and $\eta_\theta^{(i)}$, contributions to the total deformation from the dimensional changes caused in the coating materials by irradiation which are approximated as a polynomial in the fluence; and $\int_0^\gamma \varepsilon_c d\gamma$, creep deformation.

In accordance with the published data for pyrocarbon we assume a linear dependence of the rate of creep deformation on the stresses,

$$\dot{\varepsilon}_{cr}^{(i)} = \frac{\partial \varepsilon_{cr}^{(i)}}{\partial \gamma} = -2K_c^{(i)} \nu_c^{(i)} \sigma_\theta^{(i)}(r,\gamma) + K_c^{(i)} \sigma_r^{(i)}(r,\gamma);$$

$$\dot{\varepsilon}_{c\theta}^{(i)} = \frac{\partial \varepsilon_{c\theta}^{(i)}}{\partial \gamma} = K_c^{(i)}(1-\nu_c^{(i)})\sigma_\theta^{(i)}(r,\gamma) - K_c^{(i)} \nu_c^{(i)} \sigma_r^{(i)}(r,\gamma),$$

where $\gamma_c^{(i)}$ is the Poisson ratio for creep and $K_c^{(i)}$ is the radiation creep constant.

The general solution of these equations and the equilibrium and compatibility equations has the form

$$\sigma_r^{(i)}(r,\gamma) = A_i(\gamma) + B_i(\gamma) r^{-3} + \frac{2}{3} f_i(\gamma) \ln r;$$

$$\sigma_\theta^{(i)}(r,\gamma) = A_i(\gamma) - \frac{1}{2} B_i(\gamma) r^{-3} + \frac{1}{3} f_i(\gamma)(2\ln r + 1),$$

where $A_i(\gamma)$ and $B_i(\gamma)$ are unknown functions, r is the running radius, and

$$f_i(\gamma) = \frac{E_i}{1-\nu_i} \exp(-D_i \gamma) \int_0^\gamma \dot{\eta}^{(i)}(\gamma') \exp(D_i \gamma') d\gamma;$$

$$D_i(\gamma) = \frac{E_i K_c^{(i)}}{1-\nu_i}(1-\nu_c^{(i)});$$

$$\eta^{(i)}(\gamma) = \eta_r^{(i)}(\gamma) - \eta_\theta^{(i)}(\gamma);$$

$$\dot{\eta}^{(i)}(\gamma) = \frac{d\eta^{(i)}(\gamma)}{d\gamma}.$$

To determine the unknown functions we must consider the boundary conditions

$$\sigma_r^{(1)}(a_1, \gamma) = -p(a_1, \gamma);$$

$$\sigma_r^{(i)}(b_i, \gamma) = \sigma_r^{(i+1)}(a_{i+1}, \gamma);$$

$$u^{(i)}(b_i, \gamma) = u^{(i+1)}(a_{i+1}, \gamma);$$

$$i = 1 \text{ to } (n-1);$$

$$\sigma_r^{(n)}(b_n, \gamma) = -\Pi,$$

where n is the number of layers, a_1 is the inner radius, b_1 is the outer radius, $p(a_1, \gamma)$ is the internal pressure of accumulated gases, and Π is the external pressure of the matrix on the cladding.

It is assumed that there are no stresses at the initial fluence $\gamma = 0$. The pressure of gaseous fission products is calculated as the sum of the partial pressures of the gases released by the material of the core as a result of the [235]U fission reaction. The main contribution to the total pressure is made by Xe and Kr:

$$p(a_1 \gamma) = \sum_J p_J, \quad J = \text{Kr, Xe.}$$

The value of p_J is calculated from the Redlich–Kuong equation of state which was recommended for high values of the temperature and pressure [6]

$$p_J = \frac{RT}{V_J - q_J} - \frac{s_J}{V_J(V_J + q_J)\sqrt{T}},$$

80
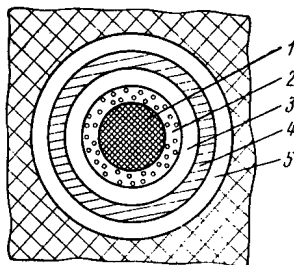
Fig. 1. Design of HTHR microfuel
elements: 1) core; 2) buffer layer;
3) first force layer PyC; 4) sec-
ond force layer of SiC; 5) third
force layer of PyC.

where R is the universal gas constant, T is the operating temperature, V_J is the molar vol-
ume of the gas, and q_J and s_J are constants of the equation of state.

At the I. V. Kurchatov Institute of Atomic Energy a package of programs in FORTRAN has
been written for the BESM-6 computer for calculating the stress—strain state for different
designs of microfuel elements [7]. Each program is a procedure for calculating the stresses
and strains which arise in different coatings, depending on the fluence of fast neutrons.
A program (dubbed LIN-2) for the calculation of the stress—strain state of microfuel ele-
ments with three deformable layers has recently been developed and perfected: In the event
of a fracture in one or two layers a switch is made to the subprogram BISON (two layers) or
KASATKA (one layer), respectively. The kinetics of the changes in the stress—strain state
is determined mainly by the joint action of three physical processes, viz., the release of
gaseous fission products, radiation-induced changes in the dimensions, and the creep of the
pyrocarbon. This package of programs was used to investigate the kinetics of the stressed
state. In calculations with one of the versions we assumed the following parameters for the
microfuel element:

Core: UO_2, diameter 500 μm, density 8.0 g/cm³, porosity 0.1, enrichment 21%.

Buffer layer from pyrocarbon: thickness 70 μm, density 1.0 g/cm³, porosity 0.6.

First force layer of dense pyrocarbon: thickness 60 μm, density 1.8 g/cm³, $E_1 = 2.9 \cdot 10^5$ MPA, $\nu_1 = 0.33$, $\nu_c^{(1)} = 0.4$, $K_c^{(1)} = 4.1 \cdot 10^{-25}$ (neutrons/cm²·MPa)⁻¹.

Second force layer of silicon carbide: thickness 40 μm, density 3.2 g/cm³, $E_2 = 3.2 \cdot 10^7$ MPa, $\nu_2 = 0.25$, $\nu_c^{(2)} = 0.25$, $K_c^{(2)} = 0.001 \cdot K_c^{(1)}$.

Third force layer of dense pyrocarbon: thickness 50 μm, density 1.8 g/cm³, $E_3 = 2.9 \cdot 10^5$ MPa, $\nu_3 = 0.33$, $\nu_c^{(3)} = 0.4$, $K_c^{(3)} = 4.1 \cdot 10^{-25}$ (neutrons/cm²·MPa)⁻¹.

At a fast-neutron fluence of $1.2 \cdot 10^{21}$ neutrons/cm² the burn-up was 10% of the heavy
atoms. The calculated curves of the stress state as a function of fast-neutron fluence,
on condition that all the force layers remain whole, are presented in Fig. 2a. In the
first force layer PyC-1 the stresses on both the inner and outer surfaces are tensile. When
the irradiation begins these stresses increase and then undergo relaxation, which is due to
the action of radiation creep. In the third force layer PyC-3 the stresses are also tensile
and at a fluence greater than $0.5 \cdot 10^{21}$ neutrons/cm² they remain practically constant. This
is explained by the fact that the second force layer SiC-2 is more rigid ($E_{SiC} \gg E_{PyC}$) and
restricts the possible displacement of the layer PyC-3, and as a result of this the action
of radiation creep counterbalances the stresses. In the second force layer of silicon car-
bide there are compressive stresses which decrease as the fluence increases. We consider
the stressed state in the case when the pyrocarbon layers are broken (see Fig. 2b). If the
first force layer is fractured when the stresses in it reach 100 MPa (tensile strength of
pyrocarbon $[\sigma]_{PyC}$ = 100-200 MPa), the stresses in the layers change abruptly. In the
layer SiC-2 the compressive stresses decrease while in the layer PyC-3 the tensile
stresses increase slightly. If it is assumed that the third force layer can break when the
maximum value of stresses is attained, then the stresses in SiC-2 pass into the tensile re-
gion and increase with the fluence. Upon completion of the irradiation the stresses do
not exceed 50 MPa, which is substantially below the breaking strength ($[\sigma]_{SiC}$ = 300-400 MPa).

81
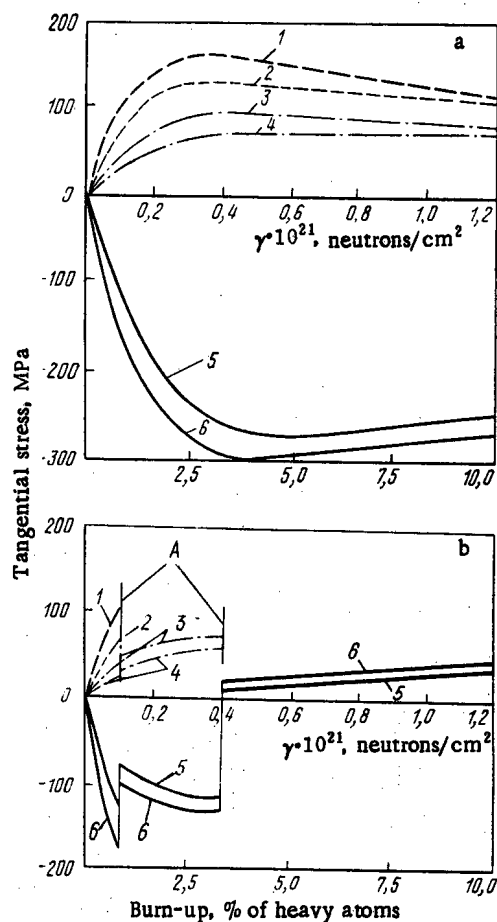
Fig. 2. Stressed state as a function of the fast-neutron fluence: 1, 2) inner and outer surfaces of PyC-1 layer; 3, 5) inner and outer surfaces of PyC-3 layer; 4, 6) outer and inner surfaces of SiC-2 layer (A denotes fracture of the layer).
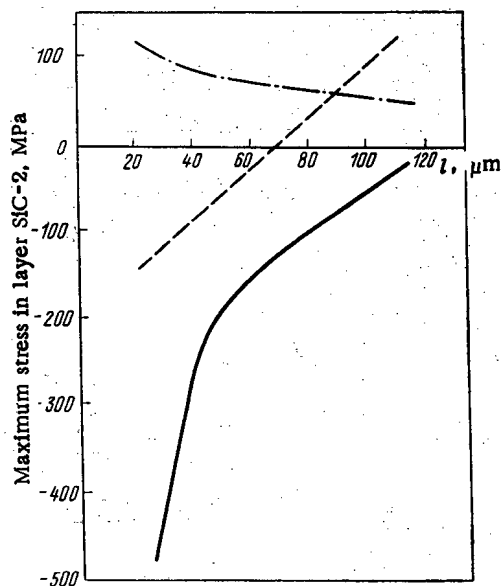
Fig. 3. Maximum stress in the layer SiC-2 as a function of the thickness l of the layer for different states of the other force layers: ——) layers PyC-1 and PyC-3 remain whole; ---) layer PyC-1 is broken, layer PyC-3 is not broken; -•-•-) layers PyC-1 and PyC-3 are broken.

82

Thus, fracture of the pyrocarbon layers does not lead to the direct fracture of the microfuel element as a whole. The main force layer is the silicon carbide layer. The fitness of a microfuel element for use, therefore, should be assessed with allowance for the stressed state that arises in the silicon carbide layer during irradiation. It must be pointed out, however, that when the first pyrocarbon layer is broken there is an increased probability of damage to the silicon carbide layer as a consequence of bombardment with fission products, corrosion, and the possible interaction of the core with the coating, all of which together lead to a decrease in its efficiency.

The design of the microfuel element, clearly, in many ways determines its stressed state. Using the package of programs developed, we investigated the influence of the design parameters of the microfuel element on its stress-strain state. As an example, Fig. 3 shows how the maximum stress in SiC-2 depends on the thickness of this layer. A decrease in the thickness leads to an increase in the compressive stresses and this may cause the layer to fracture under compression. When the layer PyC-1 is broken the compressive forces are substantially lower but when both PyC layers are broken tensile stresses arise in the layer SiC-2, substantially increasing the probability of the microfuel element fracturing. If the thickness of the layer SiC-2 is increased, fracture of the first force layer also leads to tensile stresses in SiC-2. To ensure that the microfuel element functions reliably, we must determine the optimum range for the thickness of each layer, considering the stressed state of the silicon carbide layer when the PyC layers are broken and when they are whole, assuming the same probability of fracture for both tensile and compressive stresses.

Thus, analysis of the kinetics of the stress-strain state of a microfuel element allows us to note an interesting feature of the operation of this microfuel element under the conditions of irradiation. Radiation changes in the dimensions of the pyrocarbon layers ensure that these coatings exert a compressive effect on the intermediate SiC layer, making it highly fit for work. This factor is so significant that, despite the substantial pressure of gaseous fission products and technological gases, the SiC layer turns out in fact to be unloaded during operation. And only when the pyrocarbon layers are broken at the end of the operating period does fracture of the SiC layer because of tensile stresses become possible.

The fact that reliable leakproofness can be ensured along with a high allowable temperature and heat release as well as the possibility of using mass-production technology to fabricate microfuel elements and spherical fuel elements are clear indicators of the undoubted future prospects for this type of fuel element.

LITERATURE CITED

1. J. Prodos and I. Scott, Nucl. Appl., 2, 402 (1966).
2. J. Kaae, J. Nucl. Mater., 29, 249 (1969).
3. P. Morgand, J. Lanier, and M. Boulon, in: Proceedings Second International Conference "Structural Mechanics in Reactor Technology," Berlin (1973), Vol. C, Paper C1/2.
4. S. A. Balankin et al., At. Energ., 45, No. 3, 205 (1978).
5. H. Walther, Nucl. Eng. Design, 18, No. 1, 11 (1972).
6. K. Shah and G. Thodos, Industr. Eng. Chem., 57, 3 (1965).
7. T. A. Sazykina and N. I. Tikhonov, Problems of Atomic Science and Engineering, Series on Atomic-Hydrogen Power Engineering and Technology, No. 3(10), 59 (1981).

SORPTION OF RADIOACTIVE IODINE BY STAINLESS STEEL FROM A
FLOW OF NITROGEN TETROXIDE VAPOR

V. M. Dolgov and M. A. Drugachenok   UDC 621.039.56

The concentrations of iodine radionuclides in gaseous coolants (helium or carbon dioxide) are largely determined by the sorption of the radioiodine on the inner surfaces of power-reactor loops [1, 2], and this gives interest to similar measurements on the systems with gas—liquid cycles based on dissociating nitrogen tetroxide (N_2O_4) [3].

We have examined the uptake of radioiodine on stainless steel from a gas flow with the apparatus of Fig. 1 at 338-753°K and 0.12 MPa; the mode of flow was laminar. The liquid radioactive nitrogen tetroxide tagged with radioiodine was produced directly in an evaporator by adding a few drops of an aqueous solution of $Na^{131}I$ to the N_2O_4, the latter solution not containing stable iodine nuclides. Then the specific activity of the mixture was about 4×10^7 Bq/kg. Then the tetroxide was evaporated at 10^{-5} kg/sec and passed in sequence through the experimental units (EU) and a protective column containing a radioiodine absorber, after which it was condensed and collected.

The sorption dynamics could be examined with the EU-1, whose design allowed one to record the radioactivity during the experiment. A major component of the EU-1 was a tube coil made of OKh18N10T steel, through which the radioiodine-tagged N_2O_4 was passed for 1 h at the given temperature. At the end of the EU-1 operation, the radioactivity in the protective column was measured together with the volume of condensed nitrogen tetroxide, after which the EU-1 was flushed with pure nitrogen tetroxide not containig ^{131}I. The radioactivity was measured with a scintillation counter. The radioiodine activity on the inner surface and within the volume of the EU-1 was calculated in relative terms from

$$n_v = a_v V = \frac{K_1 N_0 v_j V}{V_0 v_g} \; ; \tag{1}$$

$$n_s = a_s S_1 = n_{s+v} - n_v, \tag{2}$$

where n_v, n_s, n_{s+v} are the bulk, surface, and overall radioactivities of the iodine in the EU-1 in sec^{-1}, while a_v and a_s are the volume and surface specific radioactivities of the EU-1 in $m^{-3} \cdot sec^{-1}$ and $m^{-2} \cdot sec^{-1}$, V_1 and S_1 are the volume and internal surface of the EU-1 in m^3 and m^2, N_0 is the radioactivity in the guard column in sec^{-1}, V_0 is the volume of the N_2O_4 condensate in m^3, v_g and v_j are the specific volumes of N_2O_4 in the gaseous and liquid states in $m^3 \cdot kg^{-1}$, and K_1 is a coefficient that corrects for the difference in measurement conditions for the EU-1 and the guard column (determined by experiment).

Figure 2 shows how the activity of the EU-1 varies with time. Table 1 gives the activities of ^{131}I in the volume and at the inner surface of the EU-1.

It was found that the uptake of iodine from the gaseous nitrogen tetroxide on the stainless steel was virtually completely reversible up to 400°K. Equilibrium set in very rapidly in the bulk-surface system, which enabled us to describe the uptake by means of a distribution coefficient Γ given by $\Gamma = a_s/a_v$.

There was appreciable irreversible radioiodine uptake above 420°K; the accumulation on the inner surface is described by

$$da_s/dt = \omega a_v - (\lambda + \delta) a_s,$$

where ω and δ are the sorption and desorption rate constants in m/sec^{-1} and sec^{-1}, while λ is the radioactive decay constant in sec^{-1}.

Fig. 1

Fig. 2
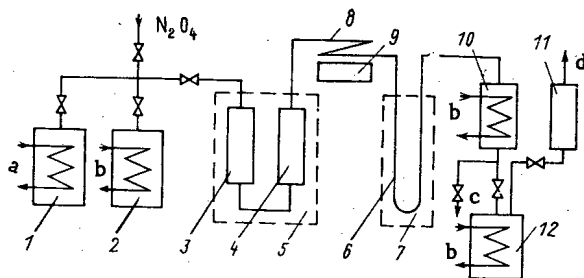
Fig. 1. Scheme for the experimental unit: 1, 2) evaporators; 3) conditioning column; 4) EU-2; 5) air thermostat; 6) guard column; 7) heater; 8) EU-1; 9) scintillation counter; 10) condenser; 11) neutralizer; 12) condensate collector; a) water for heating evaporators; b) cooling water; c) to vacuum pump; d) vent.
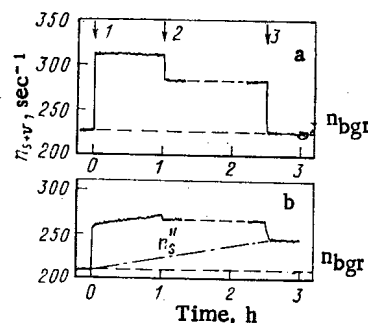
Fig. 2. Time dependence of the radioactivity in the EU-1 at temperatures of 338°K (a) and 418°K (b); 1, 2) start and end of passage of radioactive gas; 3) start of passage of nonradioactive gas.

The solution to this equation with the initial condition $a_s(0) = 0$ for a_v = const is

$$a_s = \frac{\omega a_v}{\lambda + \delta} [1 - e^{-(\lambda + \delta)t}].$$

In the initial period, when $(\lambda + \delta)t \ll 1$, we have

$$a_s \approx \omega a_v t.$$

These equations enable one to determine the sorption rate constant; Table 1 gives the values obtained for ω and Γ.

The sorption rate constants were measured in experiments with 0Kh18N10T steel for temperatures above 470°K. Some of the specimens had previously been oxidized in N_2O_4 at 675°K and 1 MPa for 100 h. The specimens were set up within the interchangeable EU-2, through which the gas containing radioiodine was passed for 2 h at a given temperature. After the end of the gas passage, we measured the radioactivity of the specimen and the guard column, as well as the volume of condensed nitrogen tetroxide, from which we calculated the sorption rate by the use of (3) from the formula

$$\omega = n_s V_0 v_g K_2 / S_0 N_0 v_j t,$$

where S_0 is the surface area of the specimen in m^2 and K_2 is a coefficient determined by experiment to correct for the difference in measurement conditions for the specimen and the guard column.

Table 2 gives values of the rate constant averaged within a temperature range of width 100°K (the bounds to the confidence ranges $\Delta\omega$ correspond to $\alpha = 0.95$).

In spite of the spread in the results, one sees that there are larger rate constants for the oxidized surface and no tendency for the values to decrease as the temperature rises, whereas the rate constants for unoxidized surfaces decrease in the range 473-753°K. The rate constants for uptake by stainless steel from gaseous nitrogen tetroxide are less by about an order of magnitude under comparable conditions than those for air, where the value is about 5×10^{-5} m/sec [4].

One can identify the nature of the bond between the radioiodine and the surface by using the basic criteria (temperature range and sorption and desorption rates) indicating differences between chemical and physical sorption [5]. The results indicate that at up to 400°K, physical sorption predominates; above 400°K, one gets stronger chemisorption. The chemical interactions of iodine with the components of stainless steel (Cr, Mn, Fe, Ni, Mo) have been

85

TABLE 1. Results of Experiments on Radio-
iodine Sorption

Temp., K	n_D, sec^{-1}	n_s, sec^{-1}		r, m	ω, m/sec
		n'_s*	n''_s		
388	65,8	47,9	—	$1,5 \cdot 10^{-3}$	—
338	48,9	44,8	—	$1,8 \cdot 10^{-3}$	—
378	37,0	30,5	4,0	$1,7 \cdot 10^{-3}$	—
383	35,2	24,5	—	$1,4 \cdot 10^{-3}$	—
423	23,4	21,2	6,8	—	$\sim 10^{-7}$
428	29,0	22,1	11,0	—	$\sim 10^{-7}$
468	8,8	23,6	53,0	—	$4 \cdot 10^{-6}$

*n'_s and n''_s are the activities of the re-
versibly and irreversibly sorbed iodine.

TABLE 2. Radioiodine Uptake Rate Constants
$\times 10^6$, m/sec

T, К	Surface	
	oxidized	unoxidized
473—573	$3,7 \pm 2,4$	$1,6 \pm 0,8$
573—673	$5,7 \pm 3,5$	$1,0 \pm 0,5$
673—753	$10,3 \pm 6,3$	$0,4 \pm 0,3$

considered [6] in examining the compatibility of fuel-rod cladding with oxide fuel; it was found that the effects of oxygen on the stainless steel—iodine system are very substantial, since oxides of the metals in the alloy are formed, which are thermodynamically more stable than the iodides. Therefore, it is likely that the reduction in the rate constant as the temperature rises for unoxidized metal is due to competition between oxidation and the formation of iodine compounds.

The results enable one to evaluate the effects of radioiodine sorption on the distribution in a loop containing N_2O_4, which is necessary in designing systems for eliminating radioiodine and in determining the radiation environment in a nuclear power system.

LITERATURE CITED

1. J. Hillary, J. Brit. Nucl. Energy Soc., 2, No. 4, 443 (1973).
2. P. Rowland et al., Control of Iodine in the Nuclear Industry, Technical Reports Series, No. 148, Vienna, IAEA (1973), p. 57.
3. V. B. Nesterenko et al., Fast Reactors and Heat-Exchange Equipment for Nuclear Power Stations Using Dissociating Coolant [in Russian], Nauka i Tekhnika, Minsk (1978).
4. Yu. V. Sivintsev, At. Tekh. Rubezhom, No. 4, 26 (1966).
5. M. Aubert et al., J. Nucl. Mater., 58, No. 3, 257 (1975).
6. W. J. Thomas and J. N. Thomas, Introduction to Principles of Heterogeneous Catalysis, Academic Press (1964).

DAMAGE OF THE SURFACE OF STRUCTURAL MATERIALS BY THE ACTION OF PLASMOIDS

V. I. Pol'skii, B. A. Kalin, P. I. Kartsev,
D. M. Skorov, E. P. Fomina, Yu. V. Skvortsov,
N. M. Umrikhin, F. R. Khamidullin, S. S. Tserevitinov,
O. A. Kozhevnikov, A. N. Lapin, and N. B. Odintsov

UDC 621.039.531

In the operation of fusion machines the first wall of the working chamber will be subjected to considerable erosive action of the fusion plasma. Many of the results of such action (e.g., blistering and sputtering) have now been investigated fairly well [1-3]. However, the damage to the first-wall material from local evaporation, cracking, splitting off, and fusion of the surface, caused by the plasma flows and multiple absorption of a large amount of energy of the plasma radiation in machines having magnetic and inertial confinement, is a serious problem which has not been sufficiently investigated experimentally [3-5].

To determine the influence of the direct action of plasma on the destruction of the first wall we have investigated plasma-flow-initiated erosion of the surface of a broad class of promising structural materials for the chamber of a fusion reactor. The irradiation was carried out with flows of hydrogen and deuterium plasma, generated by the MK-200 pulsed plasma accelerator [6]. In the experiments we used two modifications of the accelerator: with a conical (Fig. 1) and a cylindrical electrode system. To transport the plasma to the place where the specimens were set up we used a cylindrical plasma guide in the form of a metal tube-liner (length 1.5 m, diameter 0.3 m, wall thickness $2 \cdot 10^{-3}$ m), made of stainless steel. The plasma was isolated from the walls by means of external solenoids which produced a longitudinal magnetic field inside the linear. The density and velocity of the plasma flow were determined by a set of techniques. The velocity of the hydrogen or deuterium component of the plasma and that of the impurity were measured by diamagnetic probes, i.e., two monochromators with photomultipliers, as well as by a Mach-Zender interferometer. The qualitative composition of the plasma was established with a mass spectrometer.

In the first series of experiments each specimen was subjected to the threefold action of a plasma flow. Irradiation in this case was carried out with hydrogen plasmoids in the accelerator with a cylindrical geometry of electrodes, which operated at a voltage $U_0 = 15$ kV ($W_{bat} = 125$ kJ). The total energy content of the flow per pulse at the site of the specimens was $W = 30$ kJ. The time dependence of the plasma velocity in a fixed cross section of the plasma guide from the time when the forward part of the flow passes and the radial distribution of the particle density are given in Fig. 2. According to estimates, the plasma temperature was $T_i \approx 100$ eV, which allowed the plasma to be considered to be fully ionized.

In the second series of experiments each of the specimens was subjected to the 30-fold action of flows of deuterium plasma in the accelerator with a conical geometry of the electrode system. The accelerator operated at a voltage $V_0 = 30$ kV ($W_{bat} = 500$ kJ); in this case the energy content of the flow in the cross section of the plasma guide at the site of the target was $W = 70$ kJ per pulse. The distribution of the plasma velocity over the length of the flow and the distribution of the particle density over the chamber radius for the accelerator with a conical electrode geometry are shown in Fig. 3. The main parameters of the plasma flows used in this paper and assumed at the wall in plasma disruptions in INTOR [7] and other reactors with magnetic confinement [8-11] as well as the products of microexplosions of the target in pulsed fusion reactors under design [4, 12] are given in Table 1. The table shows the main parameters of plasmoids used for earlier investigations on the "Prosvet" machine [13].

In the first and second series of experiments plasma flows were used to irradiate refractory metals and alloys based on them, chromium and chromium-nickel stainless steels,

87
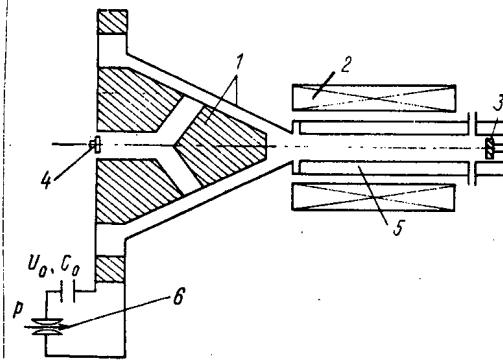
Fig. 1. Schematic diagram of irradiation with plasmoids in the
MK-200 accelerator: 1) system of electrodes with conical geom-
etry; 2) external solenoid; 3) holder with targets; 4) system
for pulsed admission of gas; 5) cylindrical plasma guide; 6)
discharger.
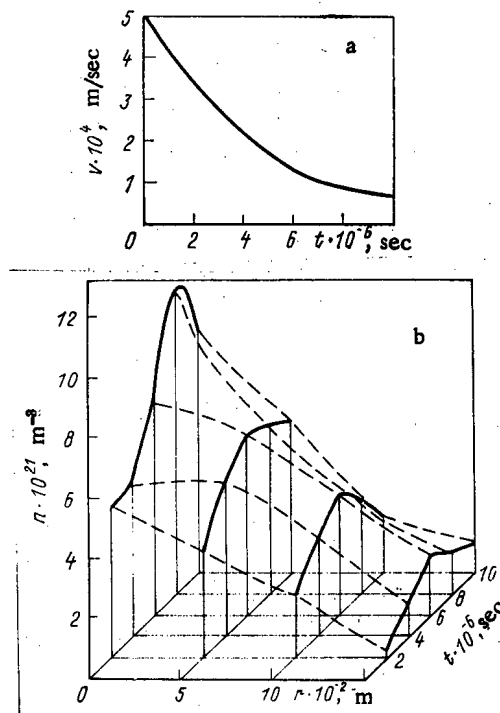
Fig. 2. Structure of plasma flow in the first series of irrad-
iations: a) time dependence of the plasma velocity in the on-
coming flow; b) particle-density distribution over the radius of
the plasma guide.

high-nickel alloys, titanium and its alloys, aluminum, aluminized steels, materials with
coatings, and coating materials (Table 2). The specimens of the material to be tested
were cut from thin plates with a thickness of $(0.3-1) \cdot 10^{-3}$ m and prior to irradiation were
annealed to remove the mechanical hardening. The surfaces of specimens without coatings
were polished electrolytically. The specimens were placed in special cassettes and sus-
pended in a holder attached to a cooled horizontal bar located at the spot where the plasma
flows emerged from the cylindrical plasma guide. The cassette and holder were made of stain-
less steel. After irradiation the specimens, cassettes, and holder were bent strongly with re-
spect to the direction to the plasma source, which was due to the thermal stress arising

88
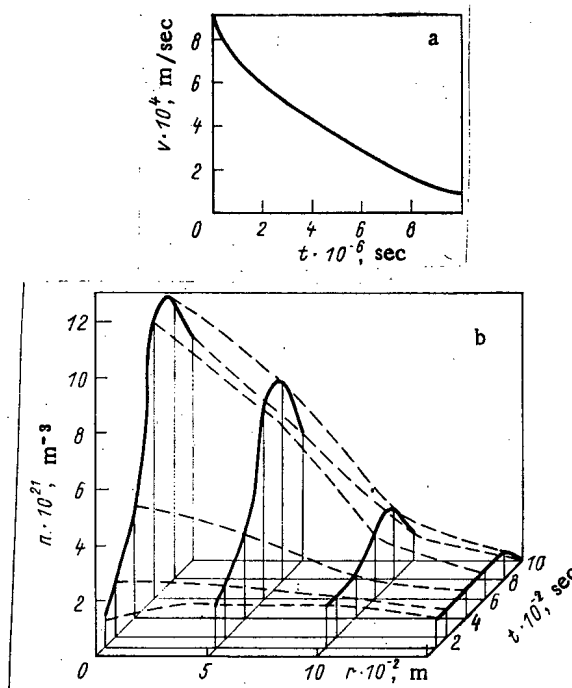
Fig. 3. Structure of the plasma flow in the second ser-
ies of experiments: a) time distribution of plasma vel-
ocity in the oncoming flow; b) distribution of the par-
ticle density over the radius of the plasma guide (the
notation along the axes is the same as in Fig. 2).

during cooling of the initially intensely heated thin surface layer [14]. Our estimates
showed that the value of the mechanical stress in the surface layer of the specimens ex-
ceeds the yield stress of the material. The strain was measured by the deflection. It
was established that the residual plastic strain is ∿1%. Repeated thermal shocks lead to
a build-up of residual strain and the deflection reaches 15% after 30 pulses.

Since the density of the plasma flow decreases along the radius of the plasma guide,
the irradiated specimens were set up at different distances from its axis. Analysis of the
experimental results showed that the degree of change of the surface of the irradiated
specimens depends on the form of the material and the irradiation parameters. Table 2
presents all of the materials tested and the forms of surface erosion observed. When the
target was irradiated by three pulses we observed considerable cracking of the surface
layer of refractory materials (first class of materials tested) along grain boundaries
(Fig. 4a). A similar effect occurred when niobium was irradiated with a lower intensity of
plasmoid and 100 times as many pulses [13]. Aluminum and titanium alloys (third and fourth
classes) were characterized by a substantial fusion of the specimens and the appearance of
drops of solidified metal and capillary waves on their surface (see Fig. 4b).

The greatest resistance to irradiation by plasma flows was displayed by carbon pyrocer-
amic and graphite (sixth class) whose surface practically did not change. The surface of
aluminum coatings, obtained by evaporation onto niobium, and aluminized 12Kh18N10T steel was
subjected to the greatest damage (see Fig. 4c), viz.: cracking, fusion, and the formation
of bulges with a diameter of $(1-5) \cdot 10^{-6}$ m resembling blisters. The stainless steels and
high-nickel alloys (second class) were relatively the most resistant; with the exception of
OKh16N15M3B powdered austenitic steels, they did not display any cracking or fusion on their
surface (see Fig. 4d).

Surface erosion of the materials of class 2 was characterized mainly by the presence
of blisterlike bulges. It must be pointed out that under irradiation with plasma flows high-
nickel alloys and chromium—nickel cast steels better conserved the initial state of their
surface than did other materials of this class, as expressed in a lower density of bulges
of equal average diameters. Chromium steels and OKh16N15M3B chromium—nickel steel made from
coarse-grained $(15 \cdot 10^{-5}$ m) powder cracked along grain boundaries in places. Such cracking

89

TABLE 1. Main Parameters of Plasma Flows

Parameter	Plasma disruption in magnetic fusion reactor		Microexplosion in pulsed fusion reactor	Simulation of process	
	INTOR [7]	PGFR [8] TFR [9] ETR [10] TFTR [11]	pulsed fusion reactor (design) [4] HIBALL [12]	"Prosvet" [13]	MK-200
Max. energy of ions (H^+, D^+), keV	1	10	150	2	5
Av. energy density of flow, J/m^2	$3 \cdot 10^6$	$0,7 \cdot 10^6$ [10] $2 \cdot 10^6$ [8]	$0,2 \cdot 10^6$	10^4	$(4 \div 10) \cdot 10^5$
Flow intensity, W/m^2	$3 \cdot 10^7$	$3,8 \cdot 10^8$ [10] $3 \cdot 10^8$ [9] $2,6 \cdot 10^{10}$ [8]	$10^8 - 10^{12}$	$5 \cdot 10^9$	$(3 \div 9) \cdot 10^{10}$
Density in main part of flow, m^{-3} Duration of action, sec	10^{20} $2 \cdot 10^{-3}$	10^{20} $1 \cdot 10^{-4}$ [10] $5 \cdot 10^{-4}$ [9] $(1 \div 10) \cdot 10^{-5}$ [8] $2 \cdot 10^{-4}$ [11]	10^{22} $10^{-9} - 10^{-5}$	$5 \cdot 10^{20}$ $2 \cdot 10^{-6}$	$(1 \div 5) \cdot 10^{21}$ $(1 \div 5) \cdot 10^{-5}$
Av. dose in pulse, ion/m^2 No. of pulses in computation period	$1 \cdot 10^{22}$ 10^3 in 15 years	— 450 in 3 years [10] 10^4 in 20 years [11] 500 in 2 years [8]	— 10^6 in 1 year	$6 \cdot 10^{19}$ 300	$1,4 \cdot 10^{22}$ 3—30
Max. temp. of wall heating, °K	600	400 [11] 700 [10]	700	—	—

TABLE 2. Classes of Materials Tested and the Form of Surface Erosion

Class	Material tested	Form of surface erosion	
		first series of irradiation	second series of irradiation
1. Refractory metals and alloys	MChVP (Mo), TsM-6 (Mo—Zr), TsM-10VD (Mo—Al), Mo—V	Cracking along grain boundaries	Cracking and local flashing-off
2. Stainless steel and high-nickel alloys	12Kh18N10T, cast and powdered 0Kh16N15M3B, 07Kh16N4B, cast and powdered Kh13M2; 03Kh20N45M4B4, and 03Kh20N45M4BRTs	Blisters and partial cracking (only in cast Kh13M2 steels and powdered steels of the type 0Kh16N15M3B)	Drops and waves of solidified metal, craters, cracking
3. Aluminum	A-999 (Al)	Flashing-off and cracking	The same
4. Titanium and its alloys	BTI-00 (Ti), PT-7M (Ti—Al—Zr)	Drops and waves of solidified metal	" "
5. Metals with coatings	Nb/Al (deposition), 12Kh18N10T/Al (aluminization)	Cracking, local flashing-off and blisters	" "
6. Coating materials	G-4 (graphite), SG-2 (glass-fiber-reinforced graphite), $Al_2O_3 + V_2O_3$, SiC, US-1 and USB-15 (carbon pyroceramic)	Without damage	Cracking

was not observed in the same grade of steel (0Kh16N15M3B) made from finer-grained ($2 \cdot 10^{-5}$ m) powder. Attention must be drawn to the comparatively high rupture strength of the surface in the case of chromium steels. In the case of Kh13M2 steels, obtained by ordinary casting methods with subsequent thermomechanical treatment, we observed slight cracking of the surface without the formation of bulges while powder chromium steels did not display any surface damage at all. A characteristic change in the topography of the surface of powder steels is the formation of double bulges with a regular round shape (see Fig. 4d). As noted during statistical processing of the micrographs, the ratio of the diameter of an upper bulge to the diameter of a lower bulge is 0.14 ± 10%.

To ascertain the nature of the bulges, using a diamond indenter on a PMT-3 microhardness meter with a minimum load we scratched a grid on the irradiated surface. Examination of the opened bulges (Fig. 5a) established that they are hollow and have a depth of $(1.2-2.3) \cdot 10^{-6}$ m.

Subsequent heating of the irradiated specimens in a vacuum led to the opening of the bulges as a result of the removal of their caps. Heating and holding the specimens at 870°K (see Fig. 5b) resulted in the formation of new, smaller bulges without destroying or changing the size of existing bulges. As a result of heating and holding at 1020°K (see Fig. 5c) the

90
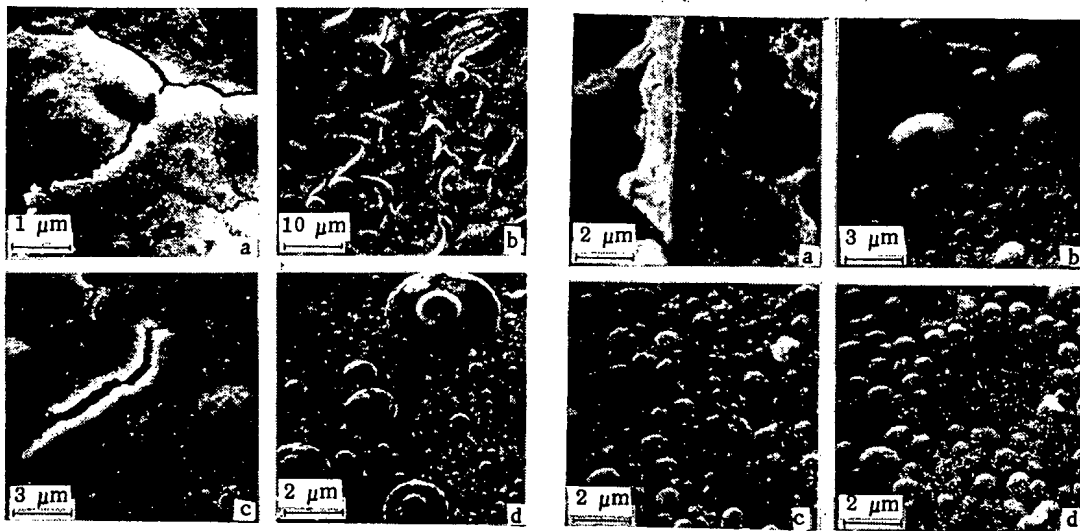
Fig. 4   Fig. 5

Fig. 4. Topography of surface of specimens of materials of different classes, irradiated with three pulses: a) TsM-6 alloy (first class); b) PT-7M alloy (fourth class); c) aluminized steel (fifth class); d) powdered 1Kh13M2 steel (second class).

Fig. 5. Structure of bulges on an irradiated surface, characteristic of the erosion of materials in the second class: a) opening of a bulge by an indenter [fine "shallow" (1-2 μm) scratches have been drawn on the surface; individual blisters have been caught by the indenter and removed; the bottom of the blister, cylindrical craters, and traces of plastic deformation from the indenter are visible]; b) formation of new bulges upon heating to 870°K in a vacuum; c) opening of initial bulges upon heating to 1020°K in a vacuum; d) uncovering of the partition between double bulges upon heating to 1300°K in a vacuum.

cupolas of the largest bulges were uncovered; when double bulges were present, at first the upper bulges were ruptured and then, upon heating to 1300°K, the separating partition between the double bulges was ruptured (see Fig. 5d). The density of the bulges increased constantly. This allows us to assume that the bulges are gas-filled cavities, i.e., blisters. A characteristic feature of the blistering observed was the greater depth of the gas-filled cavities, which was ten times the calculated [15] and experimental [16] ranges of ions of hydrogen and its isotopes for monoenergetic beams. Apparently, the considerable depth at which the cavities occur also determined the large diameters of the blisters, whose size was 4-10 times that ordinarily observed [17, 18]. Our finding that double blisters separated by a partition are formed indicates that each of the blisters was formed independently and, apparently, in succession.

Typical results of the investigation of the topography of the surface of specimens irradiated by a series of thirty pulses are shown in Fig. 6a, b. Characteristic damages to the surface of the material in this case consist of pronounced fusion of the surface layer to a depth of $(2-10) \cdot 10^{-6}$ m, the formation of craters and solidified drops of metal (classes 2 and 5), capillary waves (class 4), cracking (class 6), and cracking and local fusion (class 1). Similar damage was observed when the surface of some metals was acted upon by flows of dense metal plasma [19], streams of electrons [20], and laser beams [21] with an intensity of 10^{10} W/cm^2 or higher.

The investigation of the structure of the fused surface on transverse polished sections by scanning electron microscopy and x-ray structural analysis made it possible to determine some distinctive features of the structure of the fused layer. Metallographic etching did not reveal the microstructure of the layer and a sharp boundary was observed, without any zones of thermal influence between the layer and the main material (see Fig. 6c). A characteristic feature of all of the materials was that circular cavities oriented normal to the surface are formed in the fused layer. These cavities began at a depth of $2 \cdot 10^{-6}$ m and in

91
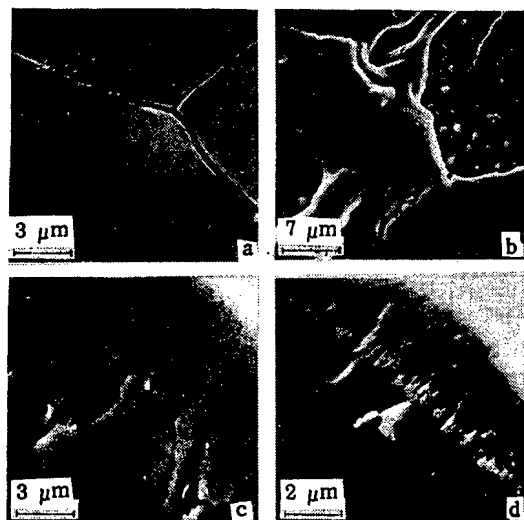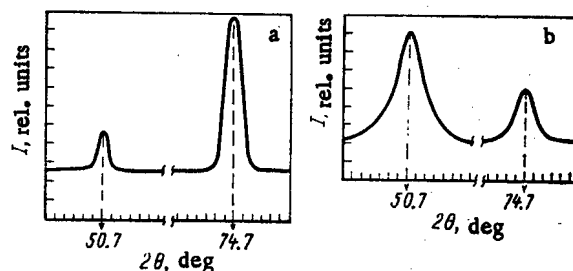
Fig. 6

Fig. 7

Fig. 6. Influence of thirtyfold irradiation by plasma flows on the structure of surface layers: a) topography of irradiated surface of USB-15 carbon py-roceramic (class 6); b) topography of irradiated surface of high-nickel alloy (class 2); c) transverse polished section of steel, etched to reveal the grain; d) acicular cavities in surface layer at a depth of $(1-2) \cdot 10^{-6}$ m.

Fig. 7. Diffraction patterns of the surface of 12Kh18N10T steel, obtained with radiation from an Fe anode (BSV-24) for unirradiated (a) and irradiated (b) specimens.

some cases emerged on the surface, forming craters on it (see Fig. 6d). X-ray structural analysis indicated the crystalline nature of the fused layer. The plasma flows, however, altered the texture of the surface layer, bringing it to complete recrystallization and the formation of a pseudoamorphous layer, which followed from the redistribution and smearing of the maxima on the diffraction pattern (Fig. 7a, b).

From what has been said above we can make the following main conclusions:

Irradiation with plasma flows possessing the energy indicated above causes a change in the surface of promising structural materials for fusion reactors (proportional to the energy of the flows and the number of irradiations) in the form of cracking along grain boundaries, formation of gas-filled blisters, and fusion of the surface layer to a depth of as much as $10 \cdot 10^{-6}$ m.

In the case of irradiation with a small number of pulses the typical result is the formation of two-layered blisters, having an anomalously large size and deep-lying gas cavities.

Irradiation with plasma flows possessing a specific energy of 10^7-10^8 $W \cdot cm^{-2}$ from the MK-200 pulsed plasma accelerator makes it possible to simulate the action of plasma on the first wall of a fusion reactor.

LITERATURE CITED

1. B. A. Kalin, D. M. Skorov, and V. L. Yakushin, Problems of Atomic Science and Engineering, "Physics of Radiation Damage and Radiation Materials Science" Series [in Russian], No. 2(13), 72 (1980).
2. M. I. Guseva, Yu. V. Martynenko, and N. V. Pleshivtsev, in: Research on and Development of Materials for Fusion Reactors [in Russian], Nauka, Moscow (1982), p. 106.
3. W. Bostick et al., J. Nucl. Mater., 63, 356 (1976).
4. B. P. Maksimenko, At. Tekh. Rubezhom, No. 5, 27 (1980).
5. G. M. Gryaznov et al., in: Research on and Development of Materials for Fusion Reactors [in Russian], Nauka, Moscow (1982), p. 71.
6. N. V. Goryacheva et al., in: Proceedings of Fifth All-Union Conference on Plasma Accelerators and Ion Injectors [in Russian], Nauka, Moscow (1982), p. 14.

7. International Tokamak Reactor. Phase One. Report of the International Tokamak Reactor Workshop organized by the International Atomic Energy Agency (held in seven sessions in Vienna during 1980 and 1981). Panel Proceedings Series. IAEA, Vienna (1982).
8. C. Traschel, D. Bowers, and B. Cramer, J. Nucl. Mater., 85/86, 203 (1979).
9. TER Group, "Thermal load on the TER Tokamak limiter during additional heating pulses and major plasma disruptions," J. Nucl. Mater., 105, 62 (1982).
10. W. Becraft et al., Fusion Technol., 32, 63 (1979).
11. TFTR Project, in: Information Bulletin on Foreign Publications [in Russian], No. 4, Atomizdat, Moscow (1978), p. 52.
12. B. P. Maksimenko, "INPORT — an improved method of protecting the first wave of pulsed fusion reactors," At. Energ. Rubezhom, No. 10, 13 (1982).
13. A. G. Belikov et al., At. Energ., 51, No. 6, 376 (1981).
14. R. Behrisch, J. Nucl. Mater., 85/86, 1047 (1979).
15. A. F. Burenkov et al., Preprint IAÉ-3332/11, Institute of Atomic Energy, Moscow (1980).
16. O. Shuichi, K. Toyoaki, and A. Hedeo, Jpn. J. Appl. Phys., 18, No. 3, 465 (1979).
17. Yu. V. Martynenko, Preprint IAÉ-3145, Institute of Atomic Energy, Moscow (1979).
18. V. M. Gusev and M. I. Guseva, in: Interaction of Atomic Particles with a Solid. Part I [in Russian], Minsk Radiotechnical Inst. (1978), p. 3.
19. E. T. Anfinogenov et al., in: Proceedings of Second All-Union Conference on the Engineering Problems of Fusion Reactors, Vol. 4 [in Russian], A. D. Efremov Scientific-Research Institute of Electrophysical Apparatus, Leningrad (1982), p. 69.
20. B. A. Demidov, G. S. Knizhnik, and Yu. F. Tomashchuk, Fiz. Khim. Obrab. Mater., No. 4, 114 (1982).
21. V. S. Kraposhin, Poverkhnost'. Fiz., Khim., Mekh., No. 3, 1 (1982).

A SPECTROPHOTOMETRIC STUDY OF THE EQUILIBRIUM IN THE REACTION

$PuO_2^{2+} + Cl^- \rightleftarrows PuO_2^+ + \frac{1}{2} Cl_2$ IN A NaCl—2CsCl MELT

S. K. Vavilov, G. N. Kazantsev,   UDC 546.799.4-143:543.42
and O. V. Shishalov

Spectrophotometric studies have been made on the reaction

$$PuO_2^{2+} + Cl^- \rightleftarrows PuO_2^+ + 1/2 Cl_2 \tag{1}$$

for LiCl—CsCl melts [1] and indicate that hexavalent plutonium is of relatively low stability in chloride melts, as is evident from the nearly zero value of the conditional formal redox potential for the PuO_2^{2+}/PuO_2^+ pair relative to a chlorine reference electrode.

It is of interest to extend the study of (1) to mixtures of alkali-metal chlorides in order to obtain a fuller conception of the chemical behavior of oxidized forms of plutonium containing oxygen in salt electrolytes. One expects an improvement in the stability of the hexavalent state in the series from lithium chloride to cesium chloride, as has been found for quadrivalent plutonium [2-4].

Here we report results on the thermodynamics of (1) for NaCl—2CsCl melt derived by spectrophotometry of the equilibrium concentrations of pentavalent and hexavalent plutonium for various values of the chlorine partial pressure (in mixtures with oxygen) and at various temperatures.

Experiment. The equilibrium concentrations of pentavalent and hexavalent plutonium were measured at various chlorine partial pressures with an IKS-14A spectrophotometer equipped for working with molten salts [5]. The solvent was an NaCl—2CsCl eutectic (T_{mp} = 495°C) made by melting the individual salts of chemically pure grade and purified from traces of oxygen and water by treating the melt with hydrogen chloride and chlorine. The density was calculated from the equation [6]
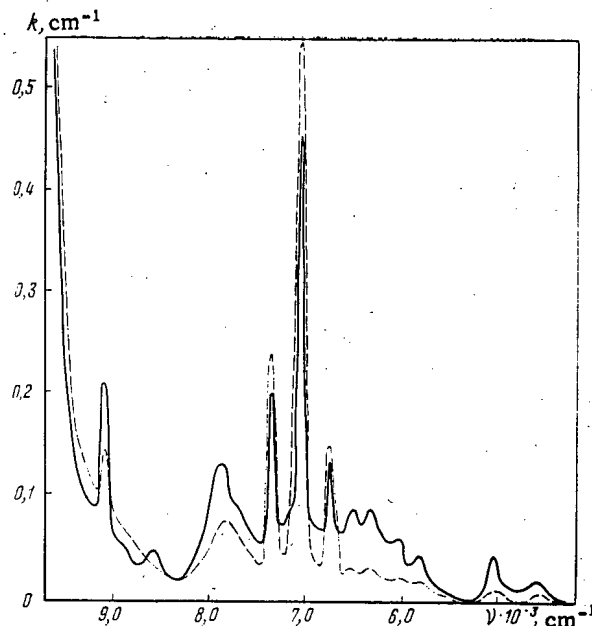
Fig. 1. Spectra of a NaCl — 2CsCl melt containing equilibrium concentrations of pentavalent and hexavalent plutonium at 550°C and $C_{Pu} = 0.192$ mole/liter: ——) $P_{Cl_2} = 0.1 \cdot 10^5$ Pa; ---) $P_{Cl_2} = 1.0 \cdot 10^5$ Pa.
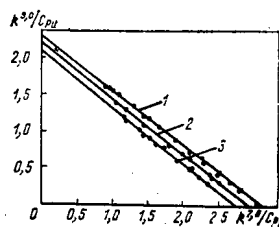
Fig. 2. Graphical check on (5) for (1) 550, (2) 650, (3) 750°C.

$$d = 3.175 - 10.01 \cdot 10^{-4} \, T. \qquad (2)$$

Plutonium was introduced as the trichloride, which was synthesized by the action between plutonium dioxide (purity 99.5-99.7%) and carbon tetrachloride vapor at 600°C. The initial solutions of the pentavalent and hexavalent plutonium oxychlorides were made by oxidizing the trivalent plutonium with a mixture of oxygen (40-90 vol.%) and chlorine (60-10 vol.%).

The reaction vessel was a quartz spectrophotometer cell ($l = 1$ cm) fitted with a vacuum tube PTFE plug with a loading device and a central inlet for the gas tube. The temperature in the cell was maintained to ±2°. The oyxgen—chlorine mixtures were produced in a steel gasholder. The chlorine partial pressure varied from 0.1×10^5 to 1.0×10^5 Pa with an error of not more than ±3%.

Methods. The plutonium trichloride was introduced into the melt to give an overall concentration of 0.1-0.3 mole/liter. Then the oxygen—chlorine mixture was bubbled through the melt to oxidize the reduced forms of plutonium to the oxychlorides and to establish equilibrium between the pentavalent and hexavalent forms. The absorption spectrum was recorded over the range 12,000-4000 cm^{-1} periodically. The melt was treated until the absorption bands of trivalent and quadrivalent plutonium disappeared and a stable spectrum was obtained for the

94

TABLE 1. Values of the Molar Extinction Coefficients ε_5 and ε_6 for Pentavalent and Hexavalent Plutonium in Molten NaCl—2CsCl

ε, liter/mole·cm	T, °C		
	550	650	750
ε_5 ($v = 9090$ cm^{-1})	2,3±0,1	2,2±0,2	2,1±0,2
ε_6 ($v = 7040$ cm^{-1})	3,1±0,2	2,9±0,2	2,7±0,2

TABLE 2. Dependence of the Ratio of the Equilibrium Concentrations of Pentavalent and Hexavalent Plutonium on the Oxygen Relative Partial Pressure at Various Temperatures in a NaCl—2CsCl Melt

$\lg P_{Cl_2}$	550 °C			650 °C			750 °C		
	m	$\frac{C_5}{C_6}$	$-\lg \frac{C_5}{C_6}$	m	$\frac{C_5}{C_6}$	$-\lg \frac{C_5}{C_6}$	m	$\frac{C_5}{C_6}$	$-\lg \frac{C_5}{C_6}$
—1,000	3	0,42±0,06	0,375	—	—	—	—	—	—
—0,698	4	0,29±0,04	0,532	2	0,49±0,04	0,319	—	—	—
—0,522	4	0,26±0,03	0,582	4	0,40±0,04	0,394	4	0,56±0,06	0,252
—0,398	4	0,21±0,03	0,685	2	0,38±0,05	0,426	2	0,50±0,06	0,305
—0,222	3	0,19±0,02	0,720	2	0,31±0,04	0,516	2	0,42±0,05	0,375
—0,000	6	0,13±0,02	0,868	8	0,22±0,02	0,656	4	0,30±0,03	0,532

Note: m is the number of experimental points and $C_5 = C_{PuO_2^+}$; $C_6 = C_{PuO_2^{2+}}$.

mixture of plutonium oxychlorides, which indicated that equilibrium had been attained in (1). Then the melt was treated with chlorine to produce equilibrium in (1) at a chlorine partial pressure of 1.01×10^5 Pa. In that case, there was partial reduction of the plutonium oxychlorides to the trivalent and quadrivalent states, which resulted in the absorption band of quadrivalent plutonium at 5300 cm^{-1}. The concentration of the reduced forms of plutonium was calculated at 750°C [4] and in this way we corrected for the reduction in the overall plutonium concentration in the oxychloride form.

Results and Discussion. Figure 1 shows absorption spectra for the NaCl—2CsCl melt containing equilibrium concentrations of pentavalent and hexavalent plutonium as recorded at various chlorine partial pressures. It is evident from Fig. 1 that the strength of the band with its peak at 7040 cm^{-1}, which relates to hexavalent plutonium [7, 8], decreases as the chlorine content of the gaseous reagent falls. On the other hand, the intensity of the band peaking at 9090 cm^{-1}, which relates to pentavalent plutonium [7, 8], increases.

The spectrum does not contain a band peaking at 4300 cm^{-1}, which is characteristic of quadrivalent plutonium, which indicates that the reduced forms Pu^{3+} and Pu^{4+} were absent [4]. Therefore, the reduction of hexavalent plutonium occurs in accordance with (1) as the chlorine concentration falls.

Neither pentavalent nor hexavalent plutonium was produced in pure form in the NaCl—2CsCl melt, and therefore it was impossible to determine the molar extinction coefficients directly, which are required in calculating the equilibrium concentrations in (1). However, if the bands peaking at 9090 and 7040 cm^{-1} obey Beer's law, the concentrations of pentavalent and hexavalent plutonium can be expressed as follows:

$$C_{PuO_2^+} = k^{9.0}/\varepsilon_5; \quad C_{PuO_2^{2+}} = k^{7.0}/\varepsilon_6, \tag{3}$$

where $C_{PuO_2^+}$, $C_{PuO_2^{2+}}$ are the concentrations of those forms correspondingly in mole/liter, $k^{9.0}$ and $k^{7.0}$ are the absorption parameters at 9090 and 7040 cm^{-1} as determined by the baseline method in cm^{-1}, and ε_5 and ε_6 are the molar extinction coefficients of pentavalent and hexavalent plutonium at 9090 and 7040 cm^{-1} correspondingly in liter/mole·cm.

95

TABLE 3. Values of the Exponent to P_{Cl_2} and of the Conditional Equilibrium Constant of $PuO_2^{2+} + Cl^- \rightleftharpoons PuO_2^+ + 1/2\ Cl_2$ in a NaCl—2CsCl Melt

T, °C	m †	Exponent to P_{Cl_2}	$-\lg K^*$	K^*
550	24	0,49±0,02	0,87±0,05	0,135±0,016
650	18	0,48±0,02	0,65±0,04	0,225±0,025
750	12	0,49±0,02	0,41±0,04	0,38±0,04

†Number of experimental points.

TABLE 4. Values of the Conditional Redox Potential for the PuO_2^{2+}/PuO_2^+ Pair Relative to a Chlorine Reference Electrode

Solvent	$(E^*_{PuO_2^{2+}/PuO_2^+} - E_{Cl_2/Cl^-})$, V			
	500 °C	550 °C	650 °C	750 °C
LiCl — CsCl (45 mole %) †	—0,116	—0,106	—0,081	—0,056
NaCl — 2CsCl (66 mole %) ‡	—0,164	—0,150	—0,122	—0,094

†Calculated from the data of [1].
‡Our results.

The overall concentration of the oxygen-bearing forms of plutonium $C_{PuO_2^{n+}}$ in the melt is

$$C_{PuO_2^{n+}} = C_{PuO_2^+} + C_{PuO_2^{2+}} = \frac{k^{9.0}}{\varepsilon_5} + \frac{k^{7.0}}{\varepsilon_6}.$$

(4)

On transforming (4) we get

$$\frac{k^{9.0}}{C_{PuO_2^{n+}}} = \varepsilon_5 - \frac{\varepsilon_5}{\varepsilon_6} \frac{k^{7.0}}{C_{PuO_2^{n+}}}.$$

(5)

In fact, in a plot in $k^{9.0}/C_{PuO_2^{n+}} - k^{7.0}/C_{PuO_2^{n+}}$ coordinates (Fig. 2), the experimental points lie almost exactly on straight lines, which confirms that Beer's law applies to both absorption bands. The interceptor on the ordinate is numerically equal to the molar extinction coefficient for pentavalent plutonium at 9090 cm⁻¹ ($k^{7.0}/C_{PuO_2^{n+}} = 0$; $k^{9.0}/C_{PuO_2^{n+}} = \varepsilon_5$), while the interceptor on the abscissa is equal to that for hexavalent plutonium at 7040 cm⁻¹ ($k^{7.0}/C_{PuO_2^{n+}} = 0$; $k^{9.0}/C_{PuO_2^{n+}} = \varepsilon_5$).

Table 1 gives these molar extinction coefficients for the bands at 9090 and 7040 cm⁻¹, which have been used in calculating the equilibrium concentrations in the NaCl—2CsCl melt in (1).

The conditional equilibrium constant of (1), namely K*, can be expressed as

$$K^* = \frac{C_{PuO_2^+}}{C_{PuO_2^{2+}}}\ P_{Cl_2}^{1/2},$$

(6)

where P_{Cl_2} is the relative partial pressure of chlorine in the gas mixture (referred to the standard pressure of 1.01×10^5 Pa).

On transforming (6) and taking logarithms we get

$$\lg \frac{C_{PuO_2^+}}{C_{PuO_2^{2+}}} = \lg K^* - 1/2 \lg P_{Cl_2},$$ (7)

which was used to calculate K*.

Table 2 shows the dependence of the observed $C_{PuO_2^+}/C_{PuO_2^{2+}}$ on the relative chlorine partial pressure and the temperature, while Table 3 gives values for the exponent to P_{Cl_2} together with the conditional equilibrium constant of (1) as calculated by least squares from (7) with the data of Table 2. Table 3 indicates that the relative chlorine partial pressure has an exponent close to 0.5 in the expression for the equilibrium constant of (1).

The temperature dependence of the equilibrium constant for (1) is described satisfactorily by

$$\lg K^* = 1.42 - 1900/T \pm 0.05.$$ (8)

From (8) we calculated the conditional formal redox potential of the PuO_2^{2+}/PuO_2^+ pair relative to a chlorine reference electrode

$$E_{PuO_2^{2+}/PuO_2^+} = \frac{2.3RT}{nF} \lg K^* = -0.380 + 2.8 \cdot 10^{-4}T \pm 0.01 \text{ v}$$ (9)

and the change in the conditional standard Gibbs energy for reaction (1) in a NaCl — 2CsCl melt

$$\Delta G^* = -2.3RT \lg K^* = 36000 - 27T \pm 1000 \text{ J/mole.}$$ (10)

From (10) we get that the change in entropy and the heat effect in (1) are correspondingly

$$\Delta S^* = 27 \pm 2 \text{ J/(mole·K)}$$

$$\Delta H^* = 36000 \pm 2000 \text{ J/mole.}$$

These results indicate that the stability of hexavalent plutonium in a NaCl—2CsCl melt decreases as the temperature rises, as for a LiCl—CsCl melt [1], as is evident from the increase in the equilibrium constant of (1). The stability of hexavalent plutonium in a NaCl—2CsCl melt is somewhat higher than that in LiCl—CsCl, because the conditional redox potential for the PuO_2^{2+}/PuO_2^+ pair is more negative (Table 4).

LITERATURE CITED

1. G. Landresse and G. Dhyckaerts, Inorg. Nucl. Chem., 10, No. 11, 1059 (1974).
2. G. Landresse and G. Dhychaerts, ibid., No. 8, 675.
3. G. Landresse and G. Dhyckaerts, ibid., No. 11, 1051.
4. S. K. Vavilov, G. N. Kazantsev, and V. V. Gushchin, At. Energ., 19, No. 2, 94 (1980).
5. V. V. Gushchin and V. M. Barinov, Prib. Tekh. Eksp., 3, 279 (1972).
6. M. V. Smirnov, V. P. Stepanov, and T. Mukatov, in: Papers from the Institute of Electrochemistry [in Russian], Issue 16, Ural Science Center, Academy of Sciences of the USSR, Sverdlovsk (1972), p. 16.
7. X. Smanson, J. Phys. Chem., 68, 438 (1964).
8. S. K. Vavilov et al., in: Abstracts for the Fifth All-Union Conference on Molten-Salt Physical Chemistry and Electrochemistry, Part 1 [in Russian], Ural Science Center, Acadecmy of Sciences of the USSR (1973), p. 67.

NEUTRON LEAKAGE FROM A CHANNEL WITH A LOW DENSITY OF
FISSIONABLE MATERIAL

B. P. Kochurov

UDC 621.039.512.4

The square of the neutron migration length in a medium with a hollow cylindrical channel can be expressed in the form

$$M^2 - M^2_{mod}\{1 + \varepsilon[1 + (2 - p)\,\rho/l]\},\tag{1}$$

where $\varepsilon = \pi\rho^2/V_{cell}$, ρ is the channel radius, and l is the neutron mean free path in the moderator. For $p = 0$ Eq. (1) is known as the Behrens formula [1] (as noted in [2] a similar result was derived by S. L. Sobolev and independently by V. S. Fursov in 1948). The deviation of the neutron flux distribution from linear (cosinusoidal) in a reactor of height H led to the following values of p:

p = 3π²ρ/4H (Davison's result given in [3]);

$$p = [3\pi^2/4 - 3/2 + 3\pi\,Si\,(\pi)/2]\,\rho/H \quad [2].\tag{2}$$

The method of images [5-7] was employed in [4] to derive interpolation formulas for M^2 which took account of terms in p for channels with a nonzero scattering cross section. In the Benoist theory the formula for the square of the neutron migration length in the axial direction

$$M^2 = \int l_z^2 (\Sigma_s N + q)\,dr \Big/ \Big(2 \int \Sigma_a N\,dr\Big),\tag{3}$$

where l_z^2 is the projection on the z axis of the mean-square displacement of neutrons before the first collision, was transformed so as not to contain the neutron source q explicitly. This can be done, for example, by considering the diffusion of thermal neutrons only. In this case neutron production and absorption occur in the same regions, and by using the balance relations and neglecting terms of order $\alpha^2 M^2$, q can be approximated by $\Sigma_a N$. In considering the migration of neutrons of all energies, Σ_s in Eq. (3) must be understood as the scattering cross section $\Sigma_s(E' \to E)$, and q must be replaced by the density of fission neutrons $\chi(E)\,\nu\Sigma_q N(E')$ with integration with respect to E. Fission neutrons begin migration in the channel, and are "absorbed" (slowed down) in the moderator. If the mean free path of fast neutrons $l_{ch} \to \infty$, it is easy to see [7] that l_z^2 contains terms which diverge as $\ln \rho/l_{ch}$.

In the present article we consider the problem of calculating the part of the square of the migration length M^2_1 from the instant of production in the channel to the first collision in the moderator. By l we understand the neutron mean free path averaged over all values of the energy, for example, over the fission spectrum. An expression is obtained for M^2_1. Instead of the method of images, a more accurate method was used [2], based on the direct calculation of neutrons. It is assumed that the neutron mean free path in the channel is infinite, $\rho/H \ll 1$, $l/H \ll 1$, and the channels are far apart, so that it is sufficient to consider the problem of an individual channel in a reactor of height H. The neutron source distribution in the channel has the form $\sin \alpha(z + \delta)$, where $\alpha = \pi/(H + 2\delta)$, and $\delta = 2l_0/3$.

Thus, we consider the limiting case when the neutron mean free path in the channel is infinite. The neutron current from the reactor per neutron created in the channel is by definition related to the square of the migration length M^2_1 by the equation $I = I_1 + I_2 = \alpha^2 M^2_1$, where I_1 is the neutron current through the end of the channel S_1 (Fig. 1), and I_2 is the neutron current through the surface S_2 adjacent to it, with

---
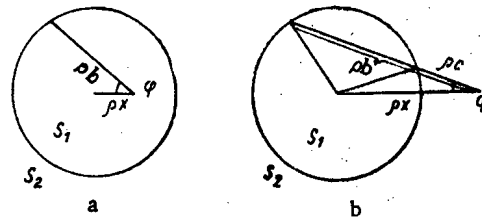
Fig. 1. Geometrical data: S_1) cross section of channel; S_2) moderator; x, c, b, φ) variables.

$$I_1 = (\alpha/2\pi \cos \alpha\delta) \int\limits_0^1 x\, dx \int\limits_0^{2\pi} d\varphi \left(\int\limits_0^{\theta_0} d\theta \int\limits_0^{H/\cos\theta} dr + \int\limits_{\theta_0}^{\pi/2} d\theta \int\limits_\theta^{\rho b/\sin\theta} dr \right) \sin\theta \cos\theta \sin\alpha\, (z+\delta). \tag{4}$$

By making the change of variables (x, φ) → (σ, b), where $\sigma = \sqrt{1 - x^2 \sin^2 \varphi}$ and $b = x \cos \varphi + \sigma$,

$$\int\limits_0^1 x\, dx \int\limits_0^{2\pi} d\varphi f(x, \varphi) = 2 \int\limits_0^1 \frac{\sigma\, d\sigma}{\sqrt{1-\sigma^2}} \int\limits_0^{2\sigma} db f_1(\sigma, b), \tag{5}$$

we can find the first part of integral (4) by using Eq. (A1) of the Appendix:

$$j_1 = (\alpha^2\rho^2/2\pi^2)(1 + 4\alpha\delta/\pi) + O(\alpha^4\rho^4). \tag{6}$$

After integrating over r and making the substitution u = αρb cot θ, the second part of integral (4) is reduced to the integral

$$j_2 = (\alpha^2\rho^2/2\pi \cos \alpha\delta) \int\limits_0^1 x\, dx \int\limits_0^{2\pi} d\varphi b^2 \int\limits_0^{\pi - 2\delta\alpha} \frac{du}{[(\alpha\rho b)^2 + u^2]^{3/2}} [\cos \alpha\delta - \cos (u + \alpha\delta)]. \tag{7}$$

The first integral in Eq. (7) is

$$j_2^{(1)} = (1/2)[1 - (\alpha^2\rho^2/2\pi)(1 + 4\alpha\delta/\pi)] + O(\alpha^4\rho^4). \tag{8}$$

We expand the integrand in the second part of (7), rearrange the limits of the integral with respect to u

$$\left[-\left(\int\limits_0^\infty - \int\limits_{\pi-2\delta\alpha}^\infty \right) \cos \alpha\delta \cos u + \left(\int\limits_0^\infty - \int\limits_{\pi-2\delta\alpha}^\infty \right) \sin \alpha\delta \sin u \right] du/[(\alpha\rho b)^2 + u^2]^{3/2} \tag{9}$$

and write it as the sum $j_2^{(2)} + \Delta j_2^{(2)} + j_2^{(3)} + \Delta j_2^{(3)}$. Using Eqs. (A1), (A3), and (A4),

$$j_2^{(2)} = -1/2 + \alpha^2\rho^2/16 - (\alpha^2\rho^2/4) \ln(\gamma\alpha\rho/4) + O(\alpha^4\rho^4); \tag{10}$$

$$j_2^{(3)} = (4/3\pi^2)\alpha^2\rho\delta - \pi\alpha^3\rho^2\delta/8 + O(\alpha^4\rho^4) \quad [\text{cf. (A5)}]. \tag{11}$$

The remaining integrals are evaluated by using Eqs. (A6)–(A8):

$$\Delta j_2^{(2)} = (\alpha^3\rho^2/4)[\text{Ci}(\pi) - 1/\pi^2] - \alpha^3\rho^2\delta/\pi^3 + O(\alpha^4\rho^4); \tag{12}$$

$$\Delta j_2^{(3)} = (\alpha^3\rho^2\delta/4)[1/\pi - \text{Si}(\pi)]. \tag{13}$$

The sum of Eqs. (6), (8), (10), (11), and (12) determines the neutron leakage through the surface S_1:

$$I_1 = (\alpha^2\rho^2/4) \ln(H/2\rho) + 4\alpha^2\delta\rho/3\pi + \alpha^3\rho^2\delta[3/4\pi - \pi/8 - \text{Si}(\pi)] + O(\alpha^4\rho^4). \tag{14}$$

99

The neutron current through the surface S_2 is

$$I_2 = (\alpha/2\pi \cos \alpha \delta) \int_1^\infty x\, dx \int_{-\arctan 1/x}^{\arctan 4x} d\varphi \left(\int_{\theta_1}^{\theta_0} d\theta \int_{\rho c/\sin \theta}^{H/\cos \theta} dr + \int_{\theta_0}^{\pi/2} d\theta \int_{\rho c/\sin \theta}^{\rho b/\sin \theta} dr \right) \times \tag{15}$$

$$\times \sin \theta \cos \theta \exp(-\rho c/\sin \theta) \sin \alpha\, (z+\delta),$$

where $\theta_0 = \arctan(b/H)$, and $\theta_1 = \arctan(\rho c/H)$. After integrating with respect to r and making the substitution $(x, \varphi) \to (\sigma, c)$, where $\sigma = \sqrt{1 - x^2 \sin^2 \varphi}$, $c = x \cos \varphi - \sigma$, $b = x \cos \varphi + \sigma$, and interchanging the order of integration with respect to θ and c, Eq. (15) is reduced to the three integrals

$$j_3 = (1/\pi \cos \alpha \delta) \int_0^1 \frac{\sigma\, d\sigma}{\sqrt{1-\sigma^2}} \int_0^{\pi/2} \sin \theta\, d\theta \int_0^{H \operatorname{tg} \theta/\rho} dc \cos(\alpha \rho c \cot \theta + \delta) \exp(-\rho c/l \sin \theta); \tag{16}$$

$$j_4 = 1/\pi \int_0^1 \frac{\sigma\, d\sigma}{\sqrt{1-\sigma^2}} \left(\int_0^{\arctan 2\rho\sigma/H} d\theta \sin \theta \int_0^{H \operatorname{tg} \theta/\rho} dc \exp(-\rho c/l \sin \theta) + \right. \tag{17}$$

$$\left. + \int_{\arctan 2\rho\sigma/H}^{\pi/2} d\theta \sin \theta \int_{H \operatorname{tg} \theta/\rho - 2\sigma}^{H \operatorname{tg} \theta/\rho} dc \exp(-c/l \sin \theta); \right.$$

$$j_5 = (-1/\pi \cos \alpha \delta) \int_0^1 \frac{\sigma\, d\sigma}{\sqrt{1-\sigma^2}} \int_{\arctan 2\rho\sigma/H}^{\pi/2} d\theta \sin \theta \int_0^{H \tan\theta/\rho - 2\sigma} dc \cos \alpha\, [\rho\,(c+2\sigma) \cot \theta + \delta] \exp(-\rho c/l \sin \theta). \tag{18}$$

Simple calculations lead to the result

$$j_3 = (l/4\rho)(1 - \alpha^2 l^2/4 - 4\alpha^2 l\delta/3\pi) + O(\alpha^4 \rho^4); \tag{19}$$

$$j_4 = \alpha^2 \rho^2 l/2\pi^2 H + O(\alpha^4 \rho^4). \tag{20}$$

Values of j_5 expressed in the form

$$j_5 = (8\alpha^3 \rho^2/\pi) \int_0^1 \frac{\sigma^4\, d\sigma}{\sqrt{1-\sigma^2}} \int_0^{\pi - 2\delta\alpha} du \sum_{i=1}^7 a_i f_i(u) \tag{21}$$

are listed in Table 1 ($v^2 = h^2 + u^2$; $h = 2\alpha\rho\sigma$).

Using Eqs. (A9)-(A13),

$$I_2 = \alpha^2 (l^2/6 + l_0 l/6 + \rho l/3 - l\rho^2 \pi^2/8H) + O(\alpha^4 \rho^4). \tag{22}$$

The final result follows from Eqs. (14) and (22):

$$M_i^2 = (l^2/3)\,[(1 + l_0/l)/2 + (1 + 8l_0/3\pi l)\rho/l + (3\rho^2/4l^2)\ln(H/2\rho) - (3\pi^2 \rho^2/8lH)(1 + l_0/3l)]. \tag{23}$$

If the nonuniformity of the first-collision density is neglected, a formula for M^2 can be constructed as the sum of Eqs. (1) and (23), with the condition that in Eq. (1) M_{mod}^2 is replaced by $M_{mod}^2 - l^{2/3}$.

APPENDIX

The following relations were used:

$$\int_0^1 x\, dx \int_0^{2\pi} b^2(\varphi)\, d\varphi = \pi \tag{A1}$$

$$\int_0^1 x\, dx \int_0^{2\pi} b(\varphi)\, d\varphi = 8/3 \tag{A2}$$

100

TABLE 1. Coefficients and Functions in Eq. (21)

i	a_i	f_i
1	-1	$\cos u/v^4$
2	$\alpha^2 l^2$	$u^2 \cos u/v^6$
3	$\alpha\delta$	$\sin u/v^4$
4	$-\alpha^3 l^2\delta$	$u^2 \sin u/v^6$
5	αl	$u \sin u/v^5$
6	$-\alpha^3 l^3$	$u^3 \sin u/v^7$
7	$\alpha^2 l\delta$	$u \cos u/v^5$

$$\int_0^1 x\,dx \int_0^{2\pi} b^2 \ln b\,d\varphi = \pi/4 \tag{A3}$$

$$\int_0^\infty \frac{\cos u\,du}{[(\alpha\rho b)^2 + u^2]^{3/2}} = K_1(\alpha\rho b)/\alpha\rho b = 1/\alpha^2\rho^2 b^2 - 1/4 + 1/2 \ln(\gamma\alpha\rho b/2) + O(\alpha^2\rho^2) \quad ([8], 8.432,5); \tag{A4}$$

$$\int_0^\infty \frac{\sin u\,du}{\sqrt{(\alpha\rho b)^2 + u^2}} = (\pi/2\alpha\rho b)[L_0'(\alpha\rho b) - I_1(\alpha\rho b)] = 1/\alpha\rho b - \pi/4 + O(\alpha\rho) \quad ([8], 3.754,1; 8.550,2); \tag{A5}$$

$$\int_{\pi-2\delta\alpha}^\infty \frac{\cos u\,du}{u^3} = -(2\delta/\pi^2 H) - 1/2\pi^2 + \mathrm{Ci}(\pi)/2 + O(\alpha^2\rho^2); \tag{A6}$$

$$\int_{\pi-2\delta\alpha}^\infty \frac{\sin u\,du}{u^3} = -1/2\pi + \mathrm{Si}(\pi)/2 + O(\alpha^2\rho^2); \tag{A7}$$

$$\mathrm{Si}(x) = \int_\infty^x \frac{\sin t}{t}\,dt; \quad \mathrm{Ci}(x) = \int_\infty^x \frac{\cos t}{t}\,dt \quad ([8], 8.230); \tag{A8}$$

$$\int_0^\infty \frac{\cos x\,dx}{(b^2 + x^2)^n} = \frac{\pi \exp(-b)}{(2b)^{2n-1}(n-1)!} \sum_{k=0}^{n-1} \frac{(2n-k-2)!(2b)^k}{k!(n-k-1)!}; \tag{A9}$$

$$\int_\pi^\infty \frac{\cos u}{u^4}\,du = 1/6\pi - 1/3\pi^3 - \mathrm{Si}(\pi)/6; \tag{A10}$$

$$\int_0^\infty f_3(u)\,du = -(1/2h)(\partial/\partial h)I, \quad I = \int_0^\infty \frac{\sin u\,du}{(h^2 + u^2)} = (1/2h)[\exp(-h)\,\mathrm{Ei}(h) - \exp(h)\,\mathrm{Ei}(-h)] \quad ([8], 3.723,1; 8.412,1,2); \tag{A11}$$

$$\int_0^\infty \frac{u \sin u\,du}{(h^2 + u^2)^{5/2}} = K_1(h)/3h = 1/3h^2 + O(1) \quad ([8], 3.773,3); \tag{A12}$$

$$h^3 \int_0^{\pi-2\delta\alpha} \frac{u \cos u\,du}{(h^2 + u^2)^{5/2}} = 1/3 + O(h^2). \tag{A13}$$

LITERATURE CITED

1. D. Behrens, Proc. Phys. Soc., 62A, 607 (1949).
2. N. I. Laletin, At. Energ., 7, 18 (1959).
3. B. Pershagen, in: Proc. Second Geneva Conf. [in Russian], Vol. 5, Akad. Nauk SSSR, Moscow (1958), p. 306.
4. J. Rowlands and C. Eaton, Nucl. Sci. Eng., 76, 263 (1980).
5. P. Benoist, J. Nucl. Energy, Part A, 13, 97 (1961).
6. I. S. Grigor'ev and V. M. Novikov, Neutron Diffusion in Heterogeneous Media [in Russian], Atomizdat, Moscow (1966).
7. B. P. Kochurov, Numerical Methods in the Theory of Heterogeneous Reactors [in Russian], Atomizdat, Moscow (1980).
8. I. S. Gradshtein and I. M. Ryzhik, Tables of Integrals, Series, and Products, Academic Press, New York (1965).

NEW RADIATION SAFETY STANDARDS FOR TRITIUM COMPOUNDS

M. I. Balonov, I. A. Likhtarev,
and Yu. I. Moskalev

UDC 539.16.08

The list of items containing tritium in common use in the USSR includes light-emitting materials, tritium—titanium static-charge neutralizers and air ionizers used in industry and agriculture in the Ukrainian SSR, tagged water in oilfields in Tataria, targets for accelerators and laser fusion systems, and tagged organic substances used in chemistry, biology, and medicine.

On the other hand, the Soviet regulations [1] and the international ones [2] contain standards only for two forms of tritium simple in composition and metabolism: oxide and gas. These standards are unsuitable for restricting the entry to the human body of tritium compounds having essentially different properties, particularly ones not soluble in the body or biologically active substances. Here we consider the radiation-safety standards for five classes of tritium compounds in common use. The calculation scheme is based on the concept of restricting the irradiation of critical organs [1].

Classification. Five classes of tritium compound may be distinguished on basic radiobiological features: the oxide, gaseous compounds, insoluble ones, soluble organic substances, and nucleic acid precursors. The oxide THO is a thermodynamically stable form of the nuclide that is most common in industrial and other conditions. The gaseous compounds such as T_2, CH_3T, etc. are dominated by elemental tritium TH, which has a low solubility in tissues. Compounds that are insoluble under physiological conditions include metallic tritides (TiT, ZrT, etc.), light-emitting materials (LEM) containing the nuclide incorporated into polymers, and glass microspheres saturated with tritium. The class of soluble organic tritium compounds consists of many hundreds of labeled substances, mainly biogenic ones, produced by the radiochemical industry. In view of the metabolic features, nucleic acid precursors labeled with tritium have been distinguished among these.

Quality Factor QF. The β radiation from tritium is of low energy (E_{max} = 18.6 keV, $\bar{E}$ = 5.7 keV), and it therefore differs from other β and γ radiations in producing elevated ionization density in tissue. The total linear energy transfer (LET) for tritium L_∞ is from 6 to 10 keV/μm for various methods of averaging the LET spectra [3]. The generally accepted relationship is QF = $(0.8 + 0.16 \cdot L_\infty)$, so $1.7 \leq$ QF ≤ 2.4 for tritium radiation.

During the past decade, QF = 1.7 has been used in the USSR to calculate the equivalent dose from tritium radiation [1], while the International Commission on Radiation Protection (ICRP) has recommended QF = 1. New experimental evidence has accumulated on the relative biological effectiveness of tritium oxide (RBE_{THO}), which is particularly applicable to radiation safety, i.e., obtained with mammals at doses of less than 100 rad (1 rad = 0.01 Gy) and/or from the remote carcinogenic and genetic effects (Table 1).

In the experiments by Dobson and also by Balonov and Kudritskaya, there was an appreciable increase in the RBE as the dose was reduced, which agrees with the Keller—Rossi dual-action theory. The values of the RBE in the table cluster around the rounded value of 2, which is in the middle of the range $1.7 \leq$ QF ≤ 2.4, and on this basis we assumed QF = 2 ber/rad for tritium radiation relative to γ radiation of low dose rate. This value of the QF is used subsequently in calculating the equivalent doses and standards.

Tritium Oxide. The calculation on the radiation dose to tissue from tritiated water is the basis for standardizing tritium, since THO is not only the commonest form of the nuclide but is also the final product from metabolism and isotope exchange for many compounds.

As THO resembles stable water, its metabolism is known in detail for man [4-7]. When THO enters the body through the lungs, mouth, or skin, it becomes uniformly distributed in the body water over 2-4 h. Also, 0.5-4% of the tritium atoms reversibly replace hydrogen

TABLE 1. Relative Biological Effectiveness of Tritium Oxide

Biological test	D_{THO}, rad	Standard radiation	RBE_{THO}, rel. units	Source
Damage to mouse spermatogonia	12	X, 200 kV	2,4	Lambert, 1969
Mammary tumors in female rats	150—600	γ, ^{137}Cs	1,8	Moskalev et al., 1973
Damage to mouse primary oocytes	10—40	γ, ^{60}Co	1,6—2,8	Dobson e. a., 1976
Atrophy in mouse	14—60	γ, ^{60}Co	1,7	Carr, Nolan, 1979
testicles	12—200	γ, ^{137}Cs	1,8—2,3	Balanov and Kudritskaya, 1983
Specific locus mutations in mouse spermatogonia	615	γ, ^{60}Co	2,2	Russel e. a., 1979
Dominant lethal mutations in mouse spermatocytes and spermatids	50—400	γ, ^{137}Cs	1,7—2,5	Balanov and Kudritskaya, 1983
Reciprocal translocations in mouse spermatogonia	100—400	γ, ^{137}Cs	1—2	Pomerantseva et al., 1983

in OH, NH, and SH groups in organic compounds. About 1% of the activity is gradually incorporated into stable CH bonds. The excretion of the THO with water is exponential with an average period T_1 = 10 days but with variations from 4 to 18 days. On prolonged observation of the tritium concentration in urine $W(t)$, there are second and third terms in the retention function with T_2 = 23–76 days and T_3 = 280–630 days and relative contributions W_2/W_1 = $4 \cdot 10^{-3}$; W_3/W_1 = $4 \cdot 10^{-5}$ [7].

The tissues most irradiated by tritium oxide are ones with high water contents, i.e., soft tissues apart from fat. The proportions of water in these tissues range from 70 to 80% [8]. If we take the tissue critical for THO irradiation as containing 80% water, we can derive the expected equivalent dose in soft tissues from the intake of 1 µCi of THO (1 Ci = 3.700×10^{10} Bq):

$$H_1 = 51.2 \frac{1 \cdot 0.8 \bar{E} \cdot QF}{M_B} \int_0^\infty \exp\left(-\frac{0.69}{T_1}t\right) dt = 1.6 \cdot 10^{-4} \text{ ber/µCi.} \tag{1}$$

where $\bar{E}$ = 0.0057 MeV, QF = 2 ber/rad (1 ber = 0.01 Sv), T_1 = 10 days, and M_B = 42×10^3 g is the mass of water in the body of a standard man [8].

The correction to the dose due to the bound tritium and to the second and third components in the THO retention is about 4% [7].

From (1) one can calculate the maximum permissible intake MPI of THO for those working with radiation: MPI = (5 ber/yr)/($1.6 \cdot 10^{-4}$ ber/µCi) = $3 \cdot 10^4$ µCi/yr. The permissible body burden BB_A is accumulated on the daily intake of $3 \cdot 10^4$/365 = 82 µCi/day and constitutes

82 $\int_0^\infty$ exp(–0.69/10)t)dt = $1.2 \cdot 10^3$ µCi. The THO concentration in the body water is then

28 µCi/liter. To calculate the permissible THO concentration in the air of working locations PC_A one should consider not only the inspiration of THO (2.5×10^6 liter/yr [1] but also the uptake through the Skin of $1-1.5 \times 10^6$ liter/yr (Osborn's data [5]). On this basis, PC_A = $3 \cdot 10^4 \cdot 10^{-6}/[(3.5-4) \cdot 10^6]$ $1 \cdot 10^{-8}$ Ci/liter. For individual members of the population, the maximum annual intake MAI = 0.1MPI; PC_B = $0.03 PC_A$. The standards thereby derived (Table 2), apart from BB_A, are 1.5-2 times those that currently apply [1] because of the use of revised physiological data.

TABLE 2. Standards for Tritium Compounds

Tritium compounds	Critical organ	Category A			Category B			
		BB_A, μCi	MPI through organs of respiration; $\mu Ci/yr$	PC_A, $Ci/liter$	MPI, $\mu Ci/yr$		PC_B, $Ci/liter$	
					through organs of respiration	through digestive tract	in atmospheric air	in water
Oxide (THO, TDO, T_2O)	Whole body	$1,2\cdot10^3$	$2\cdot10^1$ *	$1\cdot10^{-8}$	$2\cdot10^3$	$3\cdot10^3$	$3\cdot10^{-10}$	$4\cdot10^{-6}$
Gas (TH, TD, T_2)	Whole body	$1,4\cdot10^3$	$1,5\cdot10^8$	$6\cdot10^{-5}$	$1,5\cdot10^7$	—	$2\cdot10^{-6}$	—
Insoluble (Ti and Zr titrides, light-emitting materials etc.)	Lungs	70	$5\cdot10^2$	$2\cdot10^{-10}$	50	$3\cdot10^4$	$6\cdot10^{-12}$	$4\cdot10^{-5}$
Soluble organic	Whole body	$1,6\cdot10^3$	$1,5\cdot10^5$	$6\cdot10^{-8}$	$1,5\cdot10^3$	$1\cdot10^3$	$2\cdot10^{-10}$	$1\cdot10^{-6}$
Nucleic-acid precursors	Bone marrow, gonads	—	$3\cdot10^3$	$1\cdot10^{-9}$	$3\cdot10^2$	$7\cdot10^2$	$3\cdot10^{-11}$	$1\cdot10^{-6}$

*Simultaneously, half of this amount enters the body through the skin.
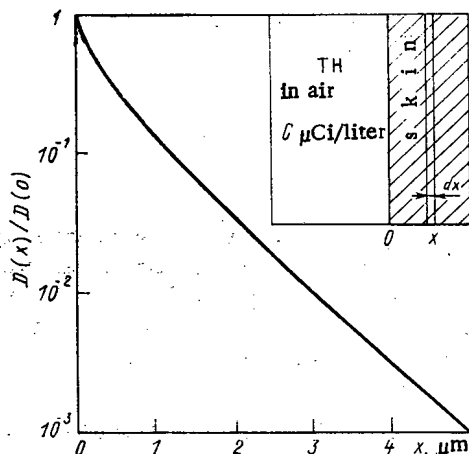
Fig. 1. Change in absorbed dose with distance x from boundary between source (air) and target (tissue) [7].

Gaseous Tritium. A person in a cloud of gaseous tritium undergoes contact irradiation in the lungs, skin, and upper respiratory tract, as well as the soft tissues arising from the nuclide dissolving or oxidizing in the body.

The alveoli are of size 0.1-0.5 mm, which is less than the range of the β particles in air, and at rest they contain V_L = 3 liters of air [8] with a tritium concentration C in $\mu Ci/liter$. The equivalent dose rate in the lung parenchyma is

$$h_L = 2.13 \frac{CV_L}{M_L} \overline{E} QF = 7.3 \cdot 10^{-5} C, \text{ ber/h}, \tag{2}$$

where M_L = 1000 g is the lung mass [8].

The dose from tritium in the upper layers of the skin and the respiratory pathways decreases rapidly with depth in the tissue (Fig. 1), so the β particles do not attain radiation-sensitive cells. The solubility of hydrogen in tissues is very low (2-10 vol.%), so the corresponding dose rate is not more than $2 \times 10^{-6} C$ ber/h in fatty tissue [7].

Pinson and Langham's data [4] indicate that 7×10^{-5} of the inspired TH is oxidized to THO in the human body at rest. The TH uptake by gut bacteria is variable [4], so it is desirable to introduce a safety factor of 3. Then on the basis of (1), TH in the atmosphere produces the following expected dose due to THO:

$$h_{THO} = 1500 \text{ liter/h } C \cdot 7 \cdot 10^{-5} \cdot 1,6 \cdot 10^{-4} \text{ ber/}\mu Ci \quad \cdot 3 = 5 \cdot 10^{-5} C, \text{ ber/h.} \tag{3}$$

We emphasize that here we do not consider the absorption of THO vapor, which is usually present in air along with TH.
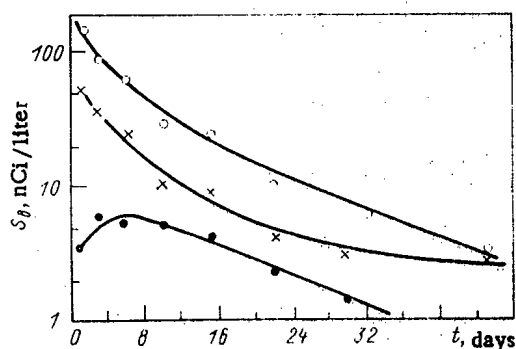
Fig. 2. Specific activity S_b of bound tritium in rat spleen after the injection of 1 μCi/g of THO (filled circle), ^{3}H-glucose (cross), and DL leucine-^{3}H (open circle)[7].

TABLE 3. Biological Effects of ^{3}H-Thymidine in Mice

Biological test	^{3}H-thymidine dose μCi/g	Standard radiation	D_1, rad·g / μCi	Source
Dominant lethal mutations in male gametes	7,5	X	20	Bateman, Chandley, 1962
	1—30	γ, ^{137}Cs	25	Balanov and Chetchueva, 1983
Carcinogenic effect, reduction in average lifespan	1—10	—	10—50	Baserga e. a., 1966
	1—5	γ, ^{60}Co		Johnson, Cronkite, 1967
	0,3—1,5	γ, ^{60}Co		Mewissen e. a., 1978
Damage to spermatogonia	1—40	X, 200 kV	6	Lambert, 1969
Fertility reduction in six generations	1	THO	20—40	Mewissen e. a., 1977
Lethal effect in 30 days	60—600	THO	4	Zhuravlev and Kalyazina, 1979
Testicle atrophy	1—20	γ, ^{60}Co	10	Carr, Nolan, 1979
	1—30	γ, ^{137}Cs	10	Balanov and Chetchueva, 1983
Reciprocal translocations in spermatogonia	1—30	γ, ^{137}Cs	10	Pomerantseva et al., 1983

To calculate PC_A, we equate the sum of (2) and (3) to the permissible dose rate PDR for irradiation of the lungs: 12×10^{-5} PC_A ber/h = 15 ber/1700 h, so $PC_A \approx 70$ μCi/liter. On the other hand, PC_A can be determined by comparing (3) with the PDR for the entire body, which gives PC_A = 60 μCi/liter. Table 2 gives the smaller value and values derived from it. The new standards exceed those applying in the USSR by factors of 30, since we have taken the critical organs as being soft tissues and lungs instead of skin irradiated from a half-space [1].

Insoluble Tritium Compounds. In vitro experiments and ones with animals have shown that when TiT or ZrT or a light-emitting material is in contact with an aqueous medium, 0.5-5% of the tritium activity passes into solution in the form of oxide [7, 9]. This fraction produces irradiation, which has been confirmed in tests on volunteers. Light-emitting materials also release simple organic tritium compounds, which are rapidly excreted and then produce doubled doses in the liver and kidneys [7].

105

Over 90% of the activity is retained indefinitely in the main carrier, which is decisive in the case of inhalation. Rats receiving TiT particles in normal respiration showed no tendency to excrete the tritium from the lungs over a month [7]. Data given by Bruk indicate that the tritium specific activity in the lungs of rats after the introduction of PS-A light-emitting powder was practically unchanged over 5 months. Both of these substances are reckoned as insoluble under physiological conditions and assigned to class D [2]. Similar properties occur in glass microspheres saturated with tritium as used in laser fusion research [10].

The ICRP model has been used for substances of solubility class D [2] to calculate the average tritium dose in human lungs from the inspiration of insoluble tritium compounds, the value being $H_1L \approx 0.03$ ber/μCi [7]. The doses in other tissues are lower by 3-4 orders of magnitude. If we compare H_1L with MPD = 15 ber/yr for the lungs, we get MPI = 500 μCi/yr for insoluble forms of tritium. This value and the derived standards (Table 2) are much more stringent than the standards for THO, and they contain a certain safety margin associated with the heterogeneous extracellular distribution of the nuclide in the lung tissue.

Soluble Organic Tritium Compounds. There are hundreds of biogenic tritium compounds produced and used in the USSR and in Comecon member nations. The standards (Table 2) are based on the properties of the most frequently used and/or radiotoxic substances and are extended to all compounds of this class, apart from nuclei-acid precursors. The compounds used in the largest amounts are tagged amino acids, glucose, and steroids. A general feature of the tritium metabolism for these substances is the stable binding that occurs in the synthesis of biopolymers, with the bound fraction of the nuclide retained for a long time (Fig. 2), which increases the tissue dose by comparison with the absorption of THO. Some of the tritium activity, perhaps a considerable fraction, is degraded to the oxide.

Studies have been made on the metabolism of over 20 tritium compounds in mammals. These include compounds such as folic acid, cholesterol, amino acids, L-lysine, and tyrosine, whose tritium is virtually completely taken up by animal tissues [7, 11, 12]. The absorbed dose in soft tissue is then 2-3 times higher than from the intake of THO.

Experiments on mice have shown that the genetic effects from ^{3}H-glycine and ^{3}H-glucose are similar to those from THO and are completely determined by the level of the dose absorbed in the sex cells [7]. For this reason, we have transferred the maximum ratio of the doses due to biogenic tritium compounds and THO (namely 3:1) to man: $H_{1max} \approx 5 \cdot 10^{-4}$ ber/μCi. Then MPI = 1×10^4 μCi/yr for oral administration. The permissible inhalation is larger by a factor 1.5 on account of incomplete particle retention in the organs of respiration.

Nucleic-Acid Precursors. The incorporation of these tritium-labeled substances is a special case of extremely inhomogeneous tissue irradiation: a ^{3}H-thymidine and other desoxyribose nucleosides are incorporated into the chromosomes of S-phase cells in radiosensitive tissues and subsequently selectively irradiate the nuclei. The concept of average tissue dose is inapplicable here. A scheme has been devised for calculating the doses in the nuclei of bone-marrow stem cells, which are responsible for radiation-induced leucosis [13]. An alternative approach is to compare the biological effects of ^{3}H-thymidine in mice with those of a standard radiation [7], which enables one to avoid numerous assumptions about the metabolism of the radiosensitive cell systems. The published information on the radiotoxicology of ^{3}H-thymidine (Table 3) shows that injection of mice with this substance at 1 μCi/g is comparable with the effect from a γ-ray dose D_1 = 10-30 rad. Then by extrapolation between species we get MPI = 2×10^3 μCi/yr for man on introduction into the circulation or 3×10^3 μCi/yr on inhalation. On account of the degradation of ^{3}H-thymidine in the gut, the limits for intake with food are higher by a factor 3.

Tritium Surface Contamination. As the range of the β particles is short, firmly attached surface contamination due to tritium does not represent a hazard and is not the subject of standardization and monitoring. Amongst unfixed contaminants, one may distinguish volatile molecular forms (sorbed TH and THO, or organic liquids) and nonvolatile particles. The skin-contact incorporation of volatile substances is of little significance by comparison with the aerial route. On the other hand, nonvolatile particles (light-emitting materials or microcrystals of tagged compounds) contaminate the skin directly, and the tritium thereby enters the blood. The secondary generation of aerosols by ventilating air flows is also important. The second path is the critical one for the most toxic forms of tritium, as for other radionuclides [14]. The permissible surface contamination density PS_A for nonvolatile tritium

106

compounds is calculated by analogy with [14] and is $PS_A = 10^{-8}$ Ci/cm². This value is higher by an order of magnitude than the values for other more toxic β emitters [1]. A calculation may be based on the irradiation of the body by the absorbed tritium and the local irradiation of the skin [7], which shows that 10^{-8} Ci/cm² is suitable also as a standard for skin contamination of those professionally exposed.

All these standards have been accepted by the National Commission on Radiation Protection and have been confirmed by the Ministry of Health Care of the USSR. To introduce them into use requires the development of adequate methodology and techanical facilities for differential monitoring of the various forms of tritium in the environment and the human body.

LITERATURE CITED

1. Radiation-Safety Standards NRB-76 [in Russian], Atomizdat, Moscow (1978).
2. Maximum Permissible Radionuclide Intakes for Those Working with Ionizing Radiation: ICRP Publication 30 [Russian translation], Énergoizdat, Moscow (1982).
3. V. I. Popov, LET Methods in Ionizing-Radiation Spectrometry [in Russian], Atomizdat, Moscow (1978).
4. E. Pinson and W. Langham, J. Appl. Physiol., 10, No. 1, 108 (1957).
5. Tritium Oxide [in Russian], Atomizdat, Moscow (1968).
6. M. Balonov, E. Dolgirev, and I. Likhtarev, Health Phys., 27, No. 4, 367 (1974).
7. M. I. Balonov, Tritium Dosimetry and Standardization [in Russian], Énergoatomizdat, Moscow (1983).
8. Man: Biomedical Data [in Russian], Meditsina, Moscow (1977).
9. J. Biro and I. Feher, in: Assessment of Air-Borne Radioactivity, IAEA, Vienna (1967), p. 501.
10. D. Cool and H. Maillie, Health Phys., 43, No. 1, 92 (1982).
11. J. Vennart, ibid., 16, No. 2, 429 (1979).
12. N. S. Kalyazina et al., Med. Radiol., 27, No. 8, 53 (1982).
13. L. Feinendegen and E. Cronkite, Current Top. Rad. Res. Quart., 12, 83 (1977).
14. Dosimetric and Radiometric Monitoring [in Russian], Vol. 1, Atomizdat, Moscow (1980).

RADIATION CAPACITY OF A RIVER CONTAINING LITTLE DRIFT
ON SHORT-TERM RADIONUCLIDE DISCHARGE

A. L. Kononovich

UDC 621.039.7.14

In nuclear power station operation, it is important to protect nearby surface water bodies, particularly rivers and streams, from contamination. At present, liquid radioactive wastes are not normally discharged to such waters. Considerable practical significance therefore attaches to the environmental effects of accidental and therefore brief radionuclide discharges.

In order to determine the doses to the population and also to the flora and fauna, it is necessary to have information on the radionuclide distribution. Here we calculate the pollutant distribution in bottom sediments in a river after a brief single discharge. The reciprocal of this is called the radiation capacity [1] and is used to calculate the limiting permissible nuclide discharge. In a short-time discharge, the radiation capacity is a function of time, in contrast to the stationary case, and has the dimensions of a volume.

Let there be an instantaneous discharge of radioactive material at the initial instant. The radionuclides in the dissolved state are rapidly carried away by the flow, and the brief action of these, which is usually slight, can readily be calculated. Insoluble radioactive particles deposit on the bottom and produce long-term contamination. The following model is used to calculate this:

107

1. Two contamination phases are considered: suspended particles carried off in the mass of the water and bottom sediments consisting of particles at rest on the bottom.

2. There is exchange between the phases, with the entry of the radionuclides into the suspended phase proportional to the bottom pollution, while the entry of radionuclides into the sediments is proportional to the concentration of suspended radioactive particles in the bottom layer of water. The mass-exchange conditions are constant throughout the river and do not vary with time.

3. Transverse migration of the suspended particles is assumed to be independent of transport in the longitudinal direction.

4. The rivers do not have persistent recirculation regions.

5. The time required to set up a stationary depth distribution is determined by the mass transfer between horizontal layers and is small by comparison with the equilibrium time for the sediments and suspended phase.

6. Reduction in the concentration due to decay is neglected.

The last point means that the suspended-particle concentration in the bottom layer is proportional to the concentration averaged over the vertical, i.e., the treatment can be two-dimensional. We choose a coordinate system in which the x axis is directed along the flow and the origin lies at the point of discharge.

It follows from condition 3 that the contamination distribution within the bed can be represented as the product of two independent functions, the first describing the longitudinal transport and the exchange between the phases and being dependent only on the x coordinate and time, while the second is a correction one and characterizes the transverse turbulent diffusion and the dilution due to the influx of pure water (groundwater and tributories). Here we consider the first of these factors.

The above model gives us the following formulation:

$$\frac{\partial q}{\partial t} = -v \frac{\partial q}{\partial x} - \alpha q + \beta \rho;$$

$$\frac{\partial \rho}{\partial t} = \alpha q - \beta \rho.$$

(1)

Here q is the concentration of suspended radioactive particles averaged over the vertical; ρ, radionuclide concentration in bottom sediments; v, flow speed; and α and β, kinetic constants that describe the mass transfer between phases. The values are dependent on the hydraulic particle size and on the flow speed.

The initial and boundary conditions at the instant of the primary discharge are described by

$$q(x, 0) = 0;$$
$$q(0, t) = Q_0 \delta(t);$$
$$\rho(x, 0) = 0;$$
$$\rho(0, t) = \frac{\alpha}{\beta} q_0 \delta(t),$$

(2)

where Q_0 is the amount of material discharged.

At this stage, we can neglect the secondary contamination of the water by the sediments, since the particle concentration in the water at that time is substantially above the equilibrium value. We then get that the particle distribution at the bottom is described by the following when the primary contaminated water has passed:

$$\rho_{st}(x) = \frac{Q_0 \alpha}{v} e^{-(\alpha/v)x}.$$

We note that the passage time for the primary pulse is small by comparison with the time scales of the following processes. Subsequently, the boundary and initial conditions can be put as follows:
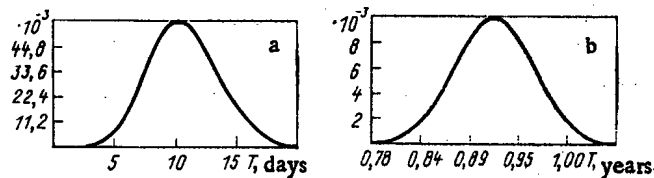
108

Fig. 1. Specific activity C of sediments in relation to time T at distances of 5 km (a) and 160 km (b) from the discharge point. The concentrations in the sediments are expressed as fractions of the contamination at the point of discharge at the initial instant.

$$\rho(x, 0) = \rho_{sl}(x);$$
$$\rho(0, t) = \frac{Q_0 \alpha}{v} e^{-\beta t}; \tag{3}$$
$$\frac{\partial \rho(x, 0)}{\partial t} = -\beta \rho_{sl}(x).$$

The solution is bounded at infinity.

The solution to (1) with the boundary conditions of (3) was derived by operational methods. The result is not given here because it is cumbersome. We used an asymptotic expansion in powers of $1/\sqrt{t}$ for practical calculations:

$$\rho(\psi, \tau) = \frac{\alpha Q_0 e^{-\left(\frac{\psi}{2\gamma} + 2\gamma(\tau - \psi)\right)}}{2v \sqrt{\gamma^2 + 1}} \sum (A^{n+1} - (-B^{n+1}) \left(\sqrt{\frac{\psi}{\tau - \psi}}\right)^n I_n (2\sqrt{\psi(\tau - \psi)}). \tag{4}$$

Here the dimensionless variables are

$$\psi = \frac{\sqrt{\alpha\beta}}{v} x;$$
$$\tau = \sqrt{\alpha\beta}\, t;$$
$$\gamma = \frac{1}{2} \sqrt{\frac{\beta}{\alpha}};$$
$$A = \sqrt{\gamma^2 + 1} - \gamma;$$
$$B = \sqrt{\gamma^2 + 1} + \gamma;$$

and $I_n(r)$ is the modified Bessel function of order n.

The graph for (4) is a curve with one maximum, which gradually moves along the flow direction. The following expression defines the speed of the maximum at large values of the argument $\left(4\sqrt{\psi(\tau - \psi)} = 4\sqrt{\frac{\alpha\beta xt}{v}} \gg 1\right)$

$$w = \frac{\beta}{\alpha + \beta} v.$$

The maximum value at large distances is

$$\rho_{max} = \frac{\alpha Q_v}{v \sqrt{4\pi} \sqrt{\psi_m (\tau_m - \psi_m)}} = \frac{Q_0 \sqrt{\alpha}}{\sqrt{4\pi v x}}, \tag{5}$$

where x is the observation coordinate.

To calculate the radiation capacity, we need to know α and β, but at present experimental data are lacking. Therefore, the values of α and β were determined by an indirect method based on results on river hydraulics. System (1) can be reduced to familiar models for river drifts on the basis that the density of the bottom sediments changes very slowly during deposition or erosion if the material is homogeneous. In that case, the second equation becomes unnecessary, while the first becomes a particular case in several models [2-6] if one assumes that

109

$$\frac{\beta}{\alpha}\rho_s = P_s h,$$

where ρ_s is the density of the bottom soil; P_s, turbidity averaged over the vertical, corresponding to the carrying capacity of the flow; and h, river depth.

The value of α can be determined by comparing the solution to the first equation in (1) with Karaushev's model [2]:

$$\alpha = \frac{u\Gamma}{(1-\Gamma)hv},$$

where u is the hydraulic particle size and Γ is the hydromechanical parameter.

We calculated the function of (4) for the particle fraction of size 0.03 mm with ρ_s = 1.5 tons/m^3, particle density 2.3 tons/m^3, h = 2 m, and v = 0.4 m/sec. This gave α = 2 $\times$ 10^{-3} sec^{-1} and β = 1 $\times$ 10^{-5} sec^{-1}. These values are only approximate, since the models for drift transport are conflicting [5]. Figure 1 gives results normalized to the specific activity of the bottom sediments at the initial instant at the origin.

To calculate the radiation capacity of a particular river, it is necessary to consider the dilution due to the influx of clean water and the mixing. The final expression for the radiation capacity at large distances from the discharge point is

$$R_b(x, t) = \frac{\varkappa(x)\omega}{\rho(x, t)},$$

where $\varkappa(x)$ is the ratio of the flow rate at a remote point at distance x to the flow rate at the discharge point, $\rho(x, t)$ is the function calculated from (4) with Q_0 = 1, and ω is the active cross section of the river at the discharge point. The point x is chosen on the basis of the economic use of the river.

To apply these results, it must be borne in mind that the values forecast from this model for distances of some tens of kilometers are approximate: the error may attain 1.5-2 orders of magnitude if one uses the values calculated for α and β, because our knowledge of suspension and sedimentation for insoluble particles is inadequate. The various models diverge in their estimates of the carrying capacity by more than an order of magnitude (p. 205 of [5]), and therefore one should use values of α and β for practical purposes that have been determined by observation on a particular river during the first few days. Then the forecast values for a river with little sediment at distances of ~100–200 km from the discharge point will differ from the observed ones by only factors of 2-3.

The main result here is the conclusion that the maximum contamination of the sediment as a function of distance does not vary exponentially, as has been assumed in many calculations, but is inversely proportional to the square root of the distance. Therefore, a contaminated zone may be found at considerable distances from the discharge point. This feature should be borne in mind in organizing radiometric monitoring.

<div align="center">LITERATURE CITED</div>

1. A. L. Kononovich et al., At. Energ., 50, No. 1, 50 (1981).
2. A. V. Karaushev, River Drifts: Theory and Calculation Methods [in Russian], Gidrometizdat, Leningrad (1977).
3. I. I. Levi, River-Flow Dynamics [in Russian], Gosénergoizdat, Moscow (1957).
4. V. N. Goncharov, River-Flow Dynamics [in Russian], Gidrometizdat, Leningrad (1962).
5. A. B. Veksler and V. M. Donenberg, River-Bed Modification below the Discharges from Large Hydroelectric Stations [in Russian], Énergoizdat, Moscow (1983).
6. A. V. Gagen, in: Papers on Hydraulic Engineering [in Russian], Issue 12, Énergoizdat, Moscow (1972), p. 44.

LETTERS TO THE EDITOR

DIAMOND DOSIMETER OF PULSED GAMMA RAYS

Z. A. Al'bikov and N. I. Terent'ev   UDC 539.12.08

In measurements of photon radiation with a quantum energy of no more than 10 MeV, the kinetic energy released (kerma) in air can be considered as the energy equivalent of the exposure dose since the fraction of the energy expended by secondary electrons on bremsstrahlung does not exceed a few percent [1, 2]. Measurement of the exposure dose (and the dose rate) of pulsed fields of photon radiation poses considerable difficulties when the pulse duration is on the order of 10^{-9} sec or less, the dose rate is greater than 10^6 C/kg·sec, and the energy is higher than 3 MeV. The principal difficulties encountered in carrying out these measurements are due to the lack of dosimeters attested for these ranges of intensity, duration, and energy. In our view, for such measurements one could recommend a high-speed air-equivalent dosimeter, constituting a solid-state analog of a wall ionization chamber, which has a sensitive diamond element [3]. For the given energy range with a proper choice of thickness of tissue-equivalent materials surrounding the sensitive element electronic equilibrium is established in it and the energy absorbed in the sensitive element is, in an approximation sufficient for measurements (except for small bremsstrahlung losses), equal to the kinetic energy released in the air at the site of installation of the dosimeter. Such dosimeters have been designed, fabricated, and used to measure dose fields in some bremsstrahlung sources.

For pulsed measurements the following dosimeter characteristics are the most important: the dose sensitivity and the error with which it is determined, the pulsed characteristic and the time resolution, the energy dependence of the dose sensitivity (EDS), the amplitude characteristic, and the radiation resistance. The procedure for determining the sensitivity of diamond dosimeters to static radiation on a UPGD-2 standard apparatus as well as the method of determining the time resolution and the results thus obtained have been discussed in [4].

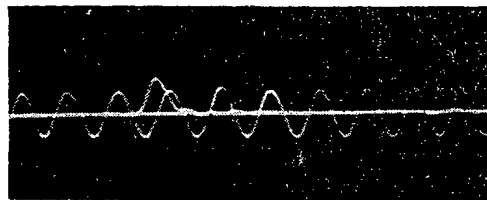Fig. 1. Oscillogram of a pulse from a diamond dosimeter under the action of a short bremsstrahlung pulse. The frequency of the sine-wave marker is 833 MHz.

TABLE 1. Characteristics of Diamond Dosimeters

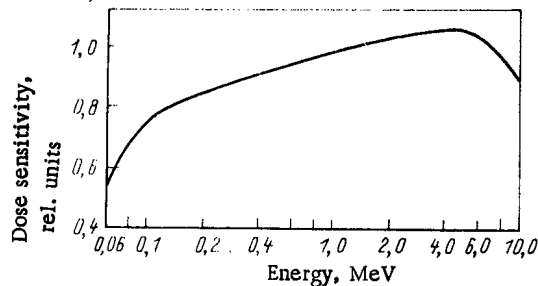| No. of dosimeter	Dose sensitivity, kg	Time resolution, nsec
K-4	$3,1 \cdot 10^{-7}$	0,4
1-3	$9,4 \cdot 10^{-7}$	0,4
V-8	$4,7 \cdot 10^{-6}$	1,2
IV-8	$2,5 \cdot 10^{-5}$	1,4

111

Fig. 2. Energy dependence of the sensitivity of a diamond dosimeter.

TABLE 2. Comparison of the Readings of Diamond and Thermoluminescent Dosimeters (TLD)

Max. dose rate measured by a diamond dosimeter, C/kg·sec	Dose in a pulse, C/kg	
	diamond dosimeters,	TLD
$2,2 \cdot 10^5$	$3,4 \cdot 10^{-2}$	$3,9 \cdot 10^{-2}$
$2,8 \cdot 10^5$	$7,5 \cdot 10^{-3}$	$7,2 \cdot 10^{-3}$
$3,4 \cdot 10^5$	$8,8 \cdot 10^{-3}$	$7,0 \cdot 10^{-3}$
$7,7 \cdot 10^5$	$1,1 \cdot 10^{-1}$	$1,4 \cdot 10^{-1}$
$3,1 \cdot 10^5$	$3,6 \cdot 10^{-2}$	$2,8 \cdot 10^{-2}$
$4,1 \cdot 10^6$	$6,2 \cdot 10^{-2}$	$5,2 \cdot 10^{-2}$

The dose sensitivity of dosimeters is determined from the measured current—voltage characteristic (I—V curve); in the given case this is called the dependence of the sensitivity on the supply voltage. For dosimeters operating with total carrier collection the I—V curves are practically independent of the supply voltage and in this case, within the limits of measuring error, the sensitivity of the dosimeters corresponds to the design value; in dosimeters operating with incomplete carrier collection the I—V curve has a slope and the sensitivity is less than that calculated for total collection. Table 1 gives the values of the sensitivity of some dosimeters at an operating voltage of 700 V. The error in the determination of the sensitivity does not exceed ±13% at a confidence coefficient P = 0.95.

The time resolution, defined as the full-width at half-maximum of the pulsed characteristic, depends on the sensitivity of the dosimeters (see Table 1). The oscillogram of a pulse from dosimeter K-4, which was obtained during investigation of the time resolution on an apparatus generating a bremsstrahlung pulse with a full-width at half-maximum of (0.34 ± 0.1) nsec, is given in Fig. 1.

It was experimentally established that diamond dosimeters are linear in the dose-rate range from $3 \cdot 10^{-7}$ (during calibration) to $3 \cdot 10^6$ C/kg·sec (in pulsed measurements). The maximum values of the linear current are 1-6 A, depending on the dosimeter. The calculated energy dependence of the sensitivity of a diamond dosimeter with a graphite substrate 10 mm thick is given in Fig. 2. It is seen that at an energy of 0.2-10 MeV the deviation of the energy dependence of the dose sensitivity does not exceed ±15% of the sensitivity to 1.25-MeV radiation. This dependence was verified experimentally with ^{60}Co and ^{137}Cs sources and bremsstrahlung with a limiting energy varying in the range 4-25 MeV. Within the limits of measuring error (±15%) the experimental data coincided with the calculated data. Table 2 compares the readings of diamond and integrated thermoluminescent dosimeters for several high-intensity pulses. The results of the measurements indicate that the readings of the dosimeters coincide to within 20-30%. The radiation resistance of diamond dosimeters is estimated at no less than 10^9 rd (1 rd = 0.01 Gy) [5].

112

The characteristics presented here show that a diamond dosimeter, which is suitable for measurements of steady-state radiations in units of exposure dose, makes it possible to make measurements to within ±20% of the kerma rate and the kerma in air by pulsed photon radiations over a wide range of dose rates (10^{-6}–10^7 C/kg·sec), pulse duration (up to 10^{-9} sec), and energy (up to 10 MeV).

In conclusion, we should point out that in dosimetric measurements on pulsed sources more reliable results, in our opinion, are obtained by recording the shape of the radiation pulse over time with subsequent integration than are obtained in integrated measurements in which it is necessary to substantiate the linear dependence of the measured dose on the radiation dose rate.

LITERATURE CITED

1. V. I. Ivanov, Course of Dosimetry [in Russian], Atomizdat, Moscow (1979), p. 36.
2. Radiation Safety. Quantities, Units, Methods, and Instruments. IAEA Reports 19 and 20 [in Russian], Atomizdat, Moscow (1974), p. 36.
3. Z. A. Al'bikov et al., Inventor's Certificate No. 701290, Byull. Izobret., No. 37, 321 (1980).
4. Z. A. Al'bikov et al., in: Problems of Physics and Technology of Wide-Gap Semiconductors [in Russian], Leningrad (1979), p. 250.
5. "Radiation detectors," Prib. Nauchn. Issled., No. 7, 142 (1975).

ERROR OF THE REICH–MOORE FORMULA FOR NEUTRON CROSS SECTIONS

I. I. Surina

UDC 539.125.5.162.3

The values of the neutron cross sections $\sigma^{(f)}(E)$ are given by the exact formulas of the Wigner–Aizenbud R-matrix theory [1]. For the cross section for fission with one fission and one radiation channel extensive use is made of the Reich–Moore approximation [2] which
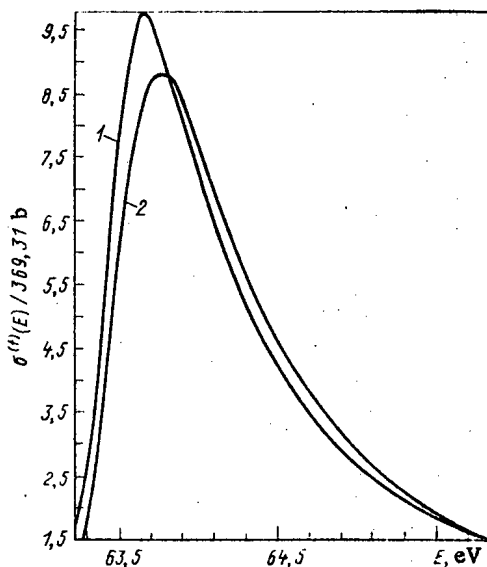

Fig. 1. Fission cross section for ^{235}U near one level (E_λ= 57.821–65.79 eV: spin of level J = 4) from exact formulas [1] and from the Reich–Moore formula [1].

113

determines $\sigma^{(f)}(E)$ with some error. We give the result of numerical investigation of this error.

For the ^{235}U fission cross section the values calculated from the exact formulas and from the Reich—Moore formula, with the same level parameters, are compared. The range of neutron energies over which the error was investigated was 5-100 eV. The relative errors were calculated at all points with respect to the energy E. Figure 1 shows a characteristic portion of the cross section in the proximity of one level. The conclusions about the properties of the error are as follows:

1. At the points $E = E_\lambda$ the error is low, about 1%.

2. At points close to E_λ the error can reach 25%. The displacement of the positions of the levels is 0.05 eV.

3. In the regions between levels the error can exceed 300%.

4. With an increase in the number of levels, the interference between which is taken into account, the error of the Reich—Moore formula increases.

5. The error of the resonance integrals is small, no greater than 0.2%.

Thus, the use of the Reich—Moore formula leads to large errors in the cross sections and the displacement of the positions of the levels, although it does permit the computation time to be reduced substantially. Upon calculating the cross sections for reactors, whose parameters are estimated in the Reich—Moore approximation, their use in exact formulas leads to the errors determined numerically here. The results presented here were obtained after the development of a method of calculating cross sections from the exact formulas of the R-matrix theory.

The authors are grateful to V. I. Mostov and A. P. Petrov for valuable discussions and to G. N. Antonova for assistance in carrying out the calculations on a computer.

LITERATURE CITED

1. D. Adler and F. Adler, Phys. Rev., 6, No. 3, 986 (1972).
2. C. Reich and M. Moore, Phys. Rev., 111, No. 3, 929 (1958).

APPLICATION OF GAS-CONTROLLED HEAT PIPES IN NUCLEAR TECHNOLOGY

I. G. Gverdtsiteli, A. G. Kalandarishvili,
V. A. Kuchukhidze, and P. D. Chilingarishvili

Heat pipes are currently used in nuclear technology primarily for cooling nuclear and isotopic reactors [1]. Heat pipes with variable thermal conductivity, so-called gas-controlled heat pipes (GCHP), are used in technology for thermal stabilization of different objects [2].

In this paper we examine the possibility of using GCHP for obtaining vapors of alkali metals, for controlling burn-up of nuclear fuel, and as a neutron flux integrator.

Use of GCHP for Obtaining Vapors of Alkali Metals. In [3] a setup was proposed for obtaining cesium vapor with the help of a heat pipe for controlling the parameters of thermal-emission energy converters. The most promising is a cesium source based on GCHP. The fundamental possibility of creating such a source was demonstrated in [4]. A peculiarity of its construction is the vapor-discharge pipe, which connects the volume of the adiabatic zone of the GCHP to the working volume of the thermal-emission energy converters.

Figure 1a shows a design in which the vapor-discharge pipe is constructed in the form of a pilot tube and is directed along the motion of the vapor flow of heat carrier. The pressure of the alkali metal vapor is measured with the help of an electrical discharge pressure sensor at the outlet of the vapor-discharge pipe.

The basic characteristic of the source — the dependence of the vapor pressure of the alkali metal (cesium) p_{Cs} at the outlet of the vapor-discharge pipe on the pressure of the noncondensing gas (NCG) in the gas reservoir of GCHP — is shown in Fig. 2. The dependence $p_{Cs} = \bar{f}(p_{NCG})$ was experimentally obtained for different values of the thermal power Q_e, injected into the evaporation zone of GCHP.

Two different sections are observed in these graphs. In the region of low pressure of NCG the cesium pressure is practically independent of p_{NCG}. At higher pressures the dependence is linear and conforms to the equation $p_{Cs} = p_{NCG}$.

These regularities are explained by taking into account the acoustic limitations of the power transmitted by the heat pipe. As is well known, the change in the NCG pressure in the reservoir propagates along the heat pipe with the velocity of sound. For this reason, when the vapor flow of heat carrier reaches the acoustic limit the change in pressure in the gas reservoir does not reach the location of the vapor-discharge pipe, and therefore, the vapor pressure does not depend on p_{NCG}. The deviation of the curve with $Q_e = 30$ W in Fig. 2 below the line $p_{Cs} = p_{NCG}$ is related with the low intensity of the heat input to the evaporator of the GCHP, as a result of which the vapor-gas interface drops below the vapor-discharge pipe and the noncondensing gas enters the volume of the electrical discharge pressure sensor.

It was shown in the experiments that sources of alkali metal vapors based on GCHP have the following basic advantages over other analogous sources:

1. Variation of the heat power introduced into the evaporation zone over a wide range (1:5) does not affect the alkali metal vapor pressure.

2. The vapor pressure of the alkali metal is controlled by a noninertial method by changing the NCG pressure in the gas reservoir of the GCHP.

3. A change in the temperature of the isothermal zone of the GCHP is caused by a change in the NCG pressure in the gas reservoir in accordance with the vapor pressure curve of the alkali metal used as the heat carrier.

Together with thermal-emission energy converters, different variants of cesium vapor sources were tested and their long-term operational lifetime was demonstrated.
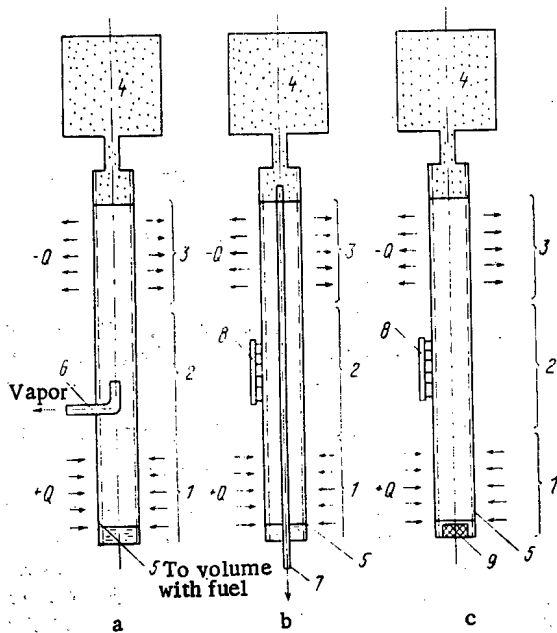
Fig. 1   Fig. 2

Fig. 1. Diagram of setups based on a gas-controlled heat pipe for obtaining vapors of alkali metals (a), for controlling burn-up of nuclear fuel (b), and as a neutron flux integrator (c): 1) evaporation zone; 2) isothermal zone; 3) condensation zone; 4) noncondensing gas; 5) wick; 6) vapor-discharge pipe; 7) gas supply pipe; 8) temperature sensor; 9) neutron absorber.
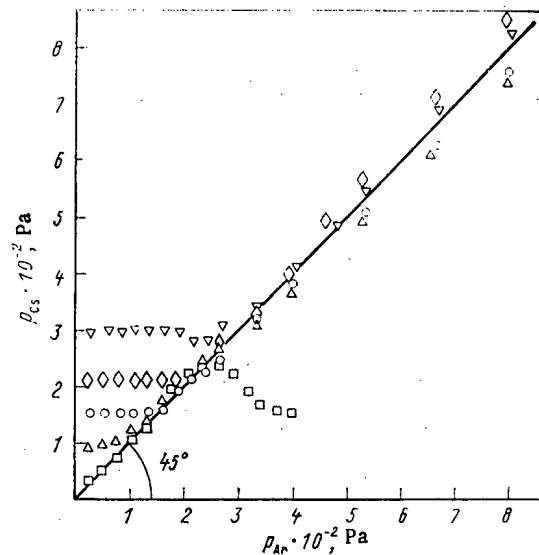
Fig. 2. Dependence of the cesium vapor pressure at the outlet of the vapor-discharge pipe on the noncondensing gas in GCHP for a thermal power Q_e introduced into the evaporator equal to 30 ($\square$); 56 ($\triangle$); 68 ($\bigcirc$); 96 ($\Diamond$) and 126 W (∇).

Use of GCHP for Continuous Control of the Degree of Burnup of Nuclear Fuel and as a Neutron Flux Integrator. The possibility of determining the degree of burnup of nuclear fuel by nondestructive methods by means of accumulation and quantitative measurement of the total effect of burnup monitors (γ activity, thermal effects, etc.) is examined in [5]. The measurement of the burnup of nuclear fuel by these methods involves the undesirable necessity of extracting spent fuel elements from the reactor. The possibility of estimating the degree of burnup of the nuclear fuel in fuel elements during the course of reactor operation according to the accumulation and quantitative measurement (pressure) of gaseous fission products (GFP) in GCHP is examined below.

The conditions of operation of measuring instruments in the active zone of the nuclear power reactors do not permit placing pressure sensors directly adjacent to the points at which measurements are made within the active zone [6]. Figure 1b shows a diagram of a possible design for monitoring the degree of burnup of nuclear fuel. The CG volume of the heat pipe is connected by means of the gas input pipe 7 to the volume of the fuel element. The pressure of the gaseous fission products, which by diffusing into the fuel enter through the pipe into the gaseous reservoir of the heat pipe and create a pressure change in it by an amount Δp, increases in proportion to the burnup of nuclear fuel [7]. Because p = PNCG, this changes the vapor pressure of the heat carrier by the same amount. According to the dependence p = φ (T), the change in the vapor pressure of the heat carrier affects the temperature in the isothermal zone of the heat pipe. Thus the temperature of the isothermal zone of the GCHP can be a measure of the degree of burnup of the nuclear fuel.

The pressure of the GFP in the fuel element is proportional to the fluence of thermal neutrons. Therefore, it is possible to determine the fluence of thermal neutrons by measuring the pressure of the GFP. It is also possible to make an integrator of thermal neutron

116

flux based on GCHP. The structural design is shown in Fig. 1c. A fissioning material 9, whose daughter nuclei are stable or metastable GFP, is placed in the evaporation zone 1. The GFP carried away by the flow of heat carrier enter the reservoir 4. This changes the temperature of the adiabatic zone of the heat pipe.

Using the equation of state of an ideal gas and the expression for determining the amount of liberated stable GFP [8], it is possible to obtain the dependence of the fluence F on the GFP pressure p_{NCG} in the gas reservoir:

$$F = \frac{p_{NCG} V_{NCG}}{Y V_f [x] k T_{NCG} E \sigma_f},$$

where V_{NCG} is the volume of the gas reservoir, cm^3; Y, relative output of stable gaseous products per act of fission; V_f, volume occupied by the fissioning material, cm^3; [x], concentration of fissioning material, atom·cm^{-3}; σ_f, fission cross section of the fissioning material, cm^{-2}; k, Boltzmann's constant, J·K^{-1}; T_{NCG}, temperature of GFP in the gas reservoir, equal to the temperature of the heat carrier in the reactor setup, °K; E, relative fraction of GEP liberated from the fissioning material. The value of p_{NCG}, entering into the equation presented above, is easily determined from the value of the temperature of the adiabatic zone of the GCHP.

As follows from the dependence obtained, the sensitivity of the thermal neutron flux integrator can be optimized to an acceptable accuracy by increasing the concentration (enrichment) and volume of the fissioning material. Thus, having placed the sensitive element of the neutron integrator (GCHP evaporator with a neutron absorber) into the active zone of the reactor, the fluence of thermal neutrons can be measured by measuring the temperature of the isothermal part of the GCHP.

LITERATURE CITED

1. S. Chi, Heat Pipes. Theory and Practice [in Russian], Mashinostroenie, Moscow (1981).
2. M. N. Ivanovskii et al., Technological Foundations of Heat Pipes [in Russian], Atomizdat, Moscow (1980).
3. P. I. Bystrov et al., At. Energ., 49, No. 4, 219 (1980).
4. I. G. Gverdtsiteli, A. G. Kalandarishvili, and P. D. Chilingarishvili, Zh. Tekh. Fiz., 49, 1764 (1979).
5. H. Ramthun, in: Proc. of the 2nd ASTM—EURATOM Symp. on Reactor Dosimetry, Dosimetry Methods for Fuels, Cladding and Structural Materials, 3-7 Oct. 1977, Palo Alto, California (1977), Vol. 1, p. 433.
6. N. A. Trofimov and V. V. Laplo, Measurement of the Parameters of Thermophysical Processes in Nuclear Energetics [in Russian], Atomizdat, Moscow (1979).
7. B. V. Samsonov et al., At. Energ., 40, No. 3, 390 (1976).
8. B. Lastman, Radiation Phenomena in Uranium Dioxide [in Russian], Atomizdat, Moscow (1964).

REACTOR TESTS OF A NEUTRON-FLUX REGULATION SYSTEM BASED ON

LAYERED COMPOUNDS OF PYROLYTIC GRAPHITE WITH CESIUM

I. G. Gverdtsiteli, Yu. A. Bunchin,
A. G. Kalandarishvili, M. N. Korotenko,
Yu. N. Krasik, S. D. Krivonosov,
B. A. Mskhalaya, and A. V. Nikonov

UDC 621.039.515

This paper is concerned with the results of an experimental check of the absorption method of regulating the neutron flux density with the help of layered structures, the basis for which is given in [1]. Experimental investigations performed with the use of activated carbon—cadmium [2] and activated carbon—boron trifluoride [3] have confirmed the effectiveness of the absorption method, based on absorption of substances by the surface of solids. In contrast to previously studied pairs, the absorbing screen in the case of layered structures is formed with absorption and penetration of neutron absorbing substances into the bulk of the structure of a neutron-transparent matrix, for example cesium in pyrolytic graphite. In view of the fact that the use of different neutron absorbing substances greatly affects the neutron spectrum due to the different spectral dependence of the absorption cross section of sorbates, as well as the temperature regime of operation of the sorption screen, it is necessary to perform thermal and reactor investigations of different sorption pairs in order to select the optimum composition for each specific problem.

We investigated an ampul with the absorbing screen made of pyrolytic graphite and cesium in a cell of the beryllium reflector of a VVR-M reactor at the Institute of Nuclear Research of the Academy of Sciences of the Ukrainian SSR.

The ampul is constructed in the form of two cylindrical cavities, placed in a housing 8 and connected by a pipe 4 (Fig. 1). A collection of rings made of pyrolytic graphite 6 with the crystallographic axis c oriented parallel to the generatrix is placed in the cavity 9. The cavity 2 serves as a source of cesium vapor. We used the central tube 1 to place the sensors of the neutron flux density beyond the absorption screen. The attenuation of the neutron flux depends on the specific content of absorbate in the absorbent, which, in its turn, is due to the temperature of graphite and cesium. In order to form a given temperature field, electrical heaters were placed on the neutron flux density regulator 9, the cesium feed 2, and the connecting pipe 4. We monitored the temperature with the help of chromel—alumel thermocouples. We measured the cesium temperature with a thermocouple fastened by contact welding in the pipe 3 (diameter 6 mm), which was washed on all sides by liquid cesium. To measure the graphite temperature, we used thermocouples built into the thin copper inserts 7, placed between the graphite rings. The leads to the thermocouples were output from the cesium volume through the hermetically sealed input leads 5. This positioning of thermocouples permitted measuring directly the temperature of the graphite and of the cesium and following the kinetics of the phase composition of the layered compound [4].

We measured the density of the neutron flux beyond the screen with the help of two DPZ-1p direct charge detectors, triplets (Cu, Au, Lu) of precalibrated activation detectors, as well as copper wire with a diameter of 0.11 mm. Irradiation of the copper wire permitted obtaining more complete data on the profile of the neutron flux along the height of the ampul. DPZ-1p detectors, one of which was placed in the housing 8 (see Fig. 1) and the other was placed in the active zone of the reactor adjacent to the experimental cell, served as monitors of the unperturbed neutron flux density. During the experiment we measured the thermal neutron flux density beyond the screen with different concentration of cesium in the graphite. The results of activation measurements are presented in Fig. 2.

The pyrographite is saturated with cesium only along the crystallographic axis c, i.e., vertically over the collection of pyrolytic graphite rings. The maximum height of the layered
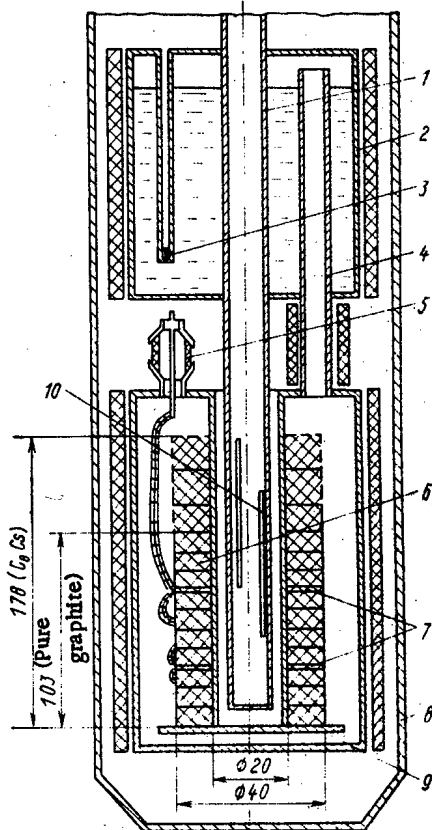
Fig. 1. Diagram of the experimental ampul for regulating
the neutron flux based on a layered compound of pyrolytic
graphite with cesium (all dimensions are shown in mm).
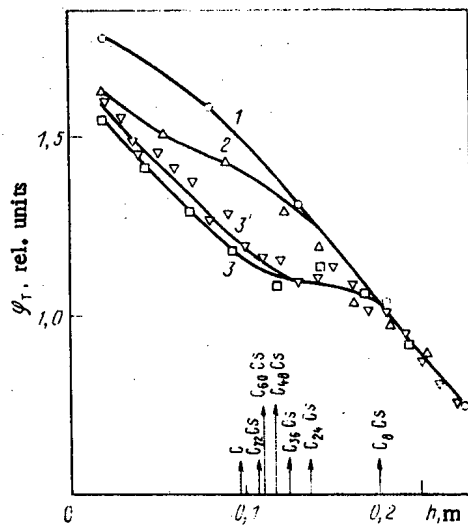
Fig. 2   Fig. 3

Fig. 2. Profiles of the thermal neutron flux density over the height of the
experimental ampul without an absorber (1) and with an absorber with phase
composition of layered compound $C_{36}Cs + C_{24}Cs$ (2) and $C_{12}Cs + C_8Cs$ (3, 3').

Fig. 3. Degree of attenuation of the flux density of thermal neutrons over
the height of the ampul with different phase compositions of the layered
compound: 1) pure graphite; 2) $C_{36}Cs + C_{24}Cs$; 3) $C_{23}Cs + C_8Cs$; — - —) data
in [1].

119

compound for all stable phases is marked by the arrows on the abscissa axis in Fig. 2. Curve 1 corresponds to a relative distribution of thermal neutron flux density in the upper half of the active zone without the absorber and curve 2 corresponds to a phase composition of the layered compound obtained with technological assembly of the ampul during recondensation of cesium from a bench still in the feeder. According to the measured temperature changes of the graphite and cesium, curve 3 corresponds to the maximum saturation by cesium of the pyrolytic graphite obtained during the investigation, i.e., to the phases $C_{12}Cs + C_8Cs$.

The relative distribution of the flux density of thermal neutrons (see Fig. 2, curve 3)) was obtained based on a calculation by the method of smoothing the induced activity of the copper wire, irradiated together with foil activation detectors with a phase composition of the layered compound corresponding to curve 3, by the moving triplet. Starting from the relative distributions of the thermal neutron flux density and assuming that the boundary of the perturbation of the neutron flux coincides with the upper cutoff of the compound formed by the pyrolytic graphite and cesium, it may be assumed that curve 2 (see Fig. 2) corresponds to the phase composition of the layered compound $C_{36}Cs + C_{24}Cs$, while curve 3 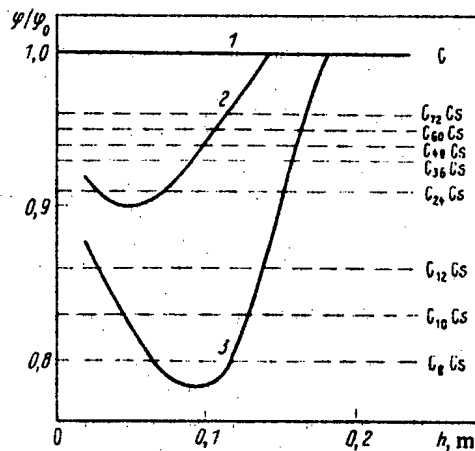corresponds to $C_{12}Cs + C_8Cs$. Figure 3 shows the decrease in the flux density of thermal neutrons calculated as the ratio of the perturbed and starting fluxes. The measured degree of attenuation of the flux density of thermal neutrons with different phase compositions of the layered graphite compound agrees well with the computed data [1].

Thus, the computed characteristics of the degree of attenuation of the flux density of thermal neutrons have been experimentally checked for different phases of the layered compound formed by pyrolytic graphite with cesium, and the possibility of precision regulation of the flux density of thermal neutrons by the absorption method has been demonstrated.

LITERATURE CITED

1. I. G. Gverdtsiteli et al., At. Energ., 48, No. 3, 187 (1980).
2. I. G. Gverdtsiteli et al., ibid., 53, No. 1, 36 (1982).
3. I. G. Gverdtsiteli et al., ibid., 54, No. 3, 211 (1983).
4. F. Salzano and S. Aronson, Nucl. Sci. Eng., 28, No. 1, 51 (1967).

HYDRODYNAMIC CHARACTERISTICS OF A DISPERSELY ANNULAR
GAS—LIQUID FLOW IN ANNULAR CHANNELS

G. V. Alekseev, N. A. Gromov,   UDC 532.542
Yu. I. Dzarasov, and S. Yu. Orlov

The results of an experimental investigation of the effect of the geometric dimensions of a channel, the physical properties of the liquid and the gas, and the flow parameters on the brightness distribution between the core of the flow and the films on the tube and rod as well as on the hydraulic drag are given in this paper. The experiments were conducted on a test stand which consisted of closed liquid and open air loops. The liquid and gas passed through filters, measuring diaphragms, and a system of reference and regulating valves into mixers mounted at the entrance to the experimental sections, which are vertical annular channels 25 × 13.5 and 52 × 30 mm in diameter and 4–5 m in length. The spacing of the rods is accomplished with the help of studs distributed uniformly around the periphery in threes on the same level with a spacing of 400–500 mm. Volume separators were mounted at the exit from the channel.

The flow rate of water in the films on the tube m_2 and the rod m_4 were determined in the region of the steady-state flow regime of the mixture. To this end a procedure was adopted for the selection of samples from the boundary layer of the flow through a porous insert. Tubes and rods perforated around the entire perimeter with holes were used as samplers in the tests along with porous inserts made out of a nickel alloy. The construction of samplers is
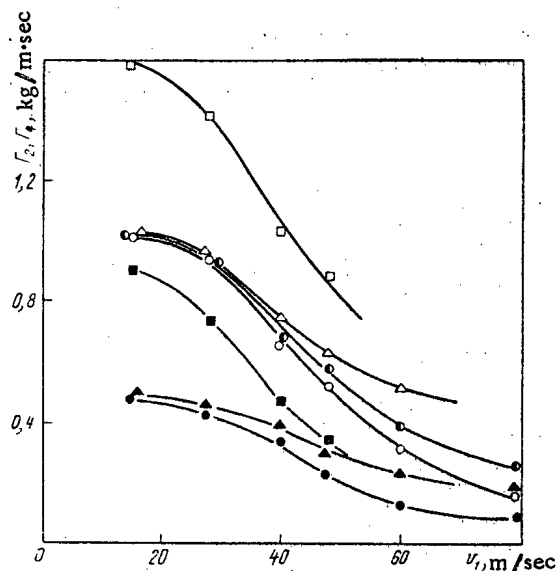
Fig. 1. Dependence of the specific flow rate of liquid
in a film on the reduced air velocity at p = 0.18 MPa,
G_l = 380 kg/(m²·sec) in an annular channel 52 × 30 mm
in diameter: □ Γ_2 and ■ Γ_4 for μ_l = 1 × 10⁻³ Pa·sec;
25 × 13.5 mm in diameter: ○ Γ_2 and ● Γ_4 for μ_l = 1 ×
10⁻³ Pa·sec; ◑ Γ_2 for μ_l = 3 × 10⁻³ Pa·sec; △) Γ_2 and
▲) Γ_4 for μ_l = 8 × 10⁻³ Pa·sec.

described in [1], and the identity of the measurement procedure and the results of determin-
ation of the flow rate of liquid in a film is shown experimentally with the help of porous
and perforated inserts.

After selection of the samples the pressure differentials were measured by a differen-
tial manometer on a section located in the region of steady-state flow. The pulse lines
were equipped with settling tanks for the removal of air from them. The experiments were
performed in the following ranges of the regime parameters: reduced velocity of the gas
v_1 = 15-85 m/sec; specific mass flow rate of liquid G_l = 50-2000 kg/(m²·sec); working
pressure in the channel p = 0.18-0.3 MPa· Water and water-glycerine solutions with a 35%
and 55% glycerine content by volume were used as the working liquids. The viscosity of
the liquid varied in the range μ_l = (1-8) × 10⁻³ Pa·sec.

This paper is a continuation of [2], in which a dependence on v_1 of the flow rate of
water in a film on a tube and on a rod in an annular channel 25 × 13.5 mm in diameter at a
working pressure of p = 0.3 MPa was shown for different values of G_l. It was noted that the
nature of the dependence is in agreement with the test data obtained on tubes.

The test data are presented in Fig. 1 in the form of a dependence of the specific flow
rate of liquid in the film on a tube Γ_2 and a rod Γ_4 (Γ is the flow rate in the film on a unit
length of the wetted perimeter) on the reduced air velocity in the channel for fixed values
of the specific mass flow rate of the liquid. It follows from Fig. 1 that Γ_2 is appreciably
larger than Γ_4, which is probably associated with the different curvature of the tube and rod
surfaces. An increase in the equivalent channel diameter d_e leads to an increase in Γ_2 and
Γ_4 for the identical values of G_l, v_1 and μ_l; this difference decreases noticeably as v_1 in-
creases. On the other hand, the effect of the viscosity of the liquid on Γ_2 and Γ_4 increases
as v_1 increases and leads to a significant increase in the specific flow rate of liquid in
the films in the region of large velocities. One can note that no effect of the viscosity
of the liquid on Γ_2/Γ_4 has been detected. Evidently a change in the viscosity of the liquid
leads to a proportional change in these parameters.

It has been established during the measurement of the pressure differentials in the work-
ing sections that as the flow rate of gas and liquid and also the viscosity of the liquid in-
crease the pressure losses along the channel length increase. The pressure losses to fric-
tion were determined from the total pressure differences measured in tests after subtraction
of the leveling pressure head. The density of the mixture was calculated in terms of the
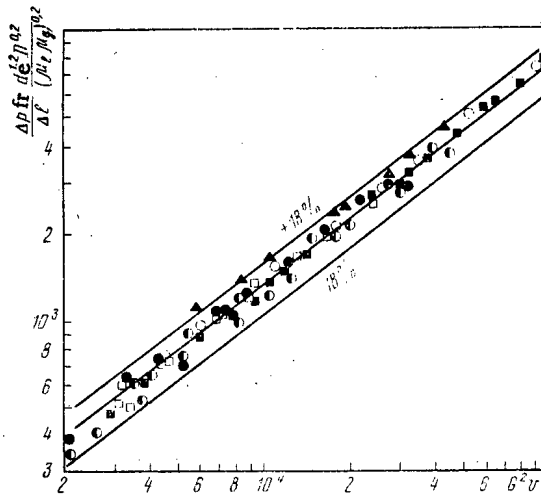volume flow gas content β:

Fig. 2. Pressure losses to friction in the flow of a
gas—liquid mixture in an annular channel 25 × 13.5 mm
in diameter: ○ p = 0.3 MPa, air + water; ■ 0.18 MPa,
air + water; ◐ 0.18 MPa, air + solution (65% water +
35% glycerine); ● 0.18 MPa, air + solution (45% water +
55% glycerine); 52 × 30 mm in diameter: ◻ 0.18 MPa,
air + water; 25 × 10 mm in diameter [3]: ▲ 2.2 MPa,
argon + water.

$$\rho = \rho_g \beta + \rho_l (1 - \beta),\qquad(1)$$

where ρ_g and ρ_l are the densities of the gas and liquid, respectively.

The following dependence (dimensions in the SI system):

$$\frac{\Delta p_{fr}}{\Delta z} = \frac{9.65 \cdot 10^{-2}}{d_e^{1,2}} (G^2 v)^{0.75}\qquad(2)$$

was proposed in [3] on the basis of extensive test material obtained during investigation
of the flow of argon—water mixtures in vertical annular channels 25 × 10 and 25 × 15 mm in
diameter in the 0.1-2.15 MPa pressure range in the working sections and for a specific mass
flow rate of the mixture of 300-2000 kg/(m²·sec).

The specific volume of the mixture v in formula (2) is defined in terms of the mass
flow gas content x:

$$v = v_l (1 - x) + v_g x,\qquad(3)$$

where v_l and v_g are the specific volumes of the liquid and gas, respectively.

Satisfactory agreement of the test data obtained in this paper with formula (2) has
been established in the analysis of the data only for the case of the flow of air—water mix-
tures in an annular channel 25 × 13.5 mm in diameter. At the same time an increase in the
equivalent diameter of the channel and the viscosity of the liquid leads, other conditions
being equal, to a decrease and an increase, respectively, in the losses to friction in com-
parison with the values calculated from formula (2). Thus one can assume that the peculiar-
ities of the channel geometry as well as the physical properties of the liquid are not taken
into account to a full extent in this formula. The viscosity of the water was practically
constant in the tests [3]. The effect of the geometrical dimensions of the annular channel
cross section is reflected in the dependence (2) by the equivalent diameter d_e. However,
variation of the curvature of the walls of an annular channel is not taken into account by
this parameter. The hydraulic drag in the flow of a two-phase dispersely annular flow is
determined by the structure of the film surface, which in turn depends on the curvature of
the channel wall. As was noted above, $\Gamma_2 > \Gamma_4$, and therefore the pressure losses to fric-
tion should be determined mainly by the structure of the film surface flowing on the tube.

The dependence (2) was refined (dimensions in the SI system) in the analysis of the test data of this paper with account taken of the variation of the viscosity of the liquid and the geometrical dimensions of the annular channels:

$$\frac{\Delta p_{fr}}{\Delta z} = \frac{1.3}{d_e^{1.2} D^{0.2}} (G^2 v)^{0.75} (\mu_l/\mu_g)^{0.2}, \tag{4}$$

where D is the diameter of a tube of the annular channel.

The experimental data of this paper and the data of [3] obtained in an annular channel 25 × 10 mm in diameter with a working pressure of 2.2 MPa in the channel are presented as an example in Fig. 2 in generalized coordinates. The dependence (4) generalizes the test points with an error of ±18%.

The authors are grateful to V. F. Semenenko for participation in the experiments.

LITERATURE CITED

1. N. A. Gromov, in: Problems of the Gas Thermodynamics of Power Plants [in Russian], No. 4, Kharkov Aviation Inst. (1981), p. 100.
2. G. V. Alekseev et al., in: Problems of the Gas Thermodynamics of Power Plants [in Russian], No. 4, Kharkov Aviation Inst. (1981), p. 14.
3. N. Adorni and I. Casagrande, "Further investigations in adiabatic dispersed two-phase flow: Pressure drop and film thickness measurements with different channel geometries. Analysis of the influence of geometrical and physical parameters," CISE, Report R-53 (1963).

RADIOACTIVE CONTAMINATION SPREAD BY

TRANSPORTATION MOVING ALONG ROADS

V. E. Vostrukhov and A. F. Lyzlov   UDC 613.169.16

Considerable practical significance attaches to radionuclide transport over the surface of the soil. For example, a study has been made [1] of the possible spread of radioactive substances from locally contaminated areas due to the movement of people and transportation. A general solution represents some difficulty, on account of the nonlinearity in the initial transport equation. It is therefore important to choose a reasonable model allowing the equations to be solved analytically or numerically. The criterion for the reasonableness is of course experiment.

The following assumptions are made:

1. The change in contamination level on the road is due to the contact with the wheels of vehicles moving in one direction and is defined by the constants λ, λ_1, and λ_2. Here λ is the adhesion-transport coefficient [2], while λ_1 and λ_2 define the residual contamination on the road and wheel correspondingly. There is no wear on the wheel rubber or any other transport mechanism for the radionuclides and the road material. All the wheels have the same diameter d.

2. The surface contamination source contains radionuclides whose half-lives are larger than the transport times for the distance considered, and it has zero thickness, while the transverse dimensions are determined by the sizes of the carriageway on which the vehicles move. The contamination level in the source is known.

With these assumptions, we get the following system of difference equations for the change in contamination level of the road $R(m, n)$ and a wheel $W(m, n)$ where m is the number of wheels and $n = x/\pi d$, where x is the distance to the contamination source:
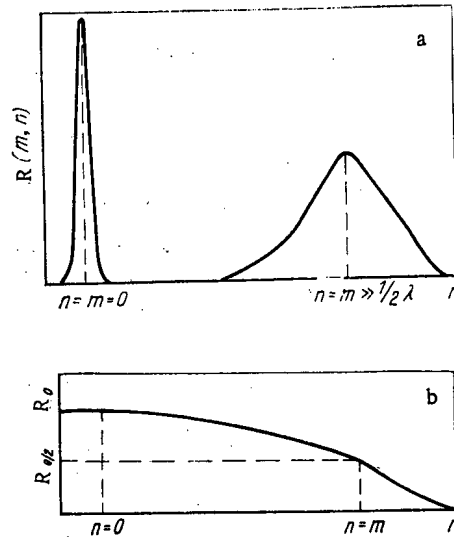

Fig. 1. Change in road contamination level
R(m, n) in accordance with the distance n
from the source and the number m of wheels
passing: a) radionuclides transported from
a local source; b) for $W(m, 0) = R_0 =$ const,
$2\lambda \sqrt{mn} \gg 1$.

$$W(m+1, n+1) = W(m+1, n) - \lambda [\lambda_2 W(m+1, n) - \lambda_1 R(m, n)]; \tag{1}$$

$$R(m+1, n) = R(m, n) - \lambda [\lambda_1 R(m, n) - \lambda_2 W(m+1, n)]. \tag{2}$$

Here R(0, n) is the road contamination level before the vehicles pass. The solution is of
the main interest for n >> 1, m >> 1, and when these conditions are obeyed, m is a continuous
parameter, while (1) and (2) reduce to a first-order differential-equation system:

$$\begin{cases} \partial W(m+1, n)/\partial n = \lambda [\lambda_1 R(m, n) - \lambda_2 W(m+1, n)]; \\ \partial R(m, n)/\partial m = \lambda [\lambda_2 W(m+1, n) - \lambda_1 R(m, n)]; \end{cases} \tag{3}$$

$$n \gg 1, \quad m \gg 1. \tag{4}$$

We consider the radionuclide transport from a local contamination source $A\delta(m)\,\delta(n)$, where A
is the total activity in the source and $\delta(m)$ and $\delta(n)$ are Dirac δ functions [3]. Then sys-
tem (3) and (4) becomes

$$\begin{cases} \partial W(m+1, n)/\partial n = \lambda [\lambda_1 R(m, n) - \lambda_2 W(m+1, n)]; \\ \partial R(m, n)/\partial m = \lambda [\lambda_2 W(m+1, n) - \lambda_1 R(m, n)] + \\ \quad + A\delta(m)\,\delta(n). \end{cases} \tag{5}$$
$$\tag{6}$$

We eliminate W(m + 1, n) from (5) and (6) to get

$$(1/\lambda^2 \lambda_1 \lambda_2)\, \partial^2 R(m, n)/\partial m\, \partial n + (1/\lambda \lambda_2)\, \partial R(m, n)/\partial n +$$
$$+ (1/\lambda \lambda_1)\, \partial R(m, n)/\partial m = A\delta(m)\,\delta(n)/\lambda \lambda_1 -$$
$$- [A\delta(m)/\lambda^2 \lambda_1 \lambda_2]\, \partial \delta(n)/\partial n. \tag{7}$$

We make the change of variables R(m, n) = R' (m', n') × exp (−m'−n') where m' = $\lambda\lambda_1$m, n' =
$\lambda\lambda_2$n, to reduce (7) to an equation of hyperbolic type in canonical form, whose solution takes
the form [3]

$$R(m, n) = A\delta(n)\,\theta(m)\exp[-\lambda(\lambda_2 n + \lambda_1 m)] +$$
$$+ A\lambda\lambda_2 \theta(n)\,\theta(m)\, I_1(2\lambda \sqrt{\lambda_1 \lambda_2 mn})\, \sqrt{\lambda_1 m/\lambda_2 n} \times$$
$$\times \exp[-\lambda(\lambda_2 n + \lambda_1 m)], \tag{8}$$

124

where $\theta(m)$ and $\theta(n)$ are Heaviside functions [3], while I_1 is a modified Bessel function of the first order and first kind [4]. The integral activity on the road after the passage of m wheels should be A. In fact, $\int_0^\infty R(m, n)dn = A$ [4], where $R(m, n)$ is derived from (8).

In practice, the situation can occur [5] where the contamination level of the wheels on leaving the contaminated surface is constant: $W(m, 0) = R_0 = $ const; then (3) and (4) can be written as

$$\begin{cases} \partial W(m+1, n)/\partial n = \\ = \lambda [\lambda_1 R(m, n) - \lambda_2 W(m+1, n)] + R_0 \delta(n); \\ \partial R(m, n)/\partial m = \lambda [\lambda_2 W(m+1, n) - \lambda_1 R(m, n)]. \end{cases}$$

(9)

(10)

We solve (9) and (10) in the same way as for (5) and (6) [3] to get

$$R(m, n) = \theta(n) R_0 (\lambda_2/\lambda_1) \exp[-\lambda(\lambda_1 m + \lambda_2 n)] \times$$

$$\times \sum_{k=1}^\infty (\lambda_1 m/\lambda_2 n)^{k/2} I_k (2\lambda \sqrt{\lambda_1 \lambda_2 mn}),$$

(11)

where I_k is a modified Bessel function of the first kind and of order k [4].

To analyze the results, we consider only the case of purely adhesion interaction, when $\lambda_1 = \lambda_2 = 1$; then according to (8) the change in road contamination level for $2\lambda \sqrt{mn} \gg 1$ (large values of the argument in the modified Bessel functions of the first kind) is described by

$$R(m, n) = A\lambda \sqrt{m/n} \exp[-\lambda(\sqrt{n} - \sqrt{m})^2]/2 \sqrt{\pi\lambda} \sqrt[4]{mn}.$$

(12)

The maximum in $R(m, n)$ occurs at $m = n$:

$$R(m, n) = (A/2) \sqrt{\lambda/\pi n}.$$

(13)

The first term on the right in (8) defines the changing contamination level at the source. Therefore, the radionuclide transport for $2\lambda \sqrt{mn} \gg 1$ resembles the motion along OX for a wave packet decreasing in amplitude as $\sim 1/\sqrt{n}$. The contamination level in the source follows the law $\sim \exp(-\lambda m)$ (Fig. 1a). Expression (11) for $2\lambda \sqrt{mn} \gg 1$ is a strictly decreasing function of n (Fig. 1b).

These results provide an estimate of the transport of radioactive substances to comparatively large distances if the transport occurs within the framework of this model.

LITERATURE CITED

1. V. I. Grishmanovskii and A. F. Lyzlov, in: Dosimetric and Radiometric Monitoring in Operating with Radioactive Substances and Ionizing-Radiation Sources [in Russian], Vol. 1, Atomizdat, Moscow (1980), p. 204.
2. A. D. Zimon, Decontamination [in Russian], Atomizdat, Moscow (1975).
3. V. S. Vladimirov, Equations of Mathematical Physics, Marcel Dekker (1971).
4. Handbook on Special Functions [in Russian], Nauka, Moscow (1979).
5. V. I. Bad'in et al., in: Dosimetry and Radiometry of Ionizing Radiations and Radiation Safety [in Russian], TsNIIatominform, Moscow (1980), p. 17.

DETERMINATION OF THE INDUSTRIAL CONTAMINATION OF SOIL WITH ^{137}Cs ON THE

GLOBAL BACKGROUND BY MEANS OF THE ANALYSIS OF THE DEPTH DISTRIBUTION OF ACTIVITY

A. N. Silant'ev, I. G. Shkuratova,   UDC 631.42
and G. N. Neushkina

In [1], a method was considered for the determination of low-level industrially con-
taminated soil with ^{137}Cs on the global background, based on a comparison of the parameters
of the spatial distribution of the global and total contamination. The industrial contam-
ination can be determined also by comparing the observed vertical distribution of the con-
tamination in the soil with the global distribution. The global fallout of radioactive nu-
clides on the surface of the earth has taken place since 1954 up to the present time, and
the maximum of this fallout was reached in 1962-1965. Industrial contamination of the
surface of the earth started from the instant of startup of factories or nuclear power
stations, but a high degree of contamination can be observed only in exceptional cases.
Usually, the fact of the discharge of radionuclides is known, and it is necessary to de-
termine the degree of contamination of the soil due to this discharge, from the results of
measurements in the territory not later than the lapse of a few months after discharge. In
this case, the contamination is found to be concentrated in the surface layer of the soil
and, as the corresponding measurements show, is located in the upper 5-mm layer of soil.
The investigations conducted of the vertical distribution of ^{137}Cs allow a method to be
developed for the determination of the industrial contamination of soil by ^{137}Cs on the
global contamination background [2].

In order to distinguish the industrial contamination on the global background, it is
necessary to know the vertical distribution of the latter, which can be defined by the val-
ues of the migration parameters of the global ^{137}Cs in the soil. In order to distinguish
the global contamination from the total, it is necessary to establish the dependence of the
migration parameters of the global ^{137}Cs on the properties of the soil and their variation
with depth. For this purpose, the ^{137}Cs content was measured layer by layer in different
soils. From the position of the maximum of the global ^{137}Cs concentration in the soil, the
rate of directional migration of this radionuclide in the soil was determined, and from the
solution of the diffusion equation [3], the variation of the coefficient of diffusion with
depth. Figure 1 shows the characteristic profile of the depth distribution of the global
concentration of ^{137}Cs in the soil and the values of the quasidiffusion coefficient. The
investigations showed that in the majority of cases for virgin and aged soils, a constant
value of the quasidiffusion coefficients is characteristic in the upper layer of soil down
to a certain depth, after which its increase is observed. Therefore, as quantitative char-
acteristics of the migration of global ^{137}Cs in soil, the rate of directional migration,
the quasidiffusion coefficient in the upper layer of soil, and the depth from which its
increase commences can be used.

As a result of generalization of the measurements, the values obtained are grouped in
accordance with certain characteristics of the soil and are presented in Table 1. The
investigations were conducted in the central region of the European part of the Soviet
Union, where turf-podzolic and gray forest soils persist predominantly. It can be seen
from the data presented that the least constant value of the quasidiffusion coefficient
is observed only in the case of contamination of soil below wood, the litter of which in-
hibits the penetration of radionuclides into the depth of the soil. There is always a cer-
tain surface layer of soil within the limits of which the migration parameters are con-
stant. This allows the industrial contamination of soil by ^{137}Cs on the global background
to be determined. In fact, by determining the migration parameters with respect to the ^{137}Cs
distribution in the soil deeper than 5 mm, the values of the migration parameters can be
estimated which are characteristic for the upper 5 mm layer of soil and, knowing them, the
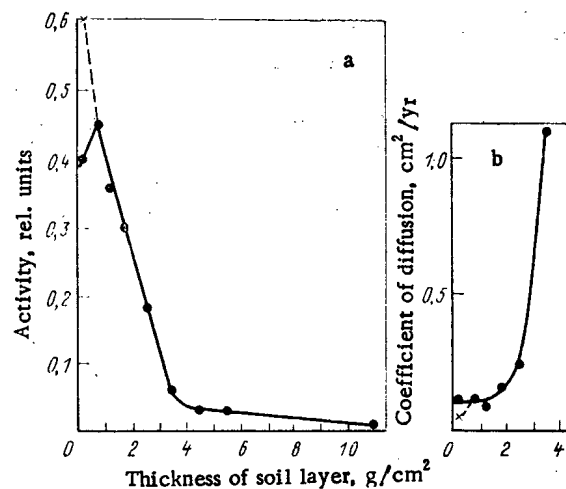amount of global ^{137}Cs located in this layer can be estimated.

Fig. 1. Vertical distribution of the global ^{137}Cs concentration in soil (a) and the values of the quasi-diffusion coefficient (b) corresponding to this distribution; •) values corresponding to global ^{137}Cs; ×) total value of ^{137}Cs with a 10% industrial contamination of the global level; ——) form of distribution for global ^{137}Cs; ---) form of distribution for the total contamination in the surface layer of soil.

TABLE 1. Migration Parameters of Global ^{137}Cs in Virgin and Aged Soils

Orography of section examined	Composition of soil	State of turf layer	Rate of directional migration cm/yr	Quasidiffusion co-efficient, cm²/yr	Depth at which quasidiffusion coefficient is constant, cm
On upland	Sandy loam	Sod	0,1	0,15	3
		No sods	0,1	0,15	2
	Loam	Same	0,1	0,4	6
Below mixed wood	Sandy loam	Same	0,05	0,1	1
	Loam	Same	0,1	0,5	1
Below coniferous wood	Sandy loam	Sod	0,1	0,1	2.
		No sods	0,05	0,1	2
In river water meadow	Same	Sod	0,2	0,5	8
	Loam	Same	0,2	0,3	5
On the slope	Sandy loam	Same	0,3	0,4	8
	Loam	Same	0,1	0,2	3

Numerous investigations were carried out of the vertical distribution of global ^{137}Cs in the surface layer of soil, which showed that the accuracy used for the thickness of the soil layer where the content of global ^{137}Cs is determined [4] is insufficient for distinguishing the low level of industrial contamination on the global background. In order to increase this accuracy, it was necessary to change from measurement of the linear dimensions of the layer thickness to determination of the mass of unit surface area of the soil layer being investigated. As we are interested in the vertical distribution of ^{137}Cs in soil, and not its absolute value, there is no necessity to dry the samples being investigated (it is sufficient that the whole monolith of the upper layer of soil investigated should have identical moisture content). Knowing the specific activity of the soil and taking account of the change of density with depth, we obtain the vertical distribution of ^{137}Cs with sufficient accuracy for determining the low level of contamination of the soil surface.

As an example, we shall consider the vertical distribution of global ^{137}Cs in soil shown in Fig. 1. If, to the existing distribution in the upper soil layer, is added ^{137}Cs to an amount consisting of 10% of the presence of global ^{137}Cs in the soil, then the distri-

127

bution shown in Fig. 1a by the dashed line is obtained. As this type of distribution can be observed also for global ^{137}Cs, then it is difficult to judge from it the presence of additional contamination on the surface of the soil. However, the distribution of the quasi-diffusion coefficient obtained, denoted in Fig. 1b also by the dashed line, allows one to see how the value of the quasidiffusion coefficient is varying for the surface layer of the soil. By estimating this value from the form of the curve characteristic for global ^{137}Cs, the additional quantity of ^{137}Cs deposited on the soil surface can be determined. According to estimates carried out, this method allows the industrial contamination of soil to be determined, amounting to a total of 10% of the global contamination.

Thus, the low level of industrial contamination of soil by ^{137}Cs can be determined on the global background, based on knowledge of the relationship of the vertical distribution of global ^{137}Cs in the soil and comparison of the observed vertical distribution with that characteristic for global distribution.

LITERATURE CITED

1. A. N. Silant'ev and I. G. Shkuratova, At. Energ., 52, No. 4, 248 (1982).
2. A. N. Silant'ev and I. G. Shkuratova, Inventor's Certificate No. 755007, Byull Izobret., No. 4, 349 (1983).
3. A. N. Silant'ev and I. G. Shkuratova, in: Proceedings of the Institute of Experimental Meteorology [in Russian], Gidrometizdat, Moscow, No. 11(97) (1983), p. 72.
4. A. N. Silant'ev and I. G. Shkuratova, in: Proceedings of the Institute of Experimental Meteorology [in Russian], Gidrometizdat, Moscow, No. 6(107) (1983), p. 58.

BEHAVIOR OF WATER-COOLED—WATER MODERATED FUEL ELEMENTS IN A HYPOTHETICAL ACCIDENT WITH THE EJECTION OF CONTROL RODS

A. I. Mysenkov and V. N. Proselkov

UDC 621.039.56:621.039.58

The growth of nuclear power leads to a further increase of the power density of water-cooled—water moderated (VVÉR) cores, and this imposes more rigid requirements on nuclear power plant (NPP) safety and, in particular, demands increased reliability of fuel elements (FE). In analyzing NPP safety, various classes of accidents and the behavior of the FE are considered.

In the present article we consider the thermal behavior of a VVÉR-1000 FE during a hypothetical accident with the ejection of the operative bank of control and safety rods (CSR) at nominal power. In such an accident the fuel element cladding (FEC) may rupture as a result of the liberation of an appreciable amount of energy in the fuel in a very short time (a fraction of a second). Therefore, an estimate of the temperatures of the fuel and FEC, and the changes in thermal and neutron power under abnormal conditions is of definite interest.

Fundamental Characteristics of NPP, Core, FEA and VVÉR-1000 FE. The basic fuel characteristics were determined for an optimum fuel cycle, taking account of restrictions imposed by the requirements of transportability of the reactor vessel, the maximum operating temperature of the zirconium alloy of the FEC (350°C), the coolant velocity, etc. [1]. We list below the basic characteristics of the VVÉR-1000, its FE, and fuel element assemblies (FEA) [2]:

Nominal thermal power, MW	3000
Nominal coolant pressure at reactor outlet, MPa	15.7
Average coolant temperature in reactor (at outlet/inlet), °C	322/290
Flow rate of coolant through reactor, m³/h	80,000
Power density of core, kW/liter	111
Maximum temperature of FEC on coolant side, °C	350
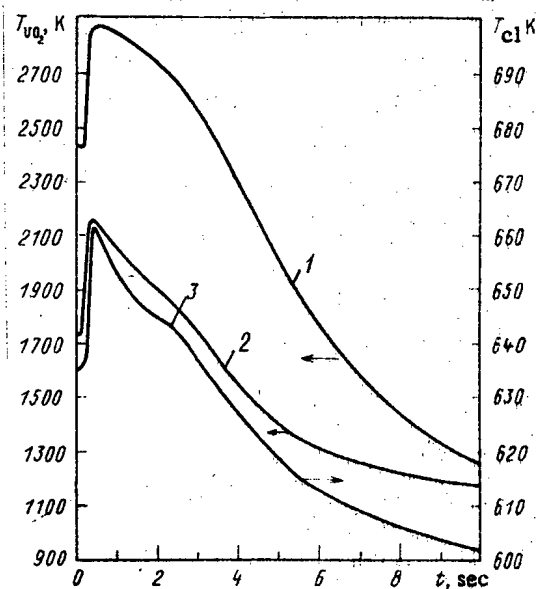
Fig. 1. Time dependence of 1) maximum fuel temperature at center of FE, 2) average temperature in most stressed cross section of FE in accident with ejection of bank of CSR, 3) maximum temperature of FEC.
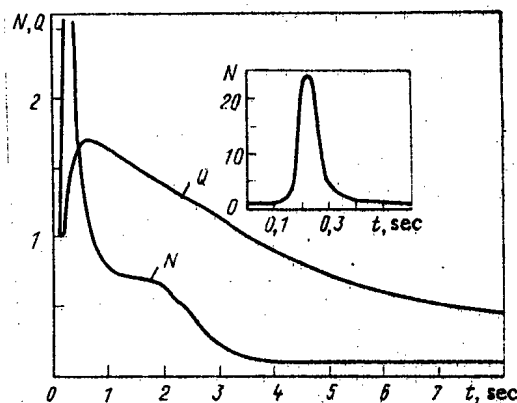
Fig. 2. Relative time dependence of neutron (N) and thermal (Q) reactor power during an accident with the ejection of a bank of CSR.

Linear power density of FE, W/cm:
```
  average. . . . . . . . . . . . . . . . . . . . . . 166-177
  maximum. . . . . . . . . . . . . . . . . . . . . .   490
Outside diameter of FE, mm . . . . . . . . . . . . .   9.1
Thickness of FEC, mm . . . . . . . . . . . . . . . . 0.63-0.68
Diametral clearance between fuel and
  cladding, mm . . . . . . . . . . . . . . . . . . . 0.19-0.32
Diameter of axial opening, mm. . . . . . . . . . . . 1.4-1.6
Helium pressure under FEC in cold
  state, MPa . . . . . . . . . . . . . . . . . . . . 1.96-2.45
```
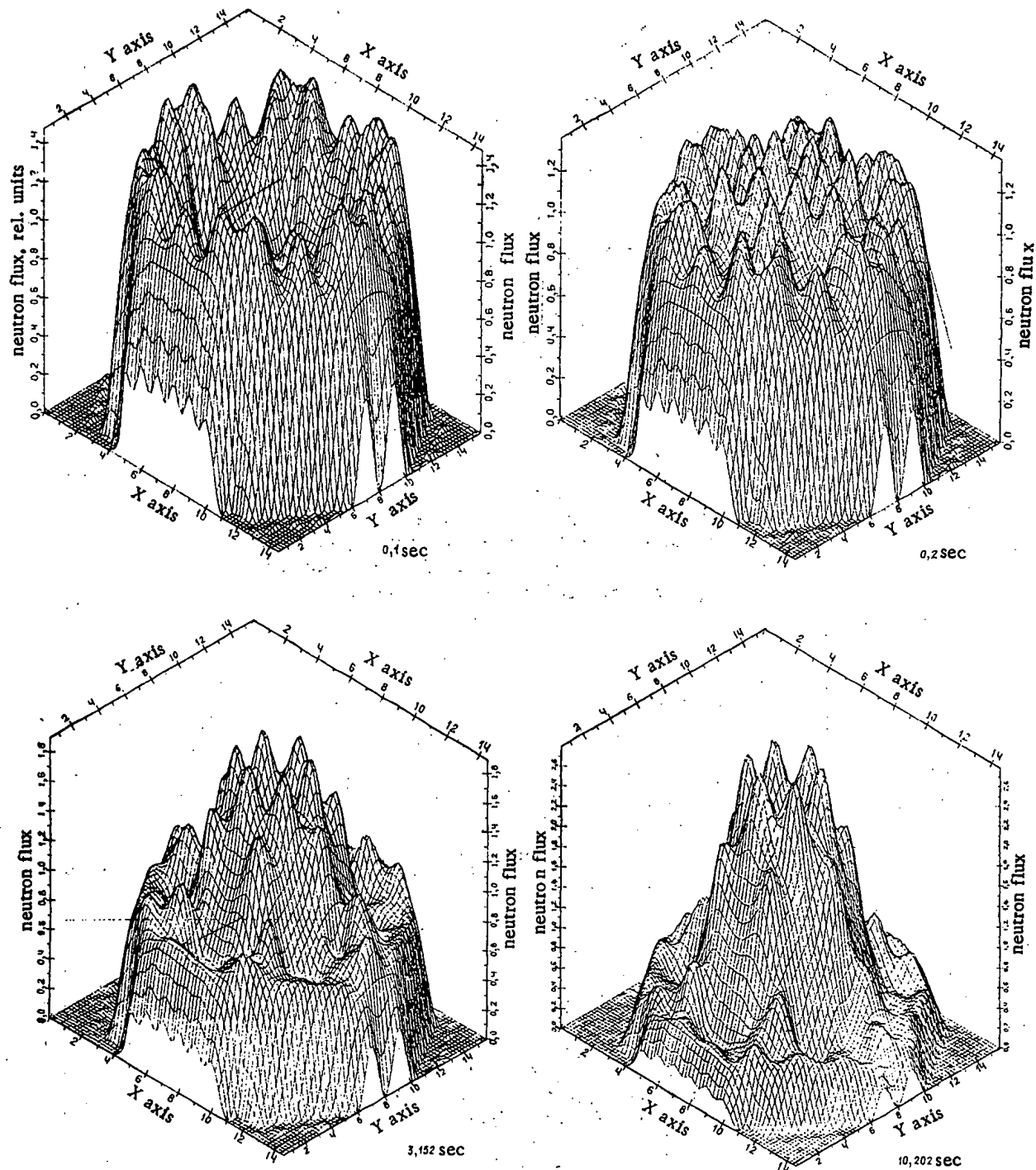
Fig. 3. Shape of neutron flux (averaged over a FEA) at various times during
an accident with the ejection of a bank of CSR.

Thermal Behavior of a VVER-1000 FE in an Accident with the Ejection of an Operative
Bank of CSR. In the accident under consideration, the ejection of control rods in the
core introduces positive reactivity, which produces an increase in the neutron flux and a re-
distribution of power release over the core volume.

The reactor was assumed to be operating at 102% of nominal power shortly after the first
fuel loading, i.e., under the worst condition from the point of view of thermal resistance
of the diametral clearance between fuel and cladding.

130

To be conservative, it was assumed that the bank of CSR for suppressing xenon oscillations is in the core, and the bank of CSR closest to the rods being ejected is stuck in the extreme upper position during scram. During scram the CSR are inserted into the core from their extreme positions in 3.6 sec. The delay time from the instant of initiation of the emergency signal to the instant of deenergizing of the CSR was taken equal to 0.5 sec. The ejection of the operative bank of CSR occurs 0.101 sec from the start of the process being modeled.

Figures 1-3 show the time dependence of 1) the maximum fuel temperature at the center of a FE, the fuel temperature averaged over a cross section of a FE, and the temperature of the outer surface of the FEC; 2) the neutron and thermal reactor power; 3) the shape of the neutron distribution. These parameters were calculated with the MOST-10 program [3] designed for treating the unsteady operation of NPP, using a model of three-dimensional space—time kinetics.

The calculation shows that with the ejection of the operative bank of CSR there is a brief (∿0.02 sec) reactor excursion on prompt neutrons. The neutron power increases about 23 times in 0.25 sec; in 0.4 sec almost all the positive reactivity introduced is suppressed by the Doppler effect; in ∿0.5 sec the fuel temperature reaches a maximum of 2613°C. In this same time the temperatures of the outer and inner surfaces of the FEC reach their maximum values of 388 and 466°C, respectively. The thermal reactor power reaches a maximum, increased by ∿70%. In the calculations the conductivity of the diametrical clearance between fuel and cladding was conservatively taken equal to 0.28 W/cm^2·°C, which is smaller than the actual values. During the accident the heat flux exceeds its critical value for a short time ((∿1.5 sec).

The following conclusions can be drawn from an analysis of the assumed consequences of an accident with the ejection of the operative bank of CSR from the core:

in the hypothetical accident considered, the maximum fuel temperature does not reach the melting point of UO_2;

the maximum (averaged over the cross section of a FE) enthalpy of the fuel does not exceed 583 kJ/kg (140 cal/g);

the maximum temperature of the FEC (388°C) does not exceed the temperature (600°C) at which the zirconium alloy (Zr + 1% Nb) abruptly loses mechanical strength [1], and is appreciably lower than the temperature (1200°C) [4] at which the steam—zirconium reaction is intense.

LITERATURE CITED

1. V. A. Sidorenko, Problems of the Safe Operation of VVÉR Reactors [in Russian], Atomizdat, Moscow (1977).
2. Yu. V. Vikhorev et al., At. Energ., 54, 163 (1983).
3. A. I. Mysenkov, in: Papers of CMEA Seminar "Thermal Physics — 82" [in Russian], Vol. 2, Karlovy Vary (1982), p. 30.
4. "General conditions of safety control of nuclear power plants during design, construction, and operation (OPB-82)," At. Energ., 54, 151 (1983).

How To Comply With The New Copyright Law

Participation in the Copyright Clearance Center (CCC) assures you of legal photocopying at the moment of need.

Libraries everywhere have found the easy way to fill photocopy requests legally and instantly, without the need to seek permissions, from more than 3000 key publications in business, science, humanities, and social science. You can:

Fill requests for multiple copies, interlibrary loan (beyond the CONTU guidelines), and reserve desk without fear of copyright infringement.

Supply copies from CCC-registered publications simply and easily.

The Copyright Clearance Center is your one-stop place for on-the-spot clearance to photocopy for internal use.

Its flexible reporting system accepts photocopying reports and returns an itemized invoice. You send only one convenient payment. CCC distributes it to the many publishers whose works you need.

And, you need not keep any records, the CCC computer will do it for you. Register now with the CCC and you will never again have to decline a photocopy request or wonder about compliance with the law for any publication participating in the CCC.

To register or for more information, just contact:
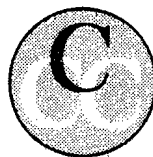
Copyright Clearance Center
21 Congress Street
Salem, Massachusetts 01970
(617) 744-3350

a not-for-profit corporation

NAME	TITLE
ORGANIZATION	
ADDRESS	
CITY	STATE ZIP
COUNTRY	TELEPHONE

CHANGING YOUR ADDRESS?

In order to receive your journal without interruption, please complete this change of address notice and forward to the Publisher, 60 days in advance, if possible.

(Please Print)

Old Address:

_____
name

_____

_____
address

_____
city

_____
state (or country)   zip code

New Address

_____
name

_____

_____
address

_____
city

_____
state (or country)   zip code

_____
date new address effective

_____
name of journal

THE LANGUAGE OF SCIENCE

Plenum
PUBLISHING CORPORATION | **233 Spring Street, New York, New York 10013**

MEASUREMENT TECHNIQUES
Izmeritel'naya Tekhnika
Vol. 27, 1984 (12 issues) $520

MECHANICS OF COMPOSITE MATERIALS
Mekhanika Kompozitnykh Materialov
Vol. 20, 1984 (6 issues) $430

METAL SCIENCE AND HEAT TREATMENT
Metallovedenie i Termicheskaya Obrabotka Metallov
Vol. 26, 1984 (12 issues) $540

METALLURGIST
Metallurg
Vol. 28, 1984 (12 issues) $555

PROBLEMS OF INFORMATION TRANSMISSION
Problemy Peredachi Informatsii
Vol. 20, 1984 (4 issues) $420

PROGRAMMING AND COMPUTER SOFTWARE
Programmirovanie
Vol. 10, 1984 (6 issues) $175

PROTECTION OF METALS
Zashchita Metallov
Vol. 20, 1984 (6 issues) $480

RADIOPHYSICS AND QUANTUM ELECTRONICS
Izvestiya Vysshikh Uchebnykh Zavedenii, Radiofizika
Vol. 27, 1984 (12 issues) $520

REFRACTORIES
Ogneupory
Vol. 25, 1984 (12 issues) $480

SIBERIAN MATHEMATICAL JOURNAL
Sibirskii Matematicheskii Zhurnal
Vol. 25, 1984 (6 issues) $625

SOIL MECHANICS AND FOUNDATION ENGINEERING
Osnovaniya, Fundamenty i Mekhanika Gruntov
Vol. 21, 1984 (6 issues) $500

SOLAR SYSTEM RESEARCH
Astronomicheskii Vestnik
Vol. 18, 1984 (6 issues) $365

SOVIET APPLIED MECHANICS
Prikladnaya Mekhanika
Vol. 20, 1984 (12 issues) $520

SOVIET ATOMIC ENERGY
Atomnaya Énergiya
Vols. 56-57, 1984 (12 issues)..................... $560

SOVIET JOURNAL OF GLASS PHYSICS AND CHEMISTRY
Fizika i Khimiya Stekla
Vol. 10, 1984 (6 issues) $235

SOVIET JOURNAL OF NONDESTRUCTIVE TESTING
Defektoskopiya
Vol. 20, 1984 (12 issues) $615

SOVIET MATERIALS SCIENCE
Fiziko-khimicheskaya Mekhanika Materialov
Vol. 20, 1984 (6 issues) $445

SOVIET MICROELECTRONICS
Mikroélektronika
Vol. 13, 1984 (6 issues) $255

SOVIET MINING SCIENCE
Fiziko-tekhnicheskie Problemy Razrabotki Poleznykh Iskopaemykh
Vol. 20, 1984 (6 issues) $540

SOVIET PHYSICS JOURNAL
Izvestiya Vysshikh Uchebnykh Zavedenii, Fizika
Vol. 27, 1984 (12 issues) $520

SOVIET POWDER METALLURGY AND METAL CERAMICS
Poroshkovaya Metallurgiya
Vol. 23, 1984 (12 issues) $555

STRENGTH OF MATERIALS
Problemy Prochnosti
Vol. 16, 1984 (12 issues) $625

THEORETICAL AND MATHEMATICAL PHYSICS
Teoreticheskaya i Matematicheskaya Fizika
Vol. 58-61, 1984 (12 issues)...................... $500

UKRAINIAN MATHEMATICAL JOURNAL
Ukrainskii Matematicheskii Zhurnal
Vol. 36, 1984 (6 issues) $500

Send for Your Free Examination Copy

RUSSIAN JOURNALS IN THE PHYSICAL AND MATHEMATICAL SCIENCES

AVAILABLE IN ENGLISH TRANSLATION

ALGEBRA AND LOGIC
Algebra i Logika
Vol. 23, 1984 (6 issues) $360

ASTROPHYSICS
Astrofizika
Vol. 20, 1984 (4 issues) $420

AUTOMATION AND REMOTE CONTROL
Avtomatika i Telemekhanika
Vol. 45, 1984 (24 issues) $625

COMBUSTION, EXPLOSION, AND SHOCK WAVES
Fizika Goreniya i Vzryva
Vol. 20, 1984 (6 issues) $445

COSMIC RESEARCH
Kosmicheskie Issledovaniya
Vol. 22, 1984 (6 issues)........................... $545

CYBERNETICS
Kibernetika
Vol. 20, 1984 (6 issues).......................... $445

DIFFERENTIAL EQUATIONS
Differentsial'nye Uravneniya
Vol. 20, 1984 (12 issues) $505

DOKLADY BIOPHYSICS
Doklady Akademii Nauk SSSR
Vols. 274-279, 1984 (2 issues) $145

FLUID DYNAMICS
Izvestiya Akademii Nauk SSSR,
Mekhanika Zhidkosti i Gaza
Vol. 19, 1984 (6 issues)......................... $500

FUNCTIONAL ANALYSIS AND ITS APPLICATIONS
Funktsional'nyi Analiz i Ego Prilozheniya
Vol. 18, 1984 (4 issues) $410

GLASS AND CERAMICS
Steklo i Keramika
Vol. 41, 1984 (6 issues) $590

HIGH TEMPERATURE
Teplofizika Vysokikh Temperatur
Vol. 22, 1984 (6 issues) $520

HYDROTECHNICAL CONSTRUCTION
Gidrotekhnicheskoe Stroitel'stvo
Vol. 18, 1984 (12 issues) $385

INDUSTRIAL LABORATORY
Zavodskaya Laboratoriya
Vol. 50, 1984 (12 issues) $520

INSTRUMENTS AND EXPERIMENTAL TECHNIQUES
Pribory i Tekhnika Éksperimenta
Vol. 27, 1984 (12 issues) $590

JOURNAL OF APPLIED MECHANICS AND TECHNICAL PHYSICS
Zhurnal Prikladnoi Mekhaniki i Tekhnicheskoi Fiziki
Vol. 25, 1984 (6 issues) $540

JOURNAL OF APPLIED SPECTROSCOPY
Zhurnal Prikladnoi Spektroskopii
Vols. 40-41, 1984 (12 issues) $540

JOURNAL OF ENGINEERING PHYSICS
Inzhenerno-fizicheskii Zhurnal
Vols. 46-47, 1984 (12 issues) $540

JOURNAL OF SOVIET LASER RESEARCH
A translation of articles based on the best Soviet research in the field of lasers
Vol. 5, 1984 (6 issues) $180

JOURNAL OF SOVIET MATHEMATICS
A translation of Itogi Nauki i Tekhniki and Zapiski Nauchnykh Seminarov Leningradskogo Otdeleniya Matematicheskogo Instituta im. V. A. Steklova AN SSSR
Vols. 24-27, 1984 (24 issues)...................... $1035

LITHOLOGY AND MINERAL RESOURCES
Litologiya i Poleznye Iskopaemye
Vol. 19, 1984 (6 issues) $540

LITHUANIAN MATHEMATICAL JOURNAL
Litovskii Matematicheskii Sbornik
Vol. 24, 1984 (4 issues) $255

MAGNETOHYDRODYNAMICS
Magnitnaya Gidrodinamika
Vol. 20, 1984 (4 issues) $415

MATHEMATICAL NOTES
Matematicheskie Zametki
Vols. 35-36, 1984 (12 issues)..................... $520